



THE UNIVERSITY OF
SYDNEY

COPYRIGHT AND USE OF THIS THESIS

This thesis must be used in accordance with the provisions of the Copyright Act 1968.

Reproduction of material protected by copyright may be an infringement of copyright and copyright owners may be entitled to take legal action against persons who infringe their copyright.

Section 51 (2) of the Copyright Act permits an authorized officer of a university library or archives to provide a copy (by communication or otherwise) of an unpublished thesis kept in the library or archives, to a person who satisfies the authorized officer that he or she requires the reproduction for the purposes of research or study.

The Copyright Act grants the creator of a work a number of moral rights, specifically the right of attribution, the right against false attribution and the right of integrity.

You may infringe the author's moral rights if you:

- fail to acknowledge the author of this thesis if you quote sections from the work
- attribute this thesis to another author
- subject this thesis to derogatory treatment which may prejudice the author's reputation

For further information contact the University's Director of Copyright Services

sydney.edu.au/copyright

FUNCTIONAL SURFACE MICROPATTERNS BY DEWETTING OF THIN POLYMER FILMS

Manuel Ghezzi

School of Chemistry
University of Sydney

2015

A thesis submitted in fulfilment of the requirements
for the degree of Doctor of Philosophy

To Itziar

Declaration

This Thesis is presented at the School of Chemistry, University of Sydney, as part of the requirements for the degree of Doctor of Philosophy in Science. All of the experimental work reported within this Thesis has been carried out by the author in the School of Chemistry, University of Sydney during August 2011 and January 2015. No part of this Thesis has been submitted for any other degree to this or any other institution. When collaboration has been necessary, the collaborators have been named and the extent of the collaboration made clear. Results from other authors are referenced in the usual manner throughout the text.

Manuel Ghezzi

Date

Abstract

Patterned polymer surfaces are of great importance with respect to an increasing number of technological and bio-medical applications, due to their great versatility in terms of chemical composition, properties and processing techniques. Surface micropatterning by spontaneous dewetting of thin polymer films represents a versatile and robust process to fabricate surfaces with controlled topography and chemistry at the micro-scale. In this Thesis, we used polymer dewetting in combination with complementary approaches to engineer both surface chemistry and the ordering of the dewetting patterns.

The dewetting of poly(D,L-glycolide-*co*-lactide) (PLGA) thin films on polystyrene (PS) was combined with the grafting of protein-repellent poly(ethylene glycol) (PEG), in order to form topographical and chemical surface micropatterns consisting in protein-adhesive PS domains surrounded by protein-repellent PEG-grafted PLGA films. The produced micropatterned surfaces were used for site-specific protein adsorption, and represent a promising platform for biological applications, such as proteomics, single-cell studies and tissue engineering.

Spatially ordered surface micropatterns were obtained by combining polymer dewetting with microcontact printing and colloidal lithography, respectively. The dewetting of thin PS films was guided within specific regions of the substrate by prestamping of the silicon substrate with self-assembled monolayers of an alkylsilane by microcontact printing. Ordered micropatterns consisting in arrays of holes with tunable size were obtained by exploiting the spontaneous dewetting of poly(4-vinyl pyridine) (P4VP) thin films on PS from the holes produced by colloidal imprinting with two-dimensional colloidal crystals assembled on the polymer bilayer.

Acknowledgments

I am immensely grateful to my supervisors, A/Prof Chiara Neto and Dr Stuart Thickett. The work presented in this Thesis would not be possible without their constant support and guidance during the last three years. Chiara has been an exceptional mentor, showing endless patience and support, especially in those days when nothing seemed to work. She guided me through a deep process of personal growth. Besides the obvious growth in terms of scientific knowledge, this growth as a persona represents the real added value you get at the end of a PhD. I also want to thank her for the trust she showed at all the times and in particular during her sabbatical in the UK. Special thanks go to Stuart, who was the first friendly face upon landing at the Airport of Sydney. Stuart was my laboratory mentor during my first six months, and showed me what means being a good scientist. Even after he moved to UNSW, he kept showing me exceptional support.

I want to acknowledge Dr Laurence Meagher for constantly giving me precious advices and directions that played a crucial role in solving the problems I have been facing during my research projects. I am also very thankful to Laurence for allowing me to spend two weeks in his laboratory at CSIRO.

My PhD journey would have not been such a great life experience without all the friends and colleagues of the Key Centre for Polymers and Colloids (KCPC) and the Neto Group, which represents a unique work environment, made of great people and great scientists. I want to thank all the current and past members of this *big family* I have been lucky enough to part of for the great time spent inside (and outside) the lab.

I am grateful to the Australian Government for providing me with financial support with an International Postgraduate Award, and to CSIRO for the top-up scholarship. I also want to thank the University of Sydney for the funds they provided through the Postgraduate Research Support Scheme which contributed to the costs of the conferences at which I presented the work in this Thesis.

Acknowledgements

Special thanks go to my parents, Sara and Antonio. Thanks for accepting my decision to move to (literally) the other side of the world and for showing me endless support during the last three years. Thanks for never making me feel alone, especially in my early days in Australia. This great personal and career achievement, represented by the completion of a PhD, is in great part the result of what you have done for me ever since and I will never be thankful enough to show my endless gratitude to you.

Last but not least, I want to thank you Itziar, my amazing girlfriend and life partner. The list of the reasons why I am so thankful to you could fill up another Thesis. Here, I simply want to thank you for taking the best out me and for being by my side every single day ever since during our amazing yet curvy journey in Australia.

Publications resulting from this work

1. Ghezzi, M.; Wang, P. Y.; Kingshott, P.; Neto, C. Guiding the Dewetting of Thin Polymer Films by Colloidal Imprinting. *Advanced Materials Interfaces* **2015**, DOI: 10.1002/admi.201500068.
2. Ghezzi, M.; Thickett, S. C.; Telford, A. M.; Easton, C. D.; Meagher, L.; Neto, C. Protein Micropatterns by PEG Grafting on Dewetted PLGA Films. *Langmuir* **2014**, *30*, 11714-11722.
3. Ghezzi, M.; Thickett, S. C.; Neto, C. Early and Intermediate Stages of Guided Dewetting in Polystyrene Thin Films. *Langmuir* **2012**, *28*, 10147-10151.

Presentations resulting from this work

1. Ghezzi, M.; Neto, C. Functional Surface Micro-Patterns by Dewetting of Thin Polymer Films (oral), *28th European Colloid and Interface Society Conference (ECIS)*, Limassol (Cyprus), September 2014.
2. Ghezzi, M.; Neto, C. Functional Surface Micro-Patterns by Dewetting of Thin Polymer Films (poster), *Australian Nanotechnology Network (ANN) Early Career Research (ECR) Meeting*, Sydney NSW (Australia), September 2014.
3. Ghezzi, M.; Thickett, S. C.; Telford, A. M.; Easton, C. D.; Meagher, L.; Neto, C. PEG Grafting on Dewetted PLGA Films: Biocompatible and Degradation-Resistant Surfaces for Protein Micro-Patterning (oral), *29th Australian Colloid and Surface Science Student Conference (ACSSSC)*, Ballarat VIC (Australia), February 2014.

4. Ghezzi, M.; Barbey, R.; Perrier, S.; Neto, C. Dewetting of Hyperbranched Polystyrene Thin Films (poster), *29th Australian Colloid and Surface Science Student Conference (ACSSSC)*, Ballarat VIC (Australia), February 2014.
5. Ghezzi, M.; Thickett, S. C.; Neto, C. Guided Dewetting in Polystyrene Thin Films (poster), *Australian Colloid and Interface Symposium (ACIS 2013)*, Noosa QLD (Australia), March 2013.
6. Ghezzi, M.; Thickett, S. C.; Neto, C. Guided Dewetting in Polymer Thin Films on Chemically Heterogeneous Substrates (poster), *28th Australian Colloid and Surface Science Student Conference (ACSSSC)*, Riverwood Downs NSW (Australia), February 2012. Poster prize winner.

Table of Contents

DECLARATION.....	I
ABSTRACT	II
ACKNOWLEDGMENTS	III
PUBLICATIONS RESULTING FROM THIS WORK.....	V
PRESENTATIONS RESULTING FROM THIS WORK	V
TABLE OF CONTENTS.....	VII
1. INTRODUCTION.....	1
1.1. Preamble	1
1.2. Patterning of Polymer Surfaces	3
1.2.1. Photolithography	3
1.2.2. Printing techniques	4
1.2.3. Direct writing techniques	5
1.2.4. Lithographically controlled wetting	7
1.3. Patterning of Polymer Surfaces by Dewetting	8
1.3.1. Thermodynamics of dewetting	9
1.3.2. Evolution of dewetting	11
1.3.3. Surface micropatterning by dewetting	14
1.3.4. Spatially controlled dewetting patterns	15
1.4. Thesis Outline.....	17
References	18
2. MATERIALS AND METHODS	26
2.1. Preparation of Thin Polymer Films	26
2.2. Ellipsometry	27
2.3. Atomic Force Microscopy (AFM).....	30
2.4. Contact Angle Goniometry.....	33
2.5. Thermogravimetric Analysis and Differential Scanning Calorimetry	34
2.6. X-Ray Photoelectron Spectroscopy (XPS).....	35

2.7. Quartz Crystal Microbalance with Dissipation Monitoring (QCM-D)	36
References	39
3. PROTEIN MICROPATTERNING ON DEWETTED PLGA FILMS.....	41
3.1. Introduction	41
3.2. Materials and Methods	44
3.2.1. Sample preparation.....	44
3.2.2. Aminolysis and hydrolysis of PLGA/PS bilayers.....	44
3.2.3. PEG grafting on PLGA-NH ₂ and PLGA-OH films on PS	45
3.2.4. Protein adsorption	46
3.3. Results	47
3.3.1. Dewetting of PLGA films	47
3.3.2. PLGA aminolysis and hydrolysis	49
3.3.3. PEG grafting	53
3.3.4. Protein adsorption and preferential protein immobilization.....	57
3.3.5. Degradation of PLGA films and PEG-g-PLGA films	61
3.4. Discussion.....	62
3.4.1. Layer inversion	63
3.4.2. Surface functionalization of PLGA.....	64
3.4.3. Grafting of PEG to PLGA	64
3.4.4. Protein adsorption on grafted PEG layers	65
3.4.5. Degradation resistance	66
3.5. Summary.....	66
References	67
4. GUIDED DEWETTING BY MICROCONTACT PRINTING.....	71
4.1. Introduction	71
4.2. Materials and Methods	74
4.2.1. Sample preparation.....	74
4.2.2. Surface characterization	75
4.3. Results and Discussion	76
4.3.1. Spatially-ordered dewetting patterns.....	76
4.3.2. Dynamics of hole growth	80
4.4. Summary.....	82
References	83
5. GUIDED DEWETTING BY COLLOIDAL IMPRINTING	86
5.1. Introduction	86

Table of Contents

5.2.	Materials and Methods	87
5.2.1.	Preparation of polymer bilayers and surface characterization.....	87
5.2.2.	Preparation of colloidal crystals.....	89
5.2.3.	Colloidal imprinting	90
5.2.4.	Dewetting of imprinted P4VP/PS bilayers	90
5.3.	Results	91
5.3.1.	Binary colloidal crystals	91
5.3.2.	Single-particle colloidal crystals	94
5.4.	Discussion.....	102
5.4.1.	Colloidal imprinting	103
5.4.2.	Guided dewetting	103
5.4.3.	Wettability of the polymer films	104
5.4.4.	Layer inversion	104
5.5.	Summary.....	105
	References	106
6.	CONCLUSIONS AND OUTLOOK.....	109

Chapter 1.

Introduction

1.1. Preamble

Patterning of surfaces is of great importance in many areas of science and technology. The last two decades have seen the introduction of several lithographic techniques that have enabled the fabrication of surface micropatterns with resolution in the sub-micrometre range. Traditional lithographic techniques used for microfabrication are capable of producing well-controlled topographical or chemical micropatterns. However, there are a growing number of applications requiring the simultaneous control over surface properties at the nano and microscale, which require the development of novel, cost-effective microfabrication techniques capable of combining topographical and chemical micropatterning.

Patterned polymer films are of growing importance with respect to an increasing number of applications, due to their great versatility in terms of chemical composition, properties and processing techniques. Polymer coatings offer a number of advantages when compared to bulk polymeric devices, such as the ability to tailor the properties of a surface without the need to change the bulk properties of the material. Polymer coatings find applications in a broad range of fields, including micro-electronics,^{1, 2} optics^{3,4} and biomedicine.⁵

Micropatterned polymer surfaces comprising both chemical and topographical features are becoming increasingly popular in biomedical research for the study of cell physiology and are progressively replacing the traditional flat substrates for cell culture. Cells within organs or tissues are embedded into highly structured microenvironments,

which impose specific boundary conditions that influence architecture, mechanics and function of the cell.^{6, 7} The size and structure of the microenvironment limits cell volume and spreading, affecting the spatial distribution of cell adhesion.⁸ The biochemical composition and the mechanical properties (e.g. stiffness) of the microenvironment determine the factors responsible for cell adhesion, and thereby affect intracellular signalling and cell assembly.⁹ In addition to playing a role in the configuration of intra-cellular organisation, the cell microenvironment also influences gene expression and cell differentiation.¹⁰ Topographical and chemical micropatterning of surfaces allow the reconstruction of tissue-like conditions for in vitro cell cultures and the investigation of the sensitivity and response of a cell to specific micro-environmental environments.

The ability to fabricate micropatterned devices with controlled chemistry and topography represents a key factor to future development of microfluidics technologies. Since the advent of microfluidics approximately two decades ago, there has been a progressive increase in the interest and development of devices for fluid flow at the microscale.¹¹ The first applications of microfluidic technologies have been in analysis, for which they offer a number of useful features, such as small volume of samples, high resolution and sensitivity, low cost, and short time for analysis.¹² At the present, microfluidics find applications in a broad range of fields, including drug discovery, diagnostic chips,¹³ organic synthesis¹⁴ and microreactors.¹⁵ A crucial role in the success of microfluidic technology is played by the development of surface modification and patterning techniques, which enable the fabrication of devices with topographical or chemical features in the sub-micrometre scale.¹⁶ The high hydrodynamic drag of liquids at the solid interface can reduce significantly the rate of liquids flowing in micron-sized channels, requiring the use of high operating pressure. Chemical micro-patterning of microfluidic devices by selective coating of the channels can effectively increase interfacial slip of the liquid and reduce the hydrodynamic drag.¹⁷

1.2. Patterning of Polymer Surfaces

1.2.1. Photolithography

Photolithography is one of the main methods currently used for patterning polymers.^{18, 19} In photolithographic methods, patterns are generated by selectively exposing monomer- or polymer-coated surfaces (polymer monolayers or polymer brushes) to photoirradiation and by subsequently removing selected areas of the film via dissolution in solvent (Figure 1.1). Site-selective irradiation is typically achieved by illuminating the film through a mask and is used to trigger photopolymerization, photocrosslinking, functionalization or decomposition reactions. Photolithographically patterned polymer surfaces have found applications in the production of light emitting diodes (LEDs),²⁰ photonic crystals,⁴ optical components,²¹ and microarrays of proteins and cells.²² Revzin *et al.*²³ used photolithography to fabricate planar arrays of cells, in which individual cells are confined in poly(ethylene glycol) (PEG) hydrogel wells (Figure 1.1b). Albrecht *et al.*²⁴ reported the precise positioning of cells in patterned poly(ethylene glycol) diacrylate (PEGDA) hydrogel produced by photocrosslinking (Figure 1.1c) and achieved multiplexing of different types of cells by multistep irradiation of the hydrogel (Figure 1.1d).

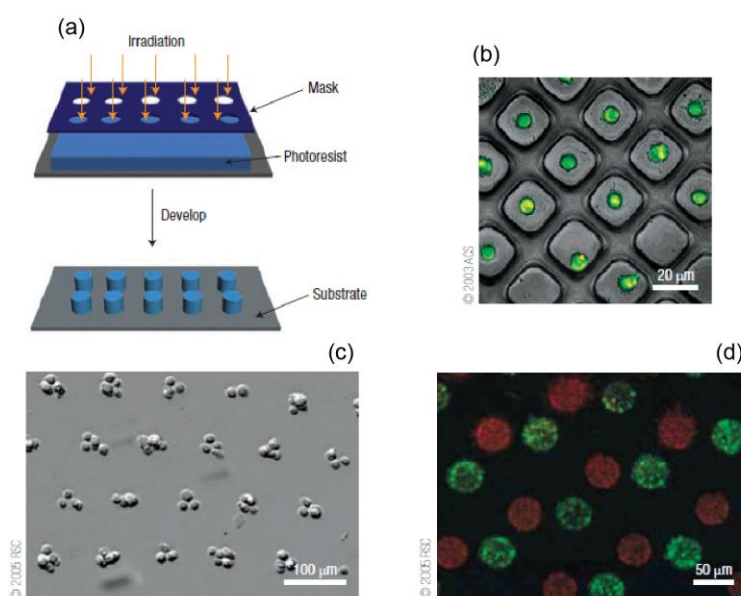


Figure 1.1. Patterning of polymers by photolithography. (a) Schematic of the photolithography technique.²⁵ (b, d) Confocal and (c) optical micrograph of cells confined within polymer microwells generated by photolithography.^{23, 24}

Overall, the major challenges in photolithography are to enhance the resolution of the patterning while keeping costs low, as well as to pattern functional materials without compromising their properties. For example, photolithography is not suitable for the direct patterning of bioactive species with high sensitivity to UV irradiation, photoinitiators or solvents used for the development of the patterns. In addition, the technique is not suitable for the patterning of curved surfaces and patterning with high resolution is usually achieved at high costs and over long times.

1.2.2. Printing techniques

Modern printing methods for polymer patterning include nanoimprint lithography, dip-pen lithography and microcontact printing. In nanoimprint lithography (NIL) the patterning of polymers is realized by pressing a mould against a softened thermoplastic polymer or a liquid polymer precursor and trapping the pattern in the solid state by either cooling the moulded material (thermal NIL) or by UV-photocuring (UV-NIL) the polymer precursor (Figure 1.2a).^{26, 27} A wide range of commercial thermoplastic polymers, including polystyrene (PS), polycarbonate, poly(methyl methacrylate) (PMMA) and poly(vinyl alcohol) (PVA) are being used for thermal NIL to produce photoresists for pattern-transfer in photolithographic applications. More sophisticated polymer systems include conductive polymers,²⁸ polymers labelled with fluorescent chromophores²⁹ and block copolymers.³⁰ In contrast with thermal nanoimprinting, UV-NIL employs photosensitive polymer precursors and photosetting typically occurs by free-radical or cationic polymerization. One of the main drawbacks of UV-NIL is sensitivity to oxygen, which can lead to defects in high resolution patterns.³¹ Future applications for NIL rely mainly on the development of new photochemically sensitive materials that are not susceptible to oxygen inhibition and can be easily removed from the mould.

Microcontact printing (μ CP) is an efficient technique for the patterning of large-area surfaces with spatial resolution down to the sub-micrometre range.³² In microcontact printing, an elastomeric stamp is used to transfer material, usually referred to as 'ink', to the substrate to produce a surface pattern mirroring the relief features of the stamp (Figure 1.2b).^{33, 34} The technique has been extensively used for direct and indirect patterning of surfaces with polymer monolayers and thin films. In direct

deposition, the ‘ink’ consists of a solution of the polymer to be transferred on the surface. In indirect deposition, the selective deposition of the polymer is followed by surface-initiated polymerization, site-specific electropolymerization or back-filling.^{35, 36} Microcontact printing is suitable for large-scale production (e.g. reel-to-reel or sheet-to-sheet schemes) and does not require expensive instrumentation, which led to significant popularity of the technique in the field of organic electronics and for site-specific immobilization of proteins and cells.^{37, 38} In spite of its popularity, the main limitations of the technique are represented by the difficulty in the production of multilayer and multicomponent patterns, along with the difficulty in achieving patterns with sub-100-nm resolution.

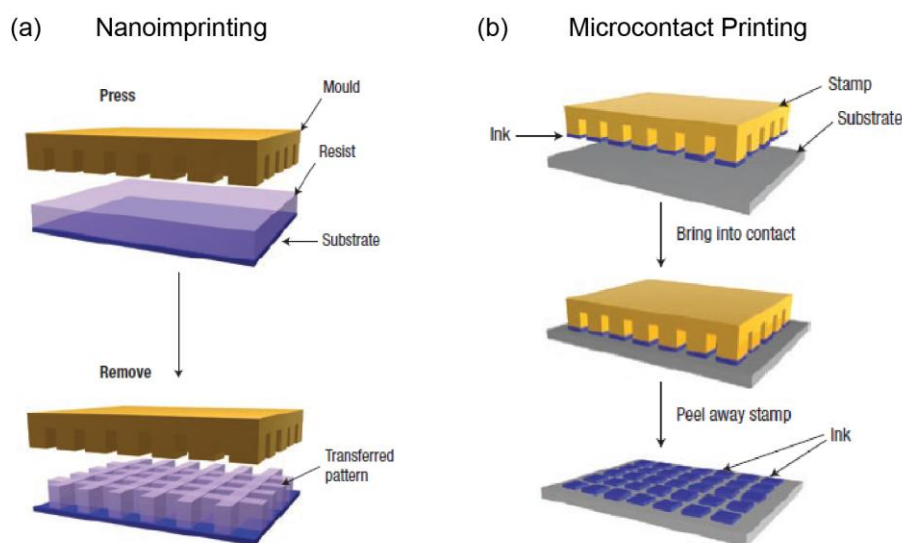


Figure 1.2. Patterning of polymers by printing techniques. Schematic representation of (a) nanoimprint lithography (NIL) and (b) microcontact printing (μ CP).²⁵

1.2.3. Direct writing techniques

Patterning by direct writing is realized by delivering molecules from a nozzle or from a probe tip to specific regions of the substrate. The most commonly used direct writing techniques are dip-pen nanolithography and inkjet printing. Dip-pen nanolithography (DPN) is a scanning probe microscopy-based technique, in which the tip of an atomic force microscope (AFM) selectively deposit the patterning material on the underlying substrate (Figure 1.3a).³⁹ When the AFM tip coated with the patterning material is

scanned above the surface a liquid meniscus forms between the tip and the substrate, with consequent transfer of the patterning material from the tip to the substrate. Patterning of polymer nanostructures by DPN is achieved in two ways: by depositing on the surface of reactive precursors and subsequently performing site-specific polymerization reactions,⁴⁰ or by directly delivering to the substrate polymer solutions or melts.⁴¹⁻⁴³ DPN in combination with electrochemical polymerization was successfully employed to create high-resolution patterns of conductive polymers, such as polythiophene and poly(vinylcarbazole).⁴⁴ Patterning by DPN has also been used for the fabrication of micro and nano-arrays of proteins and DNA, showing promising applications in fundamental studies of biological recognition and diagnostics.^{45, 46}

In inkjet printing, droplets originating from the break-up of a jet of polymer solution are deposited on a surface, and form a polymer pattern when the solvent evaporates (Figure 1.3b).⁴⁷ Polymer patterning can also be achieved by depositing onto a polymer substrate droplets of a solvent that etches the polymer.⁴⁸ Patterning of polymers by inkjet printing has been used in the fabrications of optics,⁴⁸ sensors,⁴⁹ and arrays of proteins and cells.⁵⁰ However, to date the main application of inkjet printing is in the field of plastic electronics, for example in the production of polymer transistors circuits and organic LEDs.⁴⁸

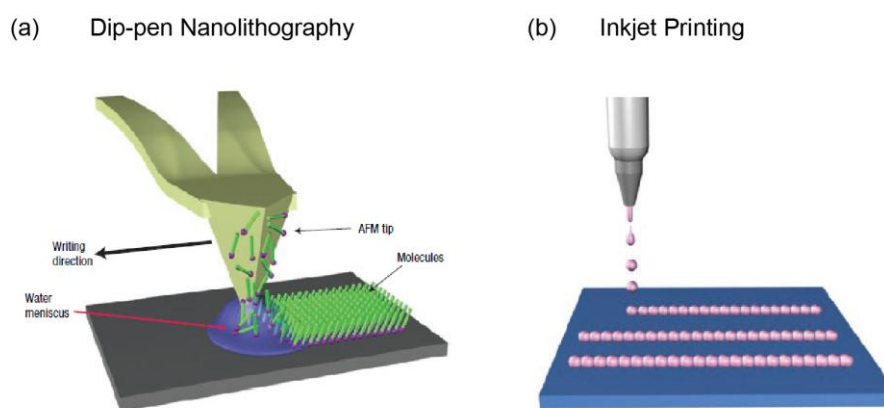


Figure 1.3. Patterning of polymers by direct writing techniques. Schematic representation of (a) dip-pen nanolithography and (b) inkjet printing.²⁵

1.2.4. Lithographically controlled wetting

Lithographically controlled wetting (LCW) is a wet-patterning process that exploits the self-organization of soluble materials, permitting spatial control provided by the features of a stamp (Figure 1.4).⁵¹ When a stamp is placed in contact with a liquid thin film on a solid substrate, the capillary forces pin the solution to the stamp protrusions, giving rise to an array of menisci (Figure 1.4b, e). As the solvent evaporates, the solution forms a subfemtoliter fluid cell under each stamp protrusion and, when the solution reaches supersaturation, the solute precipitates onto the substrate within the menisci, giving rise to a deposit replicating the protrusion of the stamp (Figure 1.4b, c and Figure 1.4e, f). Thermodynamic and kinetic parameters such as the nature of the solvent, the capillary flow and evaporation rate, the solute intermolecular interactions and the interactions with the substrate determine the morphology and structure of the printed features.⁵²

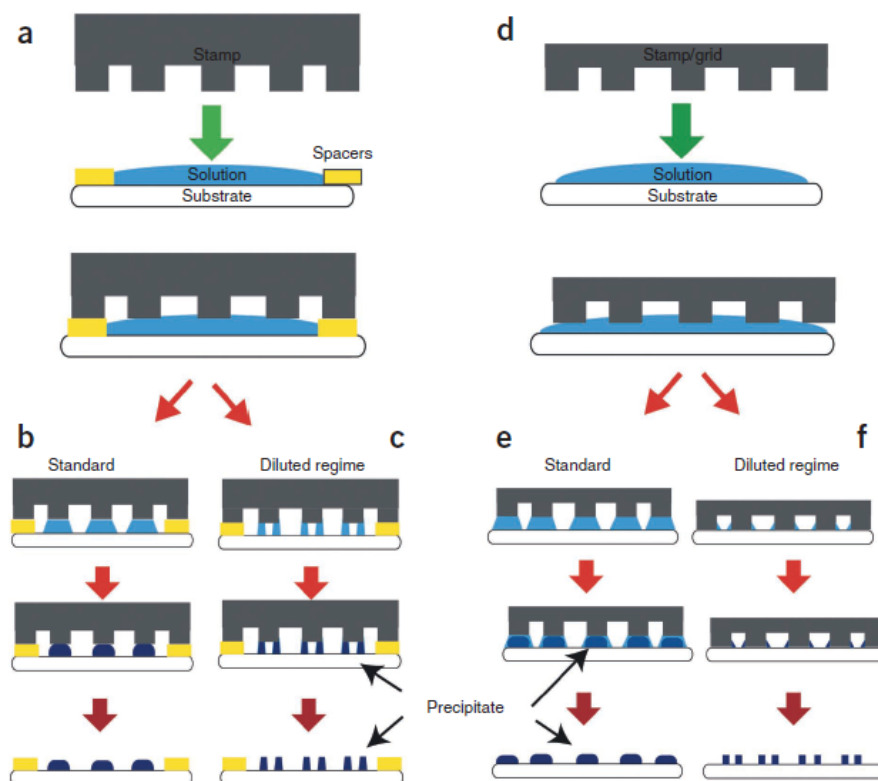


Figure 1.4. Schematic representation of lithographically controlled wetting. (a–c) Scheme of printing using (a) prefabricated spacers (b) in the standard and (c) diluted regime. (d–f) Scheme of printing using (d) a floating stamp in the (e) standard or (f) diluted regime.⁵¹

In the standard configuration, a prefabricated spacer can be used to keep the desired stamp-substrate distance (Figure 1.4a–c). Alternatively, LCW can be carried out using a floating stamp, in which case the system is self-regulating, as the solute itself determines the stamp-surface distance when it precipitates under the stamp protrusion (Figure 1.4d–f). By using a very diluted solution, supersaturation is not achieved within the fluid columns and, as the solvent evaporates, the residual solution remains pinned to the edges, forming an inverted meniscus under the protrusion (Figure 1.4c, f). The consequent mass transport to the edge via capillary flow yields a replica of the protrusion edges, rather than the protrusion itself.⁵³ This regime is suitable to downscale the size of printed features relative to the original size of the stamp features, as it is possible to print double features whose size depends on the curvature radius of the edges rather than on the size of the flat part of the protrusion.

Major limitations of LCW are the solubility of materials that can be used in LCW, as it works only with soluble compounds, and the difficulty of applying LCW to curved surfaces.

In this Thesis, a novel patterning approach based on the self-assembly of polymer thin films by spontaneous dewetting was developed to produce surface coatings with controlled chemistry and topography. The thermodynamics of dewetting and the application of dewetting to surface micropatterning are presented in the next Section.

1.3. Patterning of Polymer Surfaces by Dewetting

Dewetting is the spontaneous withdrawal of a thin liquid film on a non-wettable substrate.^{54, 55} Dewetting is encountered in everyday life, for example in the rupture of a water layer into droplets on a hydrophobic surface such as a dirty windowpane or a Teflon-coated pan. Thin liquid films consisting of polymer melts (i.e. polymer films above the glass transition temperature, T_g) are the ideal candidate for dewetting experiments, since polymer films can be easily spin coated as uniform thin films onto solid substrates, are non-volatile, and allow a fine control over the timescale of dewetting – which depends on the viscosity of the liquid film – by tuning annealing temperature and molecular weight of the polymer.^{56, 57}

Dewetting of thin liquid films arises from the instability of the liquid film on the solid surface and depends on the interplay between unfavourable surface interactions and attractive intermolecular forces.^{58, 59} The physical principles governing the dewetting of thin liquid films on solid surfaces are briefly presented in the next section.

1.3.1. Thermodynamics of dewetting

The behaviour of a liquid film on a solid substrate can be predicted by the spreading parameter, S , which represents the difference in surface energy per unit area between the dry substrate and the wet substrate, and is related to the surface tension at the solid-vapour (γ_{SV}), solid-liquid (γ_{SL}) and liquid-vapour (γ) interfaces:⁶⁰

$$S = \gamma_{SV} - (\gamma_{SL} + \gamma) \quad (1.1)$$

At a macroscopic level, the surface tension at the three interfaces depends on the equilibrium contact angle, defined as the angle at the three-phase contact line, as described by the Young's equation:

$$\gamma_{SV} = \gamma_{SL} + \gamma \cos \theta_E \quad (1.2)$$

Hence, the spreading coefficient can be rewritten as:

$$S = \gamma (\cos \theta_E - 1) \quad (1.3)$$

Depending on the sign of the spreading parameter, two different wetting regimes can be identified: total wetting and partial wetting (Figure 1.5).⁶¹ In complete wetting, the parameter S is positive and the liquid spreads completely on the substrate forming a continuous film with equilibrium contact angle $\theta_E = 0$. In partial wetting, S is negative and the liquid does not spread and forms isolated droplets on the surface with $\theta_E > 0$.

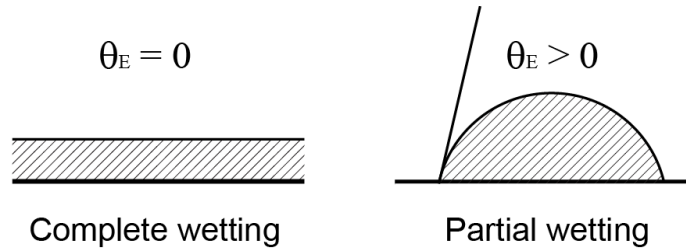


Figure 1.5. Schematic of the wetting regimes of a liquid on top of a solid substrate. (a) In complete wetting the liquid spreads on the surface and the equilibrium contact angle $\theta_E = 0$. (b) In partial wetting the equilibrium contact angle $\theta_E > 0$.

At the microscopic level, the interaction of a liquid film with a solid surface, and the resulting macroscopic effects (e.g. wetting/dewetting) can be described in terms of competing short range and long range forces.⁶² Short range forces are mainly steric repulsion interactions and, in the case of two planar surfaces, vary as $1 / r^8$. Long range forces – mainly van der Waals interactions – vary as $1 / r^2$ for planar surfaces and act significantly on distances up to about 100 nm. Both short range and long range interactions are accounted into the effective interface potential, $\phi(h)$, defined as the excess free energy per unit area necessary to bring two interfaces from infinity to a certain separation (h). For a liquid film on a solid substrate, the interface potential is:

$$\phi(h) = \frac{C}{h^8} - \frac{A}{12\pi h^2} \quad (1.4)$$

where C denotes the strength of the repulsive interaction, h the distance between the solid-liquid interface and the liquid-gas interface, i.e. the film thickness, and A is the Hamaker constant, which represents the strength of the attractive interaction. The effective interface potential describes the macroscopic behaviour of a thin liquid film in terms of surface and intermolecular interactions, hence predicting whether the film is stable, unstable or metastable (Figure 1.6).

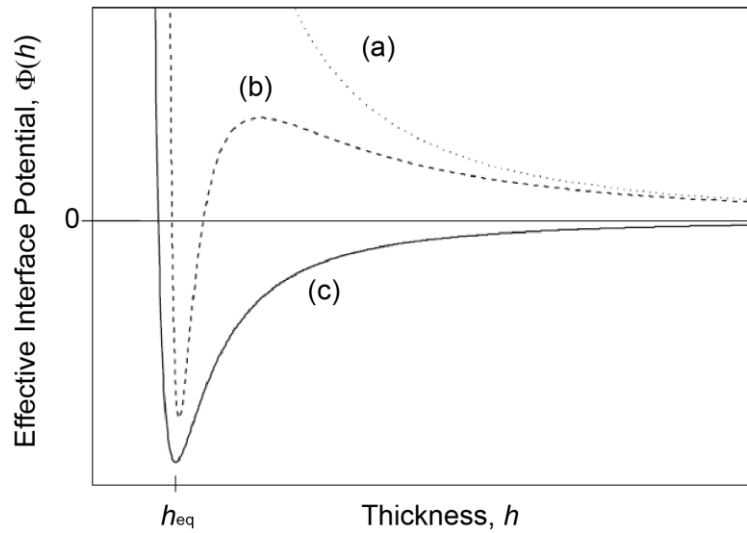


Figure 1.6. Effective interface potential $\phi(h)$ as a function of the film thickness.⁵⁹ Curve (a) represents the case of stable film, curve (b) represents the case of a metastable film, and curve (c) represents the case of an unstable film. The equilibrium film thickness is indicated as h_{eq} .

The effective interface potential of unstable and metastable films exhibits a global minimum at $h = h_{\text{eq}}$, and films thicker than h_{eq} will spontaneously dewet the substrate in order to reach the equilibrium film thickness, typically in the sub-nanometre range. In the case of metastable films, the system has to overcome a potential barrier in order to reach the state of lowest energy, and some kind of nucleus is required to lower $\phi(h)$ and induce dewetting. The effective interface potential of stable films does not exhibit any minimum and the resulting equilibrium film thickness is infinite, since energy would be necessary to thin the film.

Only liquid films thinner than the capillary length, λ_{cap} , can undergo dewetting, as in films thicker than this critical length the gravitational forces dominate over the intermolecular interactions and suppress dewetting. The capillary length of a liquid is defined as:

$$\lambda_{\text{cap}} = \sqrt{\frac{\gamma}{\rho g}} \quad (1.5)$$

where γ is the surface tension at the liquid-vapour interface, ρ is the liquid density and g is the gravitational acceleration. For water λ_{cap} is about 2.7 mm.⁶³

1.3.2. Evolution of dewetting

Two possible mechanisms for the dewetting of thin liquid films can be distinguished: spinodal dewetting and heterogeneous nucleation of holes followed by hole growth (Figure 1.7). Spinodal dewetting, predicted for the first time by Vrij in 1966, occurs only in unstable films.⁶⁴ The film instability drives the formation of capillary waves whose amplitude grows exponentially with time as $e^{t/\tau}$, where τ is the characteristic growth time. This produces a pattern of spatially correlated micro and nanostructures with characteristic wavelength λ_s . Since the growth time τ varies as the fifth power of the films thickness, spinodal dewetting can be observed only in ultrathin liquid films (typically less than 10 nm thick). For films thicker than 10 nm, the growth time of the instability is too slow and heterogeneous nucleation usually overtakes spinodal dewetting.⁶⁵

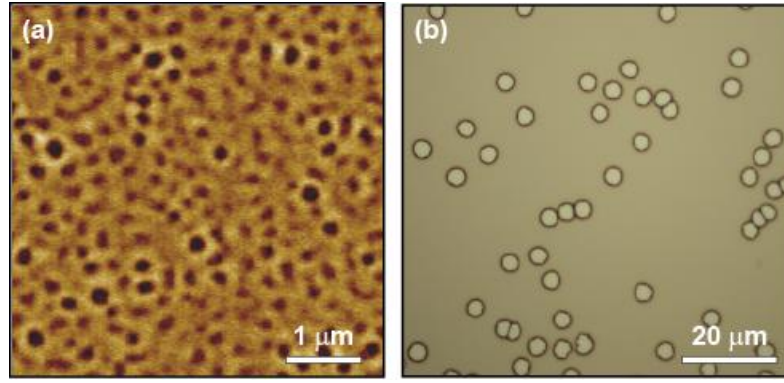


Figure 1.7. Onset of dewetting: mechanisms of film rupture. (a) Atomic force microscopy (AFM) topography image of spinodal dewetting in a 4 nm thick polystyrene film on silicon. (b) Optical micrograph of heterogeneous nucleation in a 33 nm thick polystyrene film on silicon.

The dewetting of thin liquid films by heterogeneous nucleation can be divided into three stages (Figure 1.8): (i) film rupture, (ii) hole growth and (iii) formation of isolated droplets.^{66, 67} The rupture of the initially homogeneous film by nucleation of holes represents the onset of dewetting. In heterogeneous nucleation, characteristic of most unstable and metastable films, dewetting starts with the random nucleation of holes at sites of local heterogeneity in the liquid film, typically defect sites (e.g. dust particles) or sites with high residual stress in the case of thin polymer films.^{68, 69}

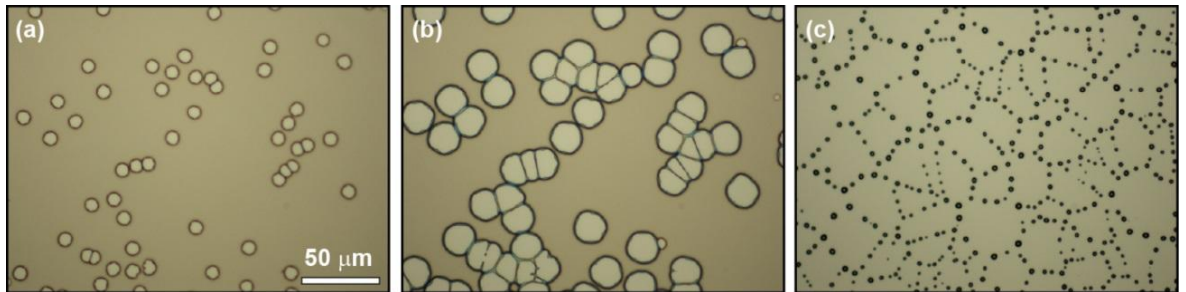


Figure 1.8. Optical micrographs of the three stages of dewetting in polystyrene thin films on silicon: (a) film rupture, (b) hole growth, and (c) formation of isolated droplets.

After film rupture, the holes nucleated on the liquid film grow in lateral size in order to minimize the contact area between the liquid and the solid substrate. Growth occurs by displacement of material away from the nuclei, leading to accumulation of

material into a rim surrounding the hole (Figure 1.9). In the early stages of dewetting, the energy is dissipated mainly by slippage of the liquid film on the solid substrate (full slip regime) and the radius of the hole grows with time as $t^{2/3}$. In later stages of dewetting, viscous dissipation within the liquid films dominates the hole growth (no slip regime) and the radius of the hole grows linearly with time.^{70, 71} In both regimes, the rate of hole growth is inversely proportional to the viscosity of the liquid film, and therefore the dewetting rate increases with increasing the annealing temperature as a consequence of the increase in fluidity of liquid.⁶⁷

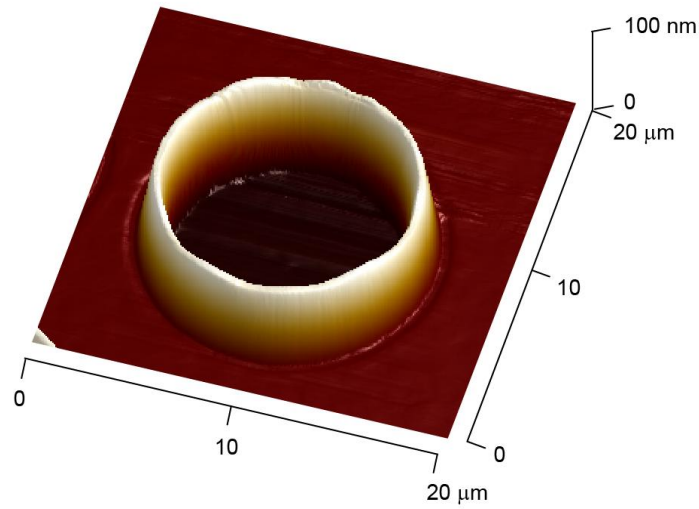


Figure 1.9. 3D rendering of an atomic force microscopy topography image illustrating the typical morphology of an isolated hole during dewetting .

The late stage of dewetting starts when holes cannot grow any further as they coalesce with neighbouring holes. Upon coalescence, the rims of the two holes overlap to form a liquid cylinder, which eventually decays into single droplets due to Rayleigh-Plateau instability. In the final state, isolated droplets of liquid are found on the solid substrate as spherical caps, with Young's equilibrium contact angle (Figure 1.10).⁷²

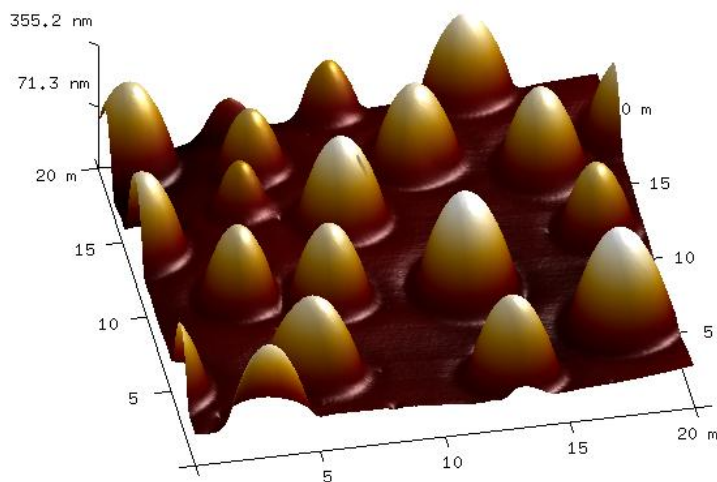


Figure 1.10. 3D rendering of an atomic force microscopy topography image illustrating the final stage of dewetting in polystyrene droplets on silicon.

1.3.3. Surface micropatterning by dewetting

In several instances, dewetting is undesirable, as in the rupture of a protective coating film or paint. However, dewetting represents a powerful tool to produce surface micropatterns and there are several examples of the application of dewetting in micro and nanotechnology. Surface patterning by dewetting of thin polymer films is an intrinsically up-scalable method, which could be applied to objects of any shape and size, as the only requirement for patterning is a uniform polymer coating on the object (achievable for example by dip-coating), and thermal annealing of the polymer films. The size of the dewetting patterns can be controlled simply by tuning the annealing conditions (temperature and time). By cooling the polymer films down to room temperature, dewetting can be stopped at any stage of hole growth: the longer the annealing time (or the higher the annealing temperature), the larger the holes.

Dewetting phenomena are universal and have been observed on a variety of inorganic, organic, polymeric and hybrid materials. Dewetting of thin metallic Pt/Fe films on MgO was exploited by Breitling and Goll⁷³ to fabricate isolated single-domain island structures with increased magnetic coercivity, for potential use in magnetic recording applications. Dewetting has been proposed as a viable tool to pattern nanoparticles.⁷⁴ Suematsu *et al.*⁷⁵ exploited the dewetting of polystyrene (PS) solutions containing Ag nanoparticles on mica to generate two-dimensional hexagonal patterns of PS droplets with ring-shaped aggregates of the nanoparticles. The combination of self-

assembling and dewetting was exploited by van Hameren *et al.*⁷⁶ to produce large-scale sub-micrometer wire-like architectures consisting of porphyrin columnar stacks. Dewetting has been proposed as a tool for patterning biological molecules for biological applications. Telford *et al.*⁷⁷ reported the use of surface patterns produced by dewetting of thin polymer films for site-selective protein adsorption and cell immobilization.

Patterns arising from the dewetting of thin liquid films typically consist in randomly distributed holes with narrow size distribution. However, for applications requiring surface patterns with lateral order, it is possible to force the dewetting to occur in an ordered fashion by introducing external factors (e.g. chemical and/or physical heterogeneities) to locally modify the interfacial potential. Some of the approaches used to spatially control the dewetting of functional materials are presented in the next section.

1.3.4. Spatially controlled dewetting patterns

The presence of physical or chemical heterogeneities on the surface introduces local changes in the interfacial potential and favours the nucleation of holes at specific location of the liquid film. There are several examples in the literature of spatially controlled dewetting patterns obtained by dewetting on physically pre-patterned substrates.⁷⁸⁻⁸⁰ Higgins and Jones⁸¹ demonstrated the possibility to achieve polymeric films with oriented morphologies by anisotropic spinodal dewetting on rubbed glass slides. Yoon *et al.*⁸² showed the dewetting of thin polystyrene films on topographic pre-patterned silica substrates and systematically investigated the morphological evolution of the film by controlling size and type of the topographic patterns (Figure 1.11a). Mukherjee *et al.*⁸³ investigated the creation of large area mesoscale structures by controlling the dewetting pathways of thin polymer films on physically heterogeneous substrates comprising two-dimensional arrays of square pillars. The controlled dewetting of metallic thin films is effective for fabrication of ordered micro and nano-structures with relevant technological applications. Oh *et al.*⁸⁴ used the dewetting of thin cobalt layers on topographically pre-patterned silicon substrates for the fabrication of ordered nanoparticle arrays. Petersen and Mayr⁸⁵ showed the formation of nanowires by thermal dewetting of Ni and NiAg solid thin films on ripple-patterned silicon substrates.

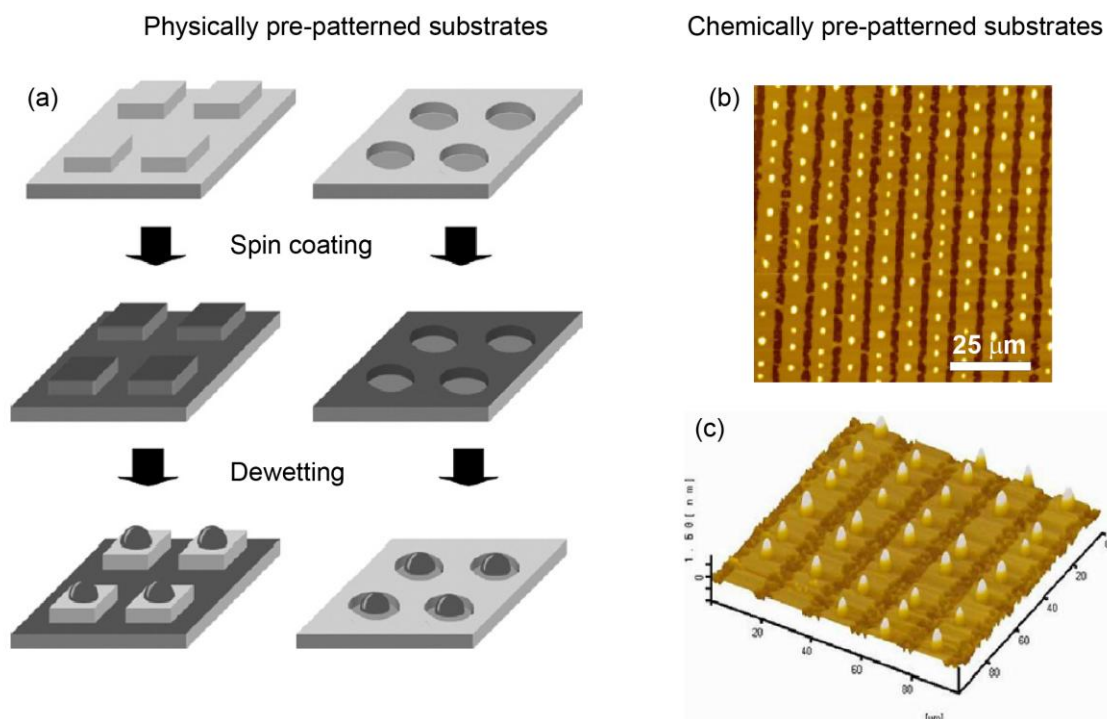


Figure 1.11. Examples of spatially controlled dewetting on pre-patterned substrates. (a) Schematic of ordered dewetting patterns on physically pre-patterned substrates.⁸² (b-c) Atomic force microscope (AFM) images of linear arrays of polymer droplets obtained by dewetting on chemically pre-patterned substrates.⁸⁶

Modification of the substrate with ordered chemical patterns was employed to drive the dewetting of liquid films to specific areas exclusively.^{87, 88} Dewetting of thin polymer films on pre-patterned surfaces by microcontact printing of self-assembled monolayers (SAM) was extensively employed for the fabrication of arrays of polymer droplets mirroring the topography of the SAM (Figure 1.11b and Figure 1.11c).^{86, 89, 90} Kumar and Whitesides⁹¹ have demonstrated the use of pre-patterned substrates as base for diffraction gratings. Heterogeneous substrates comprising well-defined hydrophilic and hydrophobic regions with micrometer-scale periodicity were prepared by patterning alkenethiolates SAM on gold. Condensation of water on the patterned surfaces resulted in droplets following the pattern of the hydrophilic SAM. The same procedure, followed by dipping and dewetting of polymer-coated magnetic nanoparticles, was used for the fabrication of ordered arrays of magnetic rings with potential application in data storage technologies.⁹²

Other techniques used in combination with dewetting to produce ordered surface patterns include microimprinting.⁹³ In this technique, a stamp is placed in contact with a polymer film and heated to a temperature higher than the glass transition temperature of the polymer, causing the features of the stamp to sink into the polymer melt. Dewetting starts where the film thickness is the thinnest, i.e. at the locations where the imprinting takes place, producing a dewetting pattern that mirrors the features of the stamp. Kim and Lee⁹⁴ showed the ability to achieve polystyrene patterns with size ranging from tens to hundreds of nanometers by controlling the time of microimprinting. Park *et al.*⁹⁵ showed that the dewetting of Teflon precursors confined by saw-toothed PDMS stamps can be used to produce highly ordered patterns of Teflon nanospheres with precise size control. Yoon *et al.*⁹⁶ used microimprinting to topographically pattern poly(4-vinylpyridine) (P4VP) / polystyrene (PS) bilayers. The subsequent annealing above the glass transition temperature started the dewetting of the P4VP top layer as well as the partial layer inversion of the two layers, producing an ordered array of PS microlenses.

1.4. Thesis Outline

This Thesis describes the design and fabrication of polymer surfaces featuring chemical and topographical micropatterns. Surface micropatterning was achieved by exploiting the self-assembly of thin polymer films based on dewetting phenomena. The materials and methodologies common to all the experimental work presented in this Thesis are summarized in Chapter 2, including sample preparation protocols and surface characterization methods.

The development of micropatterned polymer coatings for site-specific protein adsorption is presented in Chapter 3. In this study, chemical and topographical patterns with good protein adsorption contrast were achieved by the combination of grafting of polymer brushes and polymer dewetting. In particular, dense brushes of highly protein-repellent poly(ethylene glycol) (PEG) brushes were grafted onto poly(D,L-lactide-co-glycolide) (PLGA) films, previously patterned by spontaneous dewetting on top of polystyrene (PS) films. The protein absorptivity and the biodegradability of the novel PEG-grafted PLGA films was investigated and site-selective protein adsorption was achieved on the micropatterned substrates.

Two approaches to inducing spatially-ordered dewetting patterns are contained in Chapters 4 and 5. The guided dewetting of PS thin films on chemically pre-patterned substrates is presented in Chapter 4. In this study, different stages of dewetting were exploited to produce different types of ordered patterns. The dynamics of hole growth in the early stages of dewetting was investigated to determine the effect of the chemical pre-pattern on the dewetting rate.

The development of spatially-ordered surface patterns produced by the combination of colloidal imprinting and polymer dewetting is presented in Chapter 5. Colloidal imprinting with colloidal two-dimensional colloidal crystals was used to pattern poly(vinyl pyridine)/polystyrene (P4VP/PS) bilayers with ordered arrays of holes. Both single-particle and binary colloidal crystals were employed as patterning templates. The size and the depth of the holes produced by colloidal imprinting were tuned by dewetting of the P4VP top layer upon thermal annealing. The interplay between polymer dewetting and layer inversion in imprinted bilayers, and the effect of the wettability of the polymer films were investigated.

Finally, in Chapter 6, the findings are summarized and overall conclusions drawn.

References

1. Singh, T. B.; Sariciftci, N. S. Progress in plastic electronics devices. In *Annual Review of Materials Research*; Annual Reviews: Palo Alto, 2006; Vol. 36, pp 199-230.
2. Black, C. T.; Ruiz, R.; Breyta, G.; Cheng, J. Y.; Colburn, M. E.; Guarini, K. W.; Kim, H. C.; Zhang, Y. Polymer self assembly in semiconductor microelectronics. *Ibm Journal of Research and Development* **2007**, 51 (5), 605-633.
3. Valkama, S.; Kosonen, H.; Ruokolainen, J.; Haatainen, T.; Torkkeli, M.; Serimaa, R.; Ten Brinke, G.; Ikkala, O. Self-assembled polymeric solid films with temperature-induced large and reversible photonic-bandgap switching. *Nature Materials* **2004**, 3 (12), 872-876.
4. Campbell, M.; Sharp, D. N.; Harrison, M. T.; Denning, R. G.; Turberfield, A. J. Fabrication of photonic crystals for the visible spectrum by holographic lithography. *Nature* **2000**, 404 (6773), 53-56.

5. Thery, M.; Racine, V.; Pepin, A.; Piel, M.; Chen, Y.; Sibarita, J. B.; Bornens, M. The extracellular matrix guides the orientation of the cell division axis. *Nature Cell Biology* **2005**, 7 (10), 947-U29.
6. Alves, N. M.; Pashkuleva, I.; Reis, R. L.; Mano, J. F. Controlling cell behavior through the design of polymer surfaces. *Small* **2010**, 6 (20), 2208-2220.
7. Thery, M. Micropatterning as a tool to decipher cell morphogenesis and functions. *Journal of Cell Science* **2010**, 123 (24), 4201-4213.
8. Franke, K.; Kurth, I.; Bornhaeuser, M.; Werner, C.; Pompe, T. Biomimetic microcavities based on poly(dimethylsiloxane) elastomers. *Soft Matter* **2009**, 5 (18), 3505-3510.
9. Thery, M.; Racine, V.; Piel, M.; Pepin, A.; Dimitrov, A.; Chen, Y.; Sibarita, J. B.; Bornens, M. Anisotropy of cell adhesive microenvironment governs cell internal organization and orientation of polarity. *Proceedings of the National Academy of Sciences of the United States of America* **2006**, 103 (52), 19771-19776.
10. Kurth, I.; Franke, K.; Pompe, T.; Bornhaeuser, M.; Werner, C. Extracellular matrix functionalized microcavities to control hematopoietic stem and progenitor cell fate. *Macromolecular Bioscience* **2011**, 11 (6), 739-747.
11. Whitesides, G. M. The origins and the future of microfluidics. *Nature* **2006**, 442 (7101), 368-373.
12. Manz, A.; Harrison, D. J.; Verpoorte, E. M. J.; Fetting, J. C.; Paulus, A.; Ludi, H.; Widmer, H. M. Planar chips technology for miniaturization and integration of separation techniques into monitoring systems - capillary electrophoresis on a chip. *Journal of Chromatography* **1992**, 593 (1-2), 253-258.
13. Dittrich, P. S.; Manz, A. Lab-on-a-chip: microfluidics in drug discovery. *Nature Reviews Drug Discovery* **2006**, 5 (3), 210-218.
14. de Mello, A. J. Control and detection of chemical reactions in microfluidic systems. *Nature* **2006**, 442 (7101), 394-402.
15. Song, H.; Chen, D. L.; Ismagilov, R. F. Reactions in droplets in microfluidic channels. *Angewandte Chemie-International Edition* **2006**, 45 (44), 7336-7356.
16. McDonald, J. C.; Duffy, D. C.; Anderson, J. R.; Chiu, D. T.; Wu, H. K.; Schueller, O. J. A.; Whitesides, G. M. Fabrication of microfluidic systems in poly(dimethylsiloxane). *Electrophoresis* **2000**, 21 (1), 27-40.
17. Lee, T.; Charraut, E.; Neto, C. Interfacial slip on rough, patterned and soft surfaces: A review of experiments and simulations. *Advances in Colloid and Interface Science* **2014**, 210, 21-38.
18. Ito, T.; Okazaki, S. Pushing the limits of lithography. *Nature* **2000**, 406 (6799), 1027-1031.
19. Bates, A. K.; Rothschild, M.; Bloomstein, T. M.; Fedynyshyn, T. H.; Kunz, R. R.; Liberman, V.; Switkes, M. Review of technology for 157-nm lithography. *Ibm Journal of Research and Development* **2001**, 45 (5), 605-614.

20. Muller, C. D.; Falcou, A.; Reckefuss, N.; Rojahn, M.; Wiederhirn, V.; Rudati, P.; Frohne, H.; Nuyken, O.; Becker, H.; Meerholz, K. Multi-colour organic light-emitting displays by solution processing. *Nature* **2003**, *421* (6925), 829-833.
21. Wu, H. K.; Odom, T. W.; Whitesides, G. M. Reduction photolithography using microlens arrays: Applications in gray scale photolithography. *Analytical Chemistry* **2002**, *74* (14), 3267-3273.
22. Koh, W. G.; Revzin, A.; Pishko, M. V. Poly(ethylene glycol) hydrogel microstructures encapsulating living cells. *Langmuir* **2002**, *18* (7), 2459-2462.
23. Revzin, A.; Tompkins, R. G.; Toner, M. Surface engineering with poly(ethylene glycol) photolithography to create high-density cell arrays on glass. *Langmuir* **2003**, *19* (23), 9855-9862.
24. Albrecht, D. R.; Tsang, V. L.; Sah, R. L.; Bhatia, S. N. Photo- and electropatterning of hydrogel-encapsulated living cell arrays. *Lab on a Chip* **2005**, *5* (1), 111-118.
25. Nie, Z. H.; Kumacheva, E. Patterning surfaces with functional polymers. *Nature Materials* **2008**, *7* (4), 277-290.
26. Menard, E.; Meitl, M. A.; Sun, Y. G.; Park, J. U.; Shir, D. J. L.; Nam, Y. S.; Jeon, S.; Rogers, J. A. Micro- and nanopatterning techniques for organic electronic and optoelectronic systems. *Chemical Reviews* **2007**, *107* (4), 1117-1160.
27. Guo, L. J. Nanoimprint lithography: Methods and material requirements. *Advanced Materials* **2007**, *19* (4), 495-513.
28. Behl, M.; Seekamp, J.; Zankovych, S.; Torres, C. M. S.; Zentel, R.; Ahopelto, J. Towards plastic electronics: Patterning semiconducting polymers by nanoimprint lithography. *Advanced Materials* **2002**, *14* (8), 588-591.
29. Finder, C.; Beck, M.; Seekamp, J.; Pfeiffer, K.; Carlberg, P.; Maximov, I.; Reuther, F.; Sarwe, E. L.; Zankovych, S.; Ahopelto, J.; Montelius, L.; Mayer, C.; Torres, C. M. S. Fluorescence microscopy for quality control in nanoimprint lithography. *Microelectronic Engineering* **2003**, *67-8*, 623-628.
30. Li, H. W.; Huck, W. T. S. Ordered block-copolymer assembly using nanoimprint lithography. *Nano Letters* **2004**, *4* (9), 1633-1636.
31. Colburn, M.; Suez, I.; Choi, B. J.; Meissl, M.; Bailey, T.; Sreenivasan, S. V.; Ekerdt, J. G.; Willson, C. G. Characterization and modeling of volumetric and mechanical properties for step and flash imprint lithography photopolymers. *Journal of Vacuum Science & Technology B* **2001**, *19* (6), 2685-2689.
32. Kumar, A.; Whitesides, G. M. Features of gold having micrometer to centimeter dimensions can be formed through a combination of stamping with an elastomeric stamp and an alkanethiol ink followed by chemical etching. *Applied Physics Letters* **1993**, *63* (14), 2002-2004.
33. Quist, A. P.; Pavlovic, E.; Oscarsson, S. Recent advances in microcontact printing. *Analytical and Bioanalytical Chemistry* **2005**, *381* (3), 591-600.

34. Gates, B. D.; Xu, Q. B.; Stewart, M.; Ryan, D.; Willson, C. G.; Whitesides, G. M. New approaches to nanofabrication: Molding, printing, and other techniques. *Chemical Reviews* **2005**, *105* (4), 1171-1196.
35. Shah, R. R.; Merreceyes, D.; Husemann, M.; Rees, I.; Abbott, N. L.; Hawker, C. J.; Hedrick, J. L. Using atom transfer radical polymerization to amplify monolayers of initiators patterned by microcontact printing into polymer brushes for pattern transfer. *Macromolecules* **2000**, *33* (2), 597-605.
36. Zhou, F.; Chen, M.; Liu, W. M.; Liu, J. X.; Liu, Z. L.; Mu, Z. G. Fabrication of positively patterned conducting polymer microstructures via one-step electrodeposition. *Advanced Materials* **2003**, *15* (16), 1367-1370.
37. Kumar, G.; Wang, Y. C.; Co, C.; Ho, C. C. Spatially controlled cell engineering on biomaterials using polyelectrolytes. *Langmuir* **2003**, *19* (25), 10550-10556.
38. Lin, C. C.; Co, C. C.; Ho, C. C. Micropatterning proteins and cells on polylactic acid and poly(lactide-co-glycolide). *Biomaterials* **2005**, *26* (17), 3655-3662.
39. Piner, R. D.; Zhu, J.; Xu, F.; Hong, S. H.; Mirkin, C. A. "Dip-pen" nanolithography. *Science* **1999**, *283* (5402), 661-663.
40. Xu, P.; Uyama, H.; Whitten, J. E.; Kobayashi, S.; Kaplan, D. L. Peroxidase-catalyzed in situ polymerization of surface orientated caffeic acid. *Journal of the American Chemical Society* **2005**, *127* (33), 11745-11753.
41. Yang, M.; Sheehan, P. E.; King, W. P.; Whitman, L. J. Direct writing of a conducting polymer with molecular-level control of physical dimensions and orientation. *Journal of the American Chemical Society* **2006**, *128* (21), 6774-6775.
42. Lim, J. H.; Mirkin, C. A. Electrostatically driven dip-pen nanolithography of conducting polymers. *Advanced Materials* **2002**, *14* (20), 1474-1477.
43. McKendry, R.; Huck, W. T. S.; Weeks, B.; Florini, M.; Abell, C.; Rayment, T. Creating nanoscale patterns of dendrimers on silicon surfaces with dip-pen nanolithography. *Nano Letters* **2002**, *2* (7), 713-716.
44. Maynor, B. W.; Filocamo, S. F.; Grinstaff, M. W.; Liu, J. Direct-writing of polymer nanostructures: Poly(thiophene) nanowires on semiconducting and insulating surfaces. *Journal of the American Chemical Society* **2002**, *124* (4), 522-523.
45. Lee, K. B.; Park, S. J.; Mirkin, C. A.; Smith, J. C.; Mrksich, M. Protein nanoarrays generated by dip-pen nanolithography. *Science* **2002**, *295* (5560), 1702-1705.
46. Lee, S. W.; Oh, B. K.; Sanedrin, R. G.; Salaita, K.; Fujigaya, T.; Mirkin, C. A. Biologically active protein nanoarrays generated using parallel dip-pen nanolithography. *Advanced Materials* **2006**, *18* (9), 1133-1136.
47. Sirringhaus, H.; Kawase, T.; Friend, R. H.; Shimoda, T.; Inbasekaran, M.; Wu, W.; Woo, E. P. High-resolution inkjet printing of all-polymer transistor circuits. *Science* **2000**, *290* (5499), 2123-2126.

48. Bonaccorso, E.; Butt, H. J.; Hankeln, B.; Niesenhaus, B.; Graf, K. Fabrication of microvessels and microlenses from polymers by solvent droplets. *Applied Physics Letters* **2005**, 86 (12), 124101-124101.
49. Carter, J. C.; Alvis, R. M.; Brown, S. B.; Langry, K. C.; Wilson, T. S.; McBride, M. T.; Myrick, M. L.; Cox, W. R.; Grove, M. E.; Colston, B. W. Fabricating optical fiber imaging sensors using inkjet printing technology: A pH sensor proof-of-concept. *Biosensors & Bioelectronics* **2006**, 21 (7), 1359-1364.
50. Roth, E. A.; Xu, T.; Das, M.; Gregory, C.; Hickman, J. J.; Boland, T. Inkjet printing for high-throughput cell patterning. *Biomaterials* **2004**, 25 (17), 3707-3715.
51. Cavallini, M.; Gentili, D.; Greco, P.; Valle, F.; Biscarini, F. Micro-and nanopatterning by lithographically controlled wetting. *Nature protocols* **2012**, 7 (9), 1668-1676.
52. Cavallini, M.; Albonetti, C.; Biscarini, F. Nanopatterning Soluble Multifunctional Materials by Unconventional Wet Lithography. *Advanced Materials* **2009**, 21 (10-11), 1043-1053.
53. Deegan, R. D.; Bakajin, O.; Dupont, T. F.; Huber, G.; Nagel, S. R.; Witten, T. A. Capillary flow as the cause of ring stains from dried liquid drops. *Nature* **1997**, 389 (6653), 827-829.
54. de Gennes, P. G. Wetting – Static and dynamic. *Reviews of Modern Physics* **1985**, 57 (3), 827-863.
55. Sharma, A. Relationship of thin-film stability and morphology to macroscopic parameters of wetting in the apolar and polar systems. *Langmuir* **1993**, 9 (3), 861-869.
56. Reiter, G. Dewetting of Thin Polymer Films. *Physical Review Letters* **1992**, 68 (1), 75-80.
57. Sharma, A.; Reiter, G. Instability of thin polymer films on coated substrates: Rupture, dewetting, and drop formation. *Journal of Colloid and Interface Science* **1996**, 178 (2), 383-399.
58. Seemann, R.; Herminghaus, S.; Jacobs, K. Gaining control of pattern formation of dewetting liquid films. *Journal of Physics: Condensed Matter* **2001**, 13, 4925-4938.
59. Seemann, R.; Herminghaus, S.; Neto, C.; Schlagowski, S.; Podzimek, D.; Konrad, R.; Mantz, H.; Jacobs, K. Dynamics and structure of formation in thin polymer melt films. *Journal of Physics: Condensed Matter* **2005**, 17, S267-S290.
60. de Gennes, P. G.; Brochard-Wyart, F.; Quere, D. *Capillarity and wetting phenomena: drops, bubbles, pearls, waves*; New York, 2003.
61. Bonn, D.; Eggers, J.; Indekeu, J.; Meunier, J.; Rolley, E. Wetting and spreading. *Reviews of Modern Physics* **2009**, 81 (2), 739-805.
62. Israelachvili, J. N. *Intermolecular and surface forces*; Academic Press: Boston, 1992.

63. Hu, D. L.; Chan, B.; Bush, J. W. M. The hydrodynamics of water strider locomotion. *Nature* **2003**, 424 (6949), 663-666.
64. Vrij, A. Possible Mechanism for Spontaneous Rupture of Thin Free Liquid Films. *Discussions of the Faraday Society* **1966**, 42, 23-33.
65. Konnur, R.; Kargupta, K.; Sharma, A. Instability and morphology of thin liquid films on chemically heterogeneous substrates. *Physical Review Letters* **2000**, 84 (5), 931-934.
66. Redon, F.; Brochard-Wyart, F.; Rondelez, F. Dynamics of dewetting. *Physical Review Letters* **1991**, 66, 715-719.
67. Brochard-Wyart, F.; Martin, P.; Redon, C. Liquid/Liquid Dewetting. *Langmuir* **1993**, 9, 3682-3690.
68. Jacobs, K.; Herminghaus, S.; Mecke, K. R. Thin liquid polymer films rupture via defects. *Langmuir* **1998**, 14 (4), 965-969.
69. Reiter, G.; Hamieh, M.; Damman, P.; Slavovs, S.; Gabriele, S.; Vilmin, T.; Raphael, E. Residual stresses in thin polymer films cause rupture and dominate early stages of dewetting. *Nature Materials* **2005**, 4, 754-758.
70. Jacobs, K.; Seemann, R.; Schatz, G.; Herminghaus, S. Growth of holes in Liquid films with partial slippage. *Langmuir* **1998**, 14, 4961-4963.
71. Neto, C.; Jacobs, K. Dynamics of hole growth in dewetting polystyrene films. *Physica A - Statistical Mechanics and Its Applications* **2004**, 339 (1-2), 66-71.
72. Seemann, R.; Jacobs, K.; Blossey, R. Polystyrene nanodroplets. *Journal of Physics: Condensed Matter* **2001**, 13 (21), 4915-4923.
73. Breitling, A.; Goll, D. Hard magnetic L1(0) FePt thin films and nanopatterns. *Journal of Magnetism and Magnetic Materials* **2008**, 320 (8), 1449-1456.
74. Stannard, A. Dewetting-mediated pattern formation in nanoparticle assemblies. *Journal of Physics: Condensed Matter* **2011**, 23 (8), 083001.
75. Suematsu, N. J.; Ogawa, Y.; Yamamoto, Y.; Yamaguchi, T. Dewetting self-assembly of nanoparticles into hexagonal array of nanorings. *Journal of Colloid and Interface Science* **2007**, 310 (2), 648-652.
76. van Hameren, R.; Schon, P.; van Buul, A. M.; Hoogboom, J.; Lazarenko, S. V.; Gerritsen, J. W.; Engelkamp, H.; Christianen, P. C. M.; Heus, H. A.; Maan, J. C.; Rasing, T.; Speller, S.; Rowan, A. E.; Elemans, J.; Nolte, R. J. M. Macroscopic hierarchical surface patterning of porphyrin trimers via self-assembly and dewetting. *Science* **2006**, 314 (5804), 1433-1436.
77. Telford, A. M.; Meagher, L.; Glattauer, V.; Gengenbach, T. R.; Easton, C. D.; Neto, C. Micropatterning of polymer brushes: grafting from dewetting polymer films for biological applications. *Biomacromolecules* **2012**, 13 (9), 2989-2996.
78. Brusch, L.; Kuhne, H.; Thiele, U.; Bar, M. Dewetting of thin films on heterogeneous substrates: Pinning versus coarsening. *Physical Review E* **2002**, 66 (1).

79. Leopoldes, J.; Damman, P. From a two-dimensional chemical pattern to a three-dimensional topology through selective inversion of a liquid-liquid bilayer. *Nature Materials* **2006**, *5* (12), 957-961.
80. Herminghaus, S.; Brinkmann, M.; Seemann, R. Wetting and dewetting of complex surface geometries. In *Annual Review of Materials Research*; Annual Reviews: Palo Alto, 2008; Vol. 38, pp 101-121.
81. Higgins, A. M.; Jones, R. A. L. Anisotropic spinoidal dewetting as a route to self-assembly of patterned surfaces. *Nature* **2000**, *404*, 476-478.
82. Yoon, B.; Acharya, H.; Lee, G.; Kim, H. C.; Huh, J.; Park, C. Nanopatterning of thin polymer films by controlled dewetting on a topographic pre-pattern. *Soft Matter* **2008**, *4* (7), 1467-1472.
83. Mukherjee, R.; Bandyopadhyay, D.; Sharma, A. Control of morphology in pattern directed dewetting of thin polymer films. *Soft Matter* **2008**, *4* (10), 2086-2097.
84. Oh, Y. J.; Ross, C. A.; Jung, Y. S.; Wang, Y.; Thompson, C. V. Cobalt nanoparticle arrays made by templated solid-state dewetting. *Small* **2009**, *5* (7), 860-865.
85. Petersen, J.; Mayr, S. G. Dewetting of Ni and NiAg solid thin films and formation of nanowires on ripple patterned substrates. *Journal of Applied Physics* **2008**, *103* (2), 023520.
86. Luo, C. X.; Xing, R. B.; Zhang, Z. X.; Fu, J.; Han, Y. C. Ordered droplet formation by thin polymer film dewetting on a stripe-patterned substrate. *Journal of Colloid and Interface Science* **2004**, *269* (1), 158-163.
87. Krausch, G. Surface-induced self-assembly in thin polymer films. *Material Science and Engineering*. **1995**, *14* (1-2), 1-94.
88. Boltau, M.; Walheim, S.; Mlynek, J.; Krausch, G.; Steiner, U. Surface-induced structure formation of polymer blends on patterned substrates. *Nature* **1998**, *391* (6670), 877-879.
89. Meyer, E.; Braun, H. G. Controlled dewetting processes on microstructured surfaces - a new procedure for thin film microstructuring. *Macromolecular Materials and Engineering* **2000**, *276* (3-4), 44-50.
90. Sehgal, A.; Ferreiro, V.; Douglas, J. F.; Amis, E. J.; Karim, A. Pattern-directed dewetting of ultrathin polymer films. *Langmuir* **2002**, *18* (18), 7041-7048.
91. Kumar, A.; Whitesides, G. M. Patterned condensation figures as optical diffraction gratings. *Science* **1994**, *263* (5143), 60-62.
92. An, L. J.; Li, W.; Nie, Y. R.; Xie, B.; Li, Z. Q.; Zhang, J. H.; Yang, B. Patterned magnetic rings fabricated by dewetting of polymer-coated magnetite nanoparticles solution. *Journal of Colloid and Interface Science* **2005**, *288* (2), 503-507.
93. Gentili, D.; Foschi, G.; Valle, F.; Cavallini, M.; Biscarini, F. Applications of dewetting in micro and nanotechnology. *Chemical Society Reviews* **2012**, *41* (12), 4430-4443.

94. Kim, Y. S.; Lee, H. H. Selective dewetting for general purpose patterning. *Advanced Materials* **2003**, *15* (4), 332-334.
95. Park, H.; Russell, T. P.; Park, S. Spatial control of dewetting: Highly ordered Teflon nanospheres. *Journal of Colloid and Interface Science* **2010**, *348* (2), 416-423.
96. Yoon, B. K.; Huh, J.; Kim, H. C.; Hong, J. M.; Park, C. Ordered patterns of microimprinted bilayer polymer films with controlled dewetting and layer inversion. *Macromolecules* **2006**, *39* (3), 901-903.

Chapter 2.

Materials and Methods

2.1. Preparation of Thin Polymer Films

Sample preparation was performed in a class-100 laminar flow cabinet. Thin polymer films were prepared on prime-grade silicon wafers with a 1.9 nm thick native oxide layer (MMRC Pty Ltd, Malvern VIC Australia), typically 10 x 10 mm². Silicon wafers were thoroughly cleaned prior to polymer deposition in order to remove dust particles and organic contaminants from the surface.¹ Substrates were sonicated in high-purity ethanol and in high-purity acetone, and then blown dry with pure nitrogen. Particulate contaminants were removed with a CO₂ snow jet (Applied Surface Technologies, New Providence NJ), and then treated using a plasma cleaner (Harrick Plasma, Itacha NY, model PDC-002) to remove small traces of residual organic contaminants.

Polymer films were deposited on clean silicon substrates by spin-coating (Laurell Technologies Co., PA, model WS400B-6NPP-LITE) from diluted solutions in volatile organic solvents. In a typical experiment, 25-30 μ L of polymer solution (10-20 mg mL⁻¹) are deposited on the silicon substrate and then spun at 3000-4000 RPM. During spin-coating, the polymer solution spreads on the substrate due to centrifugal forces, while the solvent quickly evaporates leaving a uniform thin film on the substrate. The thickness, h , of polymer films obtained by spin-coating is given by:²

$$h \propto \frac{C_0 M}{\omega^{1/2}} \quad (2.1)$$

where C_0 is the concentration of the polymer solution, M is the molecular weight of the polymer and ω is the rotation speed. The typical thickness of the various polymer films used in this Thesis in function of the spin-coating parameters is reported in Table 2.1.

Table 2.1. Thickness of various polymer films in function of the spin coating parameters: molecular weight of the polymer (M_n), concentration of the polymer solution, rotational speed and solvent. PS = polystyrene; PLGA = poly(D,L-lactide-*co*-glycolide); P4VP = poly(4-vinyl pyridine).

	M_n (g mol ⁻¹)	Concentration (mg mL ⁻¹)	Speed (RPM)	Solvent	Thickness (nm)
PS	1920	20	4000	Toluene	35 ± 1
PS	96000	20	3000	Toluene	77 ± 1
PS	96000	10	3000	Toluene	55 ± 1
PLGA	50000-75000	10	3000	Acetonitrile	33 ± 1
P4VP	19000	10	3000	Ethanol	40 ± 1

2.2. Ellipsometry

Ellipsometry is an optical technique based on the measurement of the change in polarization of a light beam upon reflection from a surface.³ In our set up, the light beam emitted from a light source (a polychromatic source in the VIS-IR) is linearly polarized before interacting with the sample, and then reflected from the surface of the sample. Linearly polarized light contains equal amounts of p (parallel) and s (perpendicular) polarized light (Figure 2.1).⁴ The interaction of the light beam with the surface causes a shift both in the phase angle, Δ , and the relative amplitude, Ψ , of the two components, resulting in elliptically polarized light. The change in polarization of the light beam is determined by a second polarizer (analyser) in combination with a detector (photodiode, diode-array or photomultiplier tube).

The change in polarization is measured by the ellipsometer in terms of amplitude ratio Ψ and phase shift Δ , which are related to the complex Fresnel coefficients via the complex ellipsometric parameter, ρ :

$$\rho = \frac{R_p}{R_s} = \tan \Psi e^{i\Delta} \quad (2.2)$$

where R_p and R_s are the complex Fresnel reflection coefficients for p and s -polarized light, respectively. The complex ellipsometric parameter, ρ , can be related to the complex dielectric function, ε , of the material:

$$\varepsilon = \varepsilon' + i\varepsilon'' = \sin^2 \phi \left[1 + \left(\frac{1-\rho}{1+\rho} \right)^2 \tan^2 \phi \right] \quad (2.3)$$

where ε' is the real part of the dielectric function, ε'' is the imaginary part of the dielectric function and ϕ is the angle of incidence. The complex dielectric function, ε , contains information on the optical constants of the material and it can be related to refractive index and extinction coefficient of the surface:

$$\varepsilon' = n^2 - k^2 \quad (2.4)$$

$$\varepsilon'' = 2nk \quad (2.5)$$

where n is the refractive index and k is the extinction coefficient.

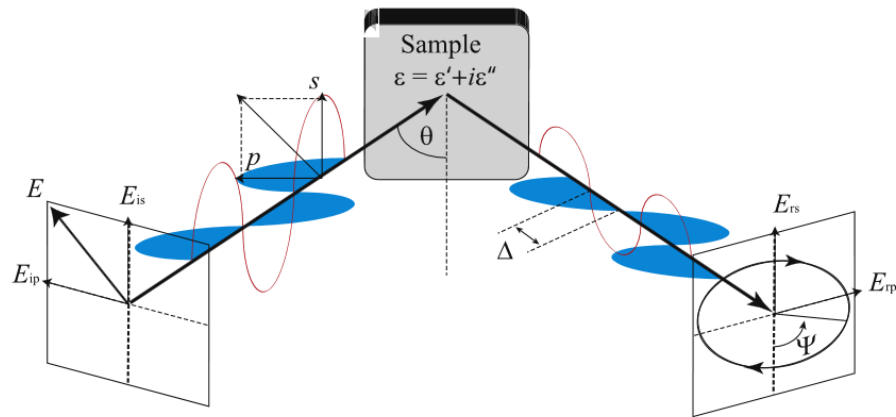


Figure 2.1. Schematic representation of the operations of an ellipsometer.⁴ (left) A linearly polarized light beam interacts with a sample with dielectric function $\varepsilon = \varepsilon' + i\varepsilon''$. (right) After reflection by the surface of the sample, the polarization of the light changes to elliptical and the changes in both the phase angle (Δ) and the amplitude ratio (Ψ) are recorded by the detector.

From the experimental Ψ and Δ values, it is possible to obtain the thickness of the film and optical constants of the material. A model must be compiled in order to generate theoretical Ψ and Δ values using Fresnel's equation, which are then used to fit the experimental Ψ and Δ values in an iterative minimum square deviation algorithm. The model used for data fitting depends on the system under investigation and is built on the knowledge of the composition and structure of the sample, e.g. number and composition of the layers and estimated refractive index of each layer.

In this Thesis, a J. A. Woollam Co. Inc. model M-2000 V ellipsometer was used to determine the thickness of the polymer films prepared by spin-coating on silicon wafers. Measurements were performed using an angle of incidence of 75° in a wavelength range of 370-1000 nm. Thickness and refractive index of the polymer films were calculated by fitting the experimental Ψ and Δ values using a model describing a multi-layer system (Figure 2.2).

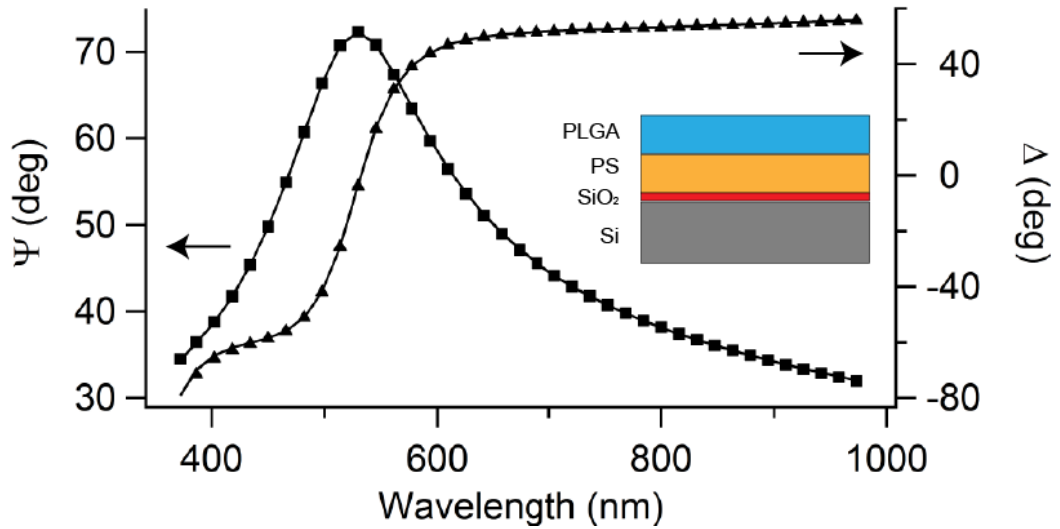


Figure 2.2. Experimental Ψ (■) and Δ (▲) values for a PLGA/PS bilayer on silicon acquired for wavelengths in the range 370-1000 nm at an angle of incidence of 75° . Experimental data were fitted (solid lines) with the multilayer model shown in the inset.

The model used to fit the ellipsometric data for a polymer bilayer (polymer 1, polymer 2) on silicon was:

$$\text{silicon} // \text{SiO}_2 // \text{polymer 1} // \text{polymer 2} \quad (2.6)$$

The refractive index of the polymer films was modelled using the Cauchy dispersion equation:

$$n(\lambda) = A_n + \frac{B_n}{\lambda^2} + \frac{C_n}{\lambda^4} + \dots \quad (2.7)$$

where $n(\lambda)$ is the refractive index; λ is wavelength of incident light; A_n , B_n and C_n are the refractive index coefficients. The contributions of the fourth term and above in the Cauchy equation were neglected as irrelevant for most applications. In order to reduce the number of fitting variables, thickness and refractive index of the polymer bottom layer (polymer 1) were measured independently before spin coating of the polymer top layer (polymer 2), using the following multilayer model:

$$\text{silicon // SiO}_2 \text{ // polymer 1} \quad (2.8)$$

Thickness and refractive index of polymer 1 were kept constant during the fitting of the ellipsometric data for the polymer bilayer. Thickness and optical constants of silicon and SiO₂ are tabulated and were kept constant during each data fitting. The data were processed and fitted using the WVASE32 softer provided with the instrument.

2.3. Atomic Force Microscopy (AFM)

Atomic force microscopy (AFM) is a type of scanning probe microscopy (SPM) developed by Binnig *et al.*⁵ in 1986 in order to overcome the limitations of scanning tunnelling microscopy (STM) to nonconductive materials. In AFM, the sample surface is scanned with a probe consisting of a sharp tip (< 20 nm) positioned at the end of a cantilever. AFM operations can be generally divided into *contact* mode and *tapping* mode. In contact mode the tip is in continuous contact with the surface, while in tapping mode the probe is driven into an oscillation at its resonant frequency by a small piezoelectric element and is in intermittent contact with the surface. The interaction of the tip with the sample surface causes the bending of the cantilever (contact mode), or the damping of the oscillation amplitude (tapping mode), in response of the repulsive or attractive forces between the sample and the tip. Bending deflection, bending oscillation, and torsion of the cantilever are monitored by an optical lever, consisting of a laser beam focused on the cantilever and reflected onto a four-quadrant photodetector (Figure 2.3). The sample is moved in a raster pattern under the tip by a piezoelectric

drive in the horizontal plane (xy plane), while the vertical motion (z distance) is controlled by a feedback mechanism. In contact mode, the feedback raises or lowers the sample and keeps the cantilever deflection at the set-point value. In tapping mode, the oscillation amplitude, which is reduced from the amplitude of the freely oscillating probe by tip-to-sample interactions, is kept at the set-point value by adjusting the vertical position of the sample with the piezoelectric drive. In both contact mode and tapping mode, the variations of the vertical position of the sample during scanning are plotted as a function of the horizontal position of the tip to create topography images, in which color contrast is used to show the variations in height of the sample surface.⁶

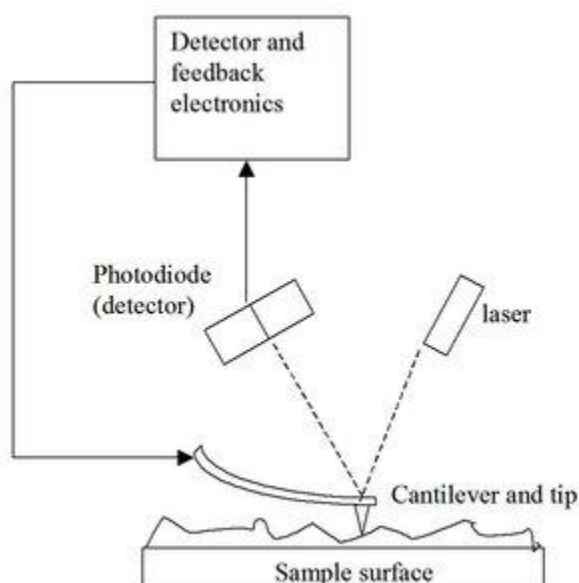


Figure 2.3. Schematic representation of the optical lever used in atomic force microscopy.⁷ The spring cantilever probes the surface, while the piezoelectric element that holds the sample moves in a raster in the xy plane. The z distance is adjusted by the feedback loop guided by the position of the laser beam reflected by the cantilever on the photodiode.

Imaging in contact mode AFM involves relatively large shear forces, frequently resulting in the damage and distortion of soft surfaces, making it unfavourable for polymeric and biological samples.⁸ In order to prevent surface damage caused by contact imaging, tapping mode AFM was developed. Shear forces associated with the raster scanning are almost eliminated in tapping mode AFM and the tip-to-sample

contact time reduced by two orders of magnitude. To date, tapping mode AFM have been extensively employed for the imaging of a wide range of soft polymeric and biological samples, offering unique advantages compared to contact mode AFM. In addition to imaging the topography of the surface, the phase shift of the cantilever in tapping mode depends on the hardness of the material, providing information on the mechanical properties of the surface.⁹

In this Thesis, tapping mode AFM was used extensively to image micropatterned polymer films (Chapters 3 and 4) and to determine the surface roughness of flat polymer films (Chapter 3). Measurements were performed with a Bruker (Billerica MA) Multimode VIII instrument, using silicon probes with nominal resonance frequency of 300 kHz and force constant of 40 N m⁻¹ (Budget Sensors, Bulgaria; model Tap300Al-G). The typical setting used for surface imaging is reported in Table 2.2.

Table 2.2. Typical setting used for the imaging of polymer surfaces with atomic force microscopy (AFM).

Imaging mode	Soft tapping in air
Scan rate	0.3 Hz
Image resolution	512 lines
Set point	200 mV
Integral gain	2.000
Proportional gain	5.000

In Chapter 5, the formation and evolution of dewetting patterns in poly(4-vinylpyridine) (P4VP) films after colloidal lithography was monitored by *in-situ* imaging with a heating/cooling AFM scanner (Bruker, model 9242JVHC), which allows to scan surfaces at temperatures up to 250 °C. During the scan, the cantilever was heated at a temperature 5-10 degrees higher than that of the heating stage in order to avoid condensation on the AFM tip.

2.4. Contact Angle Goniometry

Contact angle is a quantitative measure of the wetting of a solid by a liquid, typically water. It is defined geometrically as the angle formed by a liquid at the three-phase contact line where a liquid, solid and gas intersect.¹⁰ If the three-phase contact line is stationary, the contact angle is referred as static contact angle. When the three-phase contact line is in motion during the measurement, the contact angle is referred as advancing (droplet expansion) or receding (droplet contraction), respectively. The difference between advancing and receding contact angle represents the contact angle hysteresis, which contains information on roughness and heterogeneity of the surface.¹¹

Goniometry is the branch of surface science dedicated to the measurement of contact angles. The basic elements of a goniometer include light source, sample stage, lens and a camera. In this Thesis, the measurement of static, advancing and receding water contact angle was performed with a KSV (Helsinki, Finland) CAM200 Contact Angle System (Figure 2.4). In a typical experiment, a 4 μL water droplet was deposited on the sample surface with an automated glass syringe, and used for the measurement of the static contact angle. Advancing/receding contact angle were measured by increasing/decreasing the volume (4 μL , 0.2 $\mu\text{L s}^{-1}$) of the droplet, while capturing images of the expanding/shrinking droplet (64-128 frames, 2 fps).

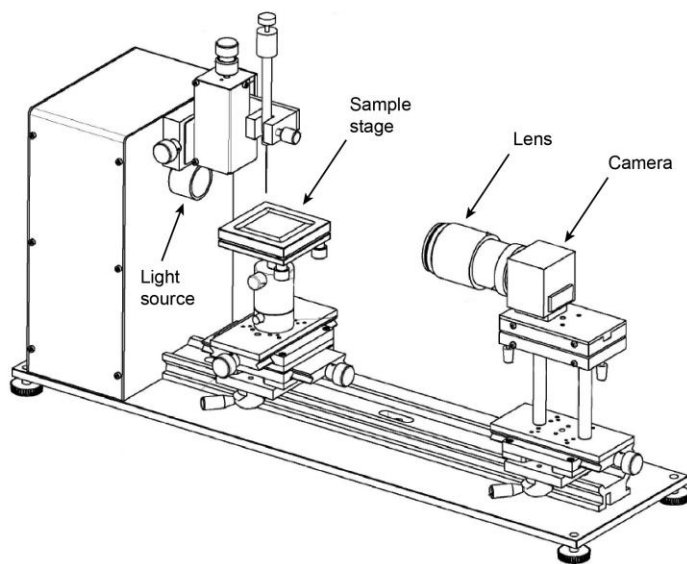


Figure 2.4. Schematic representation of a KSV CAM200 Contact Angle System. Light source, sample stage, lens and camera are indicated.

In conventional goniometry, the assessment of the contact angle consists in the measurement of the angle formed between the solid and the tangent to the drop surface. Determining the tangent line which will define the contact angle is a factor that can limit the reproducibility of the measurement. In this thesis, contact angle was measured by using computer analysis of the droplet profile by fitting the shape of the droplet with the Young-Laplace equation:

$$\Delta p = \gamma \left(\frac{1}{R_1} - \frac{1}{R_2} \right) \quad (2.9)$$

where Δp is the pressure difference across the liquid-gas interface, γ is the surface tension at the liquid-gas interface, R_1 and R_2 are the principal radii of curvature. The tangent is determined as the gradient of the Young-Laplace equation at the point where it intersects the baseline, and the contact angle is measured (Figure 2.5). Computer analysis and fitting of the droplet profile were performed with the AttensionTheta software provided with the instrument.

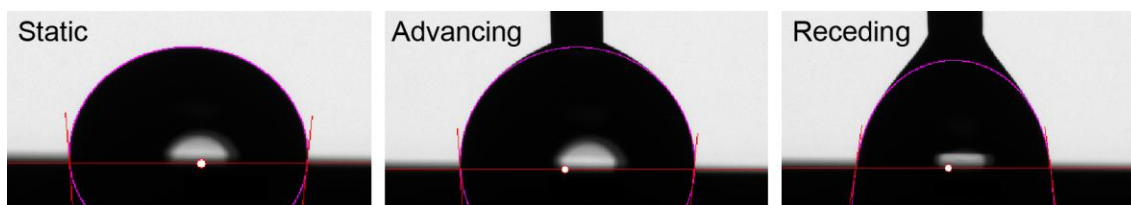


Figure 2.5. Measurement of the static, advancing, and receding contact angle by fitting of the droplet profile with the Young-Laplace equation.

2.5. Thermogravimetric Analysis (TGA) and Differential Scanning Calorimetry (DSC)

Thermogravimetric analysis (TGA) and differential scanning calorimetry (DSC) were used in this Thesis to determine the thermal properties of the polymers used. In TGA, the mass change of the sample is monitored in function of the temperature. In a typical experiment, the temperature is ramped to identify mass loss due to impurities and the temperature at which degradation occurs. In Chapter 3, TGA was employed to test the thermal stability of poly(D,L-glycolide-*co*-lactide), using a TA Instruments (New Castle, DE) model TGA 2950 instrument.

DSC monitors the heat flow within a sample in function of the temperature. It is typically used to identify phase transitions occurring in the material, such as glass transitions and melting (endothermic transition) or crystallization (exothermic transition). In this work, DSC was used to identify the glass transition temperature of poly(D,L-glycolide-*co*-lactide) (PLGA, Chapter 3) and poly(4-vinyl pyridine) (P4VP, Chapter 5). Measurements were performed with a TA Instruments (New Castle, DE) model DSC 2920 instrument.

2.6. X-Ray Photoelectron Spectroscopy (XPS)

X-ray photoelectron spectroscopy (XPS) is a quantitative spectroscopic technique used to elucidate electronic structure and elemental composition, including oxidation numbers, in a given material.^{12, 13} In this technique, monochromatic x-ray photons with energy $h\nu$ are incident on a sample, causing the emission of photoelectrons from the core energy levels of the elements present in the material. The kinetic energy, KE , of the photoelectron is given by the energy conservation as:

$$KE = h\nu - (BE + \phi) \quad (2.10)$$

where BE is the binding energy of the electron prior to the photoionization process, defined as the energy needed to bring an electron from a specific core level to the Fermi level of the material; ϕ is the work function, defined as the minimum energy needed to bring an electron from the Fermi level of a material to a point in the vacuum just outside the solid surface; KE is the kinetic energy of the photoelectron as recorded by the detector. Every chemical element has a unique photoelectron spectrum as the binding energy of photoelectrons depends on the electronic structure of the element. The binding energy of electrons does not depend only on the element and the core levels it comes from, but also on the chemical state of the element in a given compound. This dependence of the binding energy on the chemical state of the element is known as *chemical shift*.¹⁴

The intensity of the photoelectron signal is proportional to the photoionization cross-section of the specific level from which the photoionization takes place and is a function of the photon energy for any given level. The photoelectron signal is also a function of the path length that the photoionized electron has to travel through the

sample in order to reach the surface and be ejected into the vacuum. This dependency on the path length of the electron arises from the fact that the photoelectron has a finite probability to suffer collisions while travelling through the samples. Typically, the mean free path of photoelectrons is between 5 and 10 nm.

In this Thesis, XPS was used to detect the changes in surface chemistry after covalent grafting of poly(ethylene glycol) (PEG) molecules to poly(D,L-glycolide-*co*-lactide) (PLGA) films in Chapter 3. XPS analysis was performed using an AXIS Ultra DLD spectrometer (Kratos Analytical Inc.) with a monochromated Al K α source at a power of 150 W (15 kV x 10 mA) equipped with a hemispherical analyzer operating in the fixed analyzer transmission mode and standard aperture (analysis area: 0.3 x 0.7 mm²). Each sample was analyzed at an emission angle of 0° as measured from the surface normal. All elements were identified from survey spectra (acquired at pass energy of 160 eV). High resolution spectra were recorded from individual peaks at 40 eV pass energy (typical peak width for polymer: 1.0 – 1.1 eV). Nitrogen identification on aminolyzed PLGA surfaces was performed by lowering the detection limit to 0.01%, achieved by reducing the sweep range while increasing the sweep time over the N region. XPS measurements were performed by Dr Christopher D. Easton at the facilities in CSIRO Clayton VIC.

2.7. Quartz Crystal Microbalance with Dissipation Monitoring (QCM-D)

The quartz crystal microbalance (QCM) is a nanogram-sensitive technique that uses acoustic waves generated by oscillating a piezoelectric quartz crystal to measure mass.^{15, 16} The basis of QCM operation is related to quartz's inherent property of piezoelectricity: by applying alternating electric fields to quartz, an alternating expansion-contraction of the crystal lattice is induced. QCM sensors consist of an AT-cut quartz crystal sandwiched between two gold electrodes, and resonance is excited when a sufficient AC voltage is applied with a frequency close to the resonant frequency, f_0 , of the crystal. The resonant condition of QCM occurs when the standing wave produced by the alternating expansion and contraction is an odd integer of the thickness of the quartz crystal.

The quartz crystal microbalance became widely used as a mass balance after the theoretical and experimental work by Sauerbrey¹⁷ in 1959, demonstrating the relation between the frequency change (Δf) in the oscillating crystal and the mass adsorbed (Δm) on the surface of the crystal. This relationship is given by:

$$\Delta m = \frac{C}{n} \Delta f \quad (2.11)$$

where n is the harmonic number and C is a constant given by:

$$C = \frac{t_q \rho_q}{f_0} \quad (2.12)$$

with t_q and ρ_q being the thickness and the density of quartz, respectively, and f_0 being the fundamental resonant frequency. For quartz crystals with $f_0 = 5$ MHz, the constant C equals $-17.7 \text{ Hz ng cm}^{-2}$.

The Sauerbrey equation was developed for monitoring the deposition of metals from the gas phase and, although it can be extended to applications in liquid, it is strictly valid only when the adsorbed mass forms a rigid layer on the quartz crystal. However, in many liquid applications, the adsorbed material often shows viscous and elastic contributions to the frequency change, due for example to the entrapment of solvent in the adsorbed layer. Film viscoelasticity can be investigated by monitoring the dissipation parameter (D), which represents the decay of the crystal's oscillation after excitation close to the resonant frequency.¹⁸ The dissipation parameter is defined as:

$$D = \frac{E_{Dissipated}}{2\pi E_{Stored}} \quad (2.13)$$

where $E_{Dissipated}$ is the energy dissipated during one oscillatory cycle and E_{Stored} is the energy stored in the oscillating system. The viscoelastic data obtained from the dissipation allow a broader characterization of the complex systems, such as biological samples and polymers.¹⁹

In this Thesis, QCM-D was used to monitor the adsorption of proteins on poly(D,L-glycolide-*co*-lactide) (PLGA) before and after the grafting of poly(ethylene glycol) (PEG) chains (Chapter 5). Measurements were performed using a Q-Sense (Gothenburg, Sweden) QCM-D model E4. QCM sensors ($f_0 = 5$ MHz) were equilibrated in phosphate buffer saline (PBS) for 2 hours prior to injecting a 2 mg mL^{-1} BSA

solution in PBS (0.1 mL min^{-1} , 15 min). The protein solution was left in contact with the QCM sensor for 2 hours to allow adsorption on the surface and equilibration of the signal, and then rinsed with PBS buffer to remove unbound proteins.

The QCM raw data from a typical protein adsorption experiment exhibit little frequency shift splitting (Δf_n) and low dissipation values (D_n) for the various harmonics of the fundamental frequency after both protein adsorption and rinse with buffer (Figure 2.6). This indicates the formation of a rigid layer on the quartz crystal and allowed the quantification of the adsorbed protein using the Sauerbrey equation. The third harmonic of the fundamental frequency was used for the calculations because of the reduced noise and baseline drift.

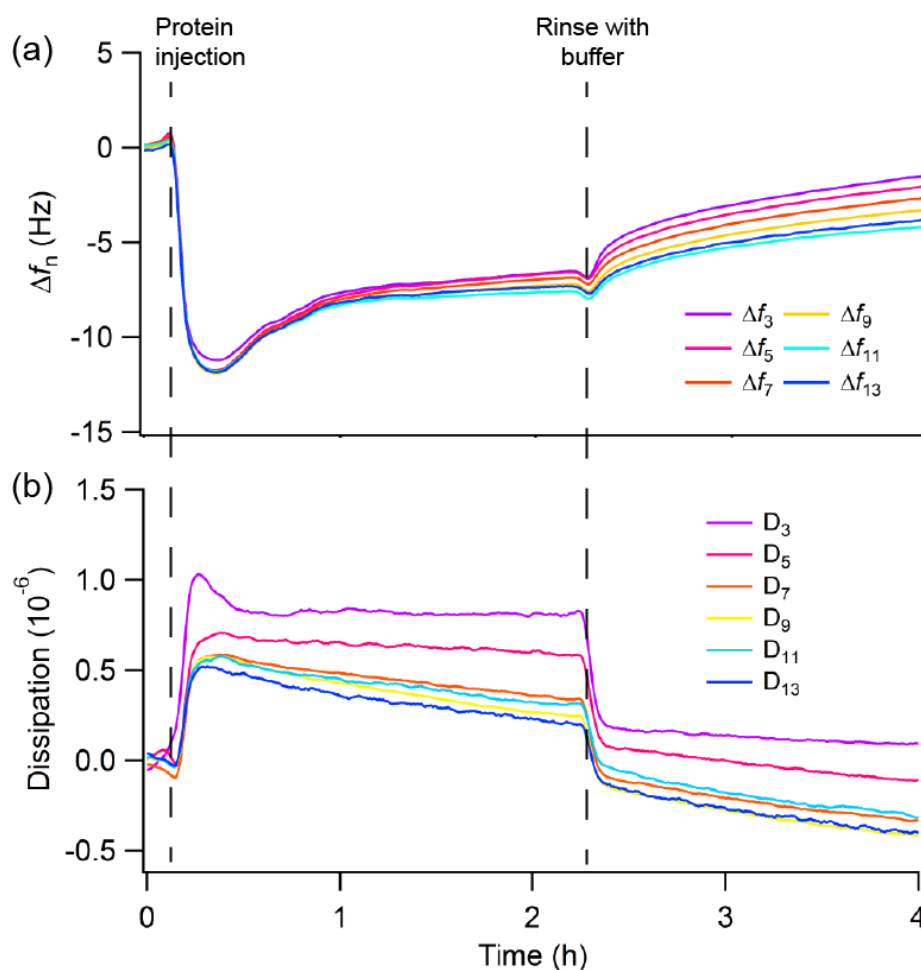


Figure 2.6. QCM raw data from a typical protein adsorption experiment: (a) frequency shift and (b) dissipation for various harmonics of the fundamental frequency of the quartz sensor.

References

1. Muller-Buschbaum, P., Influence of surface cleaning on dewetting of thin polystyrene films. *European Physical Journal E* **2003**, *12*, 443-448.
2. Lawrence, C. J., The mechanics of spin coating of polymer-films. *Physics of Fluids* **1988**, *31*, 2786-2795.
3. Jenkins, T. E., Multiple-angle-of-incidence ellipsometry. *Journal of Physics D: Applied Physics* **1999**, *32*, R45-R56.
4. Langereis, E.; Heil, S. B. S.; Knoops, H. C. M.; Keuning, W.; van de Sanden, M. C. M.; Kessels, W. M. M., In situ spectroscopic ellipsometry as a versatile tool for studying atomic layer deposition. *Journal of Physics D: Applied Physics* **2009**, *42*.
5. Binnig, G.; Quate, C. F.; Gerber, C., Atomic force microscope. *Physical Review Letters* **1986**, *56*, 930-933.
6. Giessibl, F. J., Advances in atomic force microscopy. *Reviews of Modern Physics*. **2003**, *75*, 949-983.
7. Meyer, E., Atomic force microscopy. *Progress in Surface Science* **1992**, *41*, 3-49.
8. McConney, M. E.; Singamaneni, S.; Tsukruk, V. V., Probing soft matter with the atomic force microscopies: imaging and force spectroscopy. *Polymer Reviews* **2010**, *50*, 235-286.
9. Magonov, S. N.; Reneker, D. H., Characterization of polymer surfaces with atomic force microscopy. *Annual Review of Materials Science* **1997**, *27*, 175-222.
10. de Gennes, P. G.; Brochard-Wyart, F.; Quere, D., *Capillarity and Wetting Phenomena: Drops, Bubbles, Pearls, Waves*. New York, 2003.
11. Berg, J. C., *Wettability* New York, 1993.
12. Fadley, C. S., Angle-resolved x-ray photoelectron-spectroscopy. *Progress in Surface Science* **1984**, *16*, 275-388.
13. Wagner, C. D., Factors affecting quantitative determinations by x-ray photoelectron spectroscopy. *Analytical Chemistry* **1977**, *49*, 1282-1290.
14. Carver, J. C.; Carlson, T. A.; Schweitz, Gk, Use of X-ray photoelectron spectroscopy to study bonding in Cr, Mn, Fe, and Co compounds. *Journal of Chemical Physics* **1972**, *57*, 973.
15. Buttry, D. A.; Ward, M. D., Measurement of interfacial processes at electrode surfaces with the electrochemical quartz crystal microbalance. *Chemical Reviews* **1992**, *92*, 1355-1379.
16. Ferreira, G. N. M.; Da-Silva, A. C.; Tome, B., Acoustic wave biosensors: physical models and biological applications of quartz crystal microbalance. *Trends in Biotechnology* **2009**, *27*, 689-697.

17. Sauerbrey, G., Verwendung Von Schwingquarzen zur wagung dunner schichten und zur mikrowagung. *Zeitschrift Fur Physik* **1959**, *155*, 206-222.
18. Johannsmann, D., Viscoelastic, mechanical, and dielectric measurements on complex samples with the quartz crystal microbalance. *Physical Chemistry Chemical Physics*. **2008**, *10*, 4516-4534.
19. Marx, K. A., Quartz crystal microbalance: a useful tool for studying thin polymer films and complex biomolecular systems at the solution-surface interface. *Biomacromolecules* **2003**, *4*, 1099-1120.

Chapter 3.

Protein Micropatterning on Dewetted PLGA Films

3.1. Introduction

The ability to control protein adsorption on solid substrates is crucial for many applications involving site-specific cell adhesion, such as single cell studies, as the interaction of cells with their environment is mediated by extracellular proteins.¹⁻³ Several techniques have been employed to pattern proteins on a surface, including microcontact printing,⁴ dip-pen nanolithography,⁵ and microfluidic patterning.⁶ Although elegant, these strategies have drawbacks, such as the time and number of steps required for fabrication, and their applicability only to flat surfaces. The Neto group developed an alternative route to create micropatterned surfaces for protein patterning, based on the dewetting of polymer bilayers made of polymer thin films with different protein affinity.⁷⁻⁹ In dewetted films, control over hole size and density is possible by varying annealing the temperature and polymer molecular weight, respectively.¹⁰⁻¹² Although thin polymer films are commonly prepared by spin coating onto flat substrates, they can also be easily deposited on three-dimensional objects by dip-coating or spraying.

The approach developed by the Neto group is based on the use of polymer bilayers consisting in a protein-repellent top layer deposited on top of a protein-adhesive bottom layer. Dewetting of the polymer top layer produces a chemical and topographical surface pattern consisting in exposed holes of the bottom layer (protein-adhesive) surrounded by a matrix of the top layer (protein-repellent).⁷ The different protein affinity of the polymers can be used to pattern proteins by site-selective

adsorption inside the holes of the protein-adhesive bottom layer upon exposure to protein solutions. Protein micropatterning was achieved using poly(methyl methacrylate) (PMMA) as protein-repellent top layer, and additionally cell attachment and growth was proven inside the patterns when poly(vinyl pyrrolidone) (PNVP) films were dewetted and cross-linked on top of polystyrene (PS) bottom layers.^{7, 8} Grafting of protein-repellent poly(ethylene glycol) brushes from custom-synthesized macro-initiator polymer films improved significantly the selective localization of proteins and cells, but required a significant synthetic effort.⁹

A crucial point in the design of polymer coatings for biological applications is the long-term biocompatibility of the materials employed, since many synthetic polymers show cytotoxic effects.¹³ Poly(D,L-lactide-*co*-glycolide) (PLGA) is a well-known biodegradable polymer,¹⁴ widely studied for use in biological applications¹⁵⁻¹⁷ and also approved for use in certain applications by the US Food and Drug Administration, as the products of PLGA degradation are non-cytotoxic and readily eliminated from the human body.¹⁸ In the present work we present for the first time the micropatterning of PLGA film by dewetting for site-specific protein adsorption. Non-specific protein adsorption on PLGA films can be reduced by grafting of poly(ethylene glycol) (PEG) brushes. PEG coatings with high grafting density can be obtained via *grafting-to* strategies, which involve the attachment of prefabricated polymers onto the surface, where the grafting reaction is carried out under low solubility conditions for PEG (close to the cloud point, *CP*). At the cloud point, PEG chains undergo a transition from being well-solvated and occupying a large hydrodynamic volume, to a collapsed state, resulting in closely packed PEG molecules tethered to a surface.¹⁹

In this study, PLGA thin films were patterned by dewetting on top of polystyrene (PS) films (Figure 3.1, step (i)), and the partially dewetted PLGA films were then grafted with poly(ethylene glycol) diglycidyl ether (PEGepoxide) in a simple two-step process (Figure 3.1, steps (ii)-(iii)). This approach combines the protein-repellence of PEG coatings with the numerous benefits of PLGA films: biocompatibility, insolubility in water, processability and the ability to dewet on various substrates. The grafting density of PEG on the partially dewetted PLGA films was tuned by performing the grafting reaction under varying solubility conditions for PEG (Figure 3.1, step (iii)): low solubility grafting, referred as cloud point grafting (*CP*), and high solubility grafting, referred as room temperature grafting (*RT*). The protein

repellence and the biodegradability of the PEG-grafted PLGA films (PEG-g-PLGA) films were investigated, and the partially dewetted PEG-g-PLGA films on PS was employed for protein micropatterning by preferential protein adsorption from solution (Figure 3.1, step (iv)).

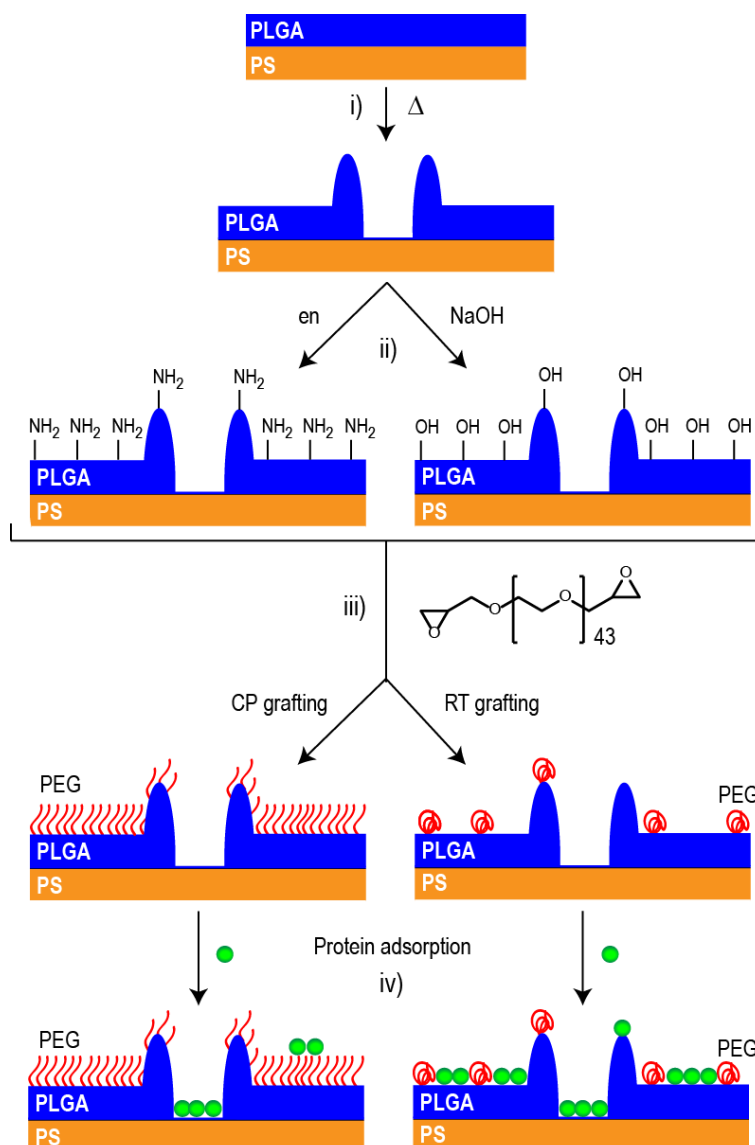


Figure 3.1. Schematic of the patterning and functionalization of PLGA/PS bilayers for biological applications. (i) Dewetting of PLGA films on PS by thermal annealing. (ii) Surface aminolysis (with ethylenediamine, en) and surface hydrolysis (with NaOH) of the PLGA film to create grafting points in the form of NH_2 and OH groups, respectively. (iii) PEG grafting performed on PLGA- NH_2 and PLGA- OH under cloud point conditions (*CP* grafting) and at room temperature (*RT* grafting), resulting in brush layers and mushrooms, respectively. (iv) Exposure to a protein solution results in preferential protein adsorption.

3.2. Materials and Methods

3.2.1. Sample preparation

Polymer bilayers were prepared on prime grade silicon wafers (MMRC Pty. Ltd., Australia), previously cleaned as described in Section 2.1.²⁰ Polystyrene (PS, M_n 96000 g mol⁻¹, \bar{D} 1.04; Polymer Standard Service, Germany) was spin-cast in films on clean silicon wafers from a 20 mg mL⁻¹ toluene (anhydrous, 99.8 %; Sigma-Aldrich) solution (3000 RPM for 1 min). Poly(D,L-lactide-*co*-glycolide) (PLGA, M_n 50000 – 75000 g mol⁻¹; Sigma-Aldrich) was then spin-cast on top of the PS films from a 10 mg mL⁻¹ acetonitrile (> 99.9%, Merck) solution (3000 RPM for 1 min).

The average thickness of the films obtained was 77 ± 2 nm for PS, and 33 ± 2 nm for PLGA, as determined by spectroscopic ellipsometry (Woollam Co. Inc. M-2000), as described in Section 2.2. Both as-prepared films were smooth, with root-mean-square (RMS) roughness lower than 0.3 nm, as measured by atomic force microscopy (AFM, Bruker Multimode VIII) using tapping mode in air on 3×3 μ m scan area. To induce the desired pattern of holes, the PLGA/PS bilayers were dewetted by annealing at 120 °C for 1 min in air on a hot plate with fine temperature control (ATV Technologie GmbH, Germany), and cooled down at room temperature to stop the dewetting. The dewetting process was monitored by optical microscopy (Nikon LV-150). X-ray photoelectron spectroscopy (XPS) analysis on flat films was performed using an AXIS Ultra DLD spectrometer (Kratos Analytical Inc.), as described in Section 2.6.⁹ The contact angle of sessile droplets of Milli-Q water (18.2 M Ω cm at 25 °C) on the polymer films prior to dewetting was measured with a KSV CAM200 contact angle system (KSV Instruments Ltd., Finland), as described in Section 2.4. Differential scanning calorimetry (DSC; TA Instruments, DSC 2920) was used to measure the T_g of PLGA powder, as described in Section 2.5. Mass loss and eventual decomposition of PLGA during annealing were monitored with thermal gravimetric analysis (TGA; TA Instruments, TGA 2950) by heating-up PLGA powder from 25 °C to 200 °C at 10 °C/min.

3.2.2. Aminolysis and hydrolysis of PLGA/PS bilayers

Aminolysis and hydrolysis of both partially dewetted and flat PLGA/PS bilayers were performed following the protocol described by Croll *et al.*²¹ Briefly, the polymer

bilayers were immersed into solutions of aqueous ethylenediamine (en, > 99%, Merck) 0.05 M, or aqueous sodium hydroxide (NaOH, > 97%, Ajax Finechem) 0.05 M, and allowed to react for 5 min with stirring at room temperature.

3.2.3. PEG grafting on PLGA-NH₂ and PLGA-OH films on PS

The grafting of poly(ethylene glycol) diglycidyl ether (PEGepoxide, M_n 2000 g mol⁻¹, \bar{D} 1.10; Sigma-Aldrich) on PLGA-NH₂/PS and PLGA-OH/PS bilayers was performed under different solubility conditions for PEG, in order to vary the final grafting density, as described by Kingshott *et al.*¹⁹ Low solubility grafting (cloud point conditions, *CP*) was performed in solutions of PEGepoxide (5.0 mg mL⁻¹) in 0.1 M phosphate buffer at pH 7 containing 0.8 M Na₂SO₄. The reaction was carried out overnight at 33 °C. High solubility grafting (room temperature conditions, *RT*) was performed in solutions of aqueous PEGepoxide (5.0 mg mL⁻¹) overnight at room temperature ($T = 25$ °C). PLGA-NH₂ and PLGA-OH films were exposed to PEGepoxide immediately after preparation, to ensure minimal loss of surface reactivity from the spontaneous oxidation of surface amine and hydroxyl groups.²²

Grafting density (g) and average interchain distance ($2R$) were calculated from the thickness (h) of the PEG coating measured by ellipsometry. The calculation used is described in the following. From the thickness (h) the volume (V) of the PEG coating per unit area (l^2) was estimated as:

$$V = h \cdot l^2 \quad (3.1)$$

V was used to calculate the mass (m) of the PEG coating:

$$m = V \cdot \rho \quad (3.2)$$

where ρ is the density of PEG. The number of moles (n) and the number of molecules (ν) of grafted PEG are, respectively:

$$n = \frac{m}{MW} \quad (3.3)$$

$$\nu = n \cdot \mathcal{N}_A \quad (3.4)$$

where MW is the molecular weight of PEG and \mathcal{N}_A is the Avogadro constant. The number of molecules (ν) per unit area (l^2) gives the grafting density (g). The area per molecule (A) is the reverse of the grafting density:

$$A = g^{-1} \quad (3.5)$$

Assuming the area per PEG molecule (A) is a circular section on the surface, the average interchain distance ($2R$) is twice the radius of the circle:

$$2R = 2 \left(\frac{A}{\pi} \right)^{1/2} \quad (3.6)$$

3.2.4. Protein adsorption

A quartz crystal microbalance (QCM-D, Q-Sense model E4) was used to investigate the adsorption of bovine serum albumin (BSA, Sigma-Aldrich) on flat unpatterned PEG-*g*-PLGA/PS bilayers at 25 °C. The PEG-*g*-PLGA/PS bilayers on the gold-coated quartz crystal sensors (fundamental resonance frequency 5 MHz) were prepared following the same procedure used for silicon wafers described above. QCM measurements were performed as described in Section 2.7. Each measurement was repeated three times and the results averaged in order to calculate mean value and standard deviation.

Fluorescence microscopy was used to visualize the adsorption of BSA on partially dewetted PEG-*g*-PLGA/PS bilayers. BSA was tagged with isothiocyanate (FITC, Sigma-Aldrich) using the procedure recommended by Invitrogen Molecular Probes. Briefly, 10 mg of protein were dissolved in 1 mL of 0.1 M sodium carbonate buffer. Separately, 5 mg of FITC were dissolved in 0.5 mL of dimethyl sulfoxide (DMSO). The FITC solution was slowly added to the protein solution while stirring at room temperature, and incubated at the same temperature for one hour. The FITC-BSA conjugated was separated from the unreacted FITC using a column packed with Sephadex G-25 gel filtration media and 10 mM phosphate buffer saline (PBS; 140 mM NaCl, 3 mM KCl, pH 7.4) as eluent. The resulting protein solution was estimated to be 2 mg mL⁻¹ in concentration by UV-VIS absorption assay. The FITC-BSA solution was divided into 500 µL aliquots, wrapped in aluminium foil and frozen.

Adsorption of FITC-BSA on partially dewetted PEG-*g*-PLGA/PS bilayers was performed by depositing 100 µL of the protein solution on the patterned surface, and leaving to incubate for 2 hours at room temperature. Samples were thoroughly rinsed with Milli-Q water and gently dried with nitrogen prior to imaging. Imaging of the

surface patterns was carried out in fluorescence mode (λ_{ex} 494 nm, λ_{em} 518 nm, exposure time: 6 s).

3.3. Results

3.3.1. Dewetting of PLGA films

The PLGA powder used to prepare all our films was characterized by thermal gravimetric analysis (TGA) to determine the mass loss and potential decomposition at the annealing conditions used in the dewetting of our coatings. The TGA profile in Figure 3.2a shows a small decrease in mass (about 2%) in the first 30 minutes of the annealing in air. This initial mass loss was due to a small quantity of water retained by PLGA (to be expected given that PLGA is relatively hydrophilic). No signs of degradation of PLGA were detected up to a temperature of 200 °C. Differential scanning calorimetry (DSC) results identified the glass transition temperature (T_g) of PLGA to be at approximately 50 °C (Figure 3.2b).

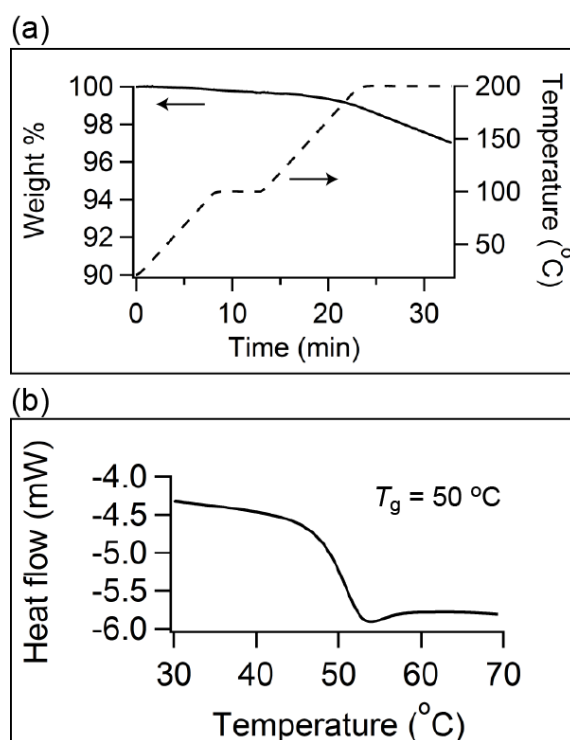


Figure 3.2. Thermogravimetric analysis (TGA) and differential scanning calorimetry (DSC) of PLGA powder. The glass transition temperature (T_g) is indicated.

PLGA thin films on top of PS films were unstable when annealed above the T_g of PLGA and dewetted on the underlying PS layers. The onset of PLGA dewetting upon annealing at 120 °C occurred by random nucleation of holes (Figure 3.3a), which grew in lateral size until coalescence with neighbouring holes (Figure 3.3b), leading to the formation of polymer ribbons (Figure 3.3c) and, eventually, to isolated droplets after prolonged annealing (Figure 3.3d). The dynamics of hole growth in PLGA films before hole coalescence is shown in Figure 3.4. In the early stages of dewetting, the energy is dissipated mainly by slippage of the liquid film on the solid substrate (full slip regime) and the radius of the hole (R) grows with time as $t^{2/3}$. In later stages of dewetting, viscous dissipation within the liquid films dominates the hole growth (no slip regime) and the radius of the hole grows linearly with time.²⁴ This growth profile is the typical behavior expected for the dewetting of a polymer film on top of a non-wettable solid substrate and, therefore, indicates that negligible interpenetration of the two films occurred in the early stages of dewetting. However, the long annealing time required to achieve the formation of isolated PLGA droplets (5 hours) indicated that partial interpenetration of the films occurred at later stages of dewetting, which slowed down the break-up of the PLGA cylinders into droplets.^{25, 26} Partial interpenetration was confirmed by imaging carried out using AFM, as detailed in Figure 3.3e-f.

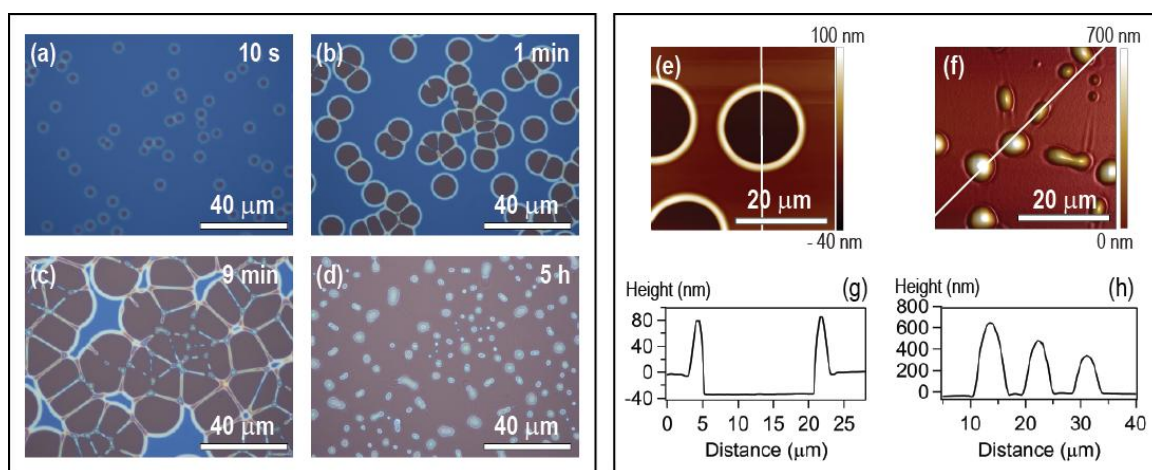


Figure 3.3. (a-d) Optical micrographs showing the typical real-time dewetting of PLGA films on PS films upon annealing at 120 °C. (e-h) AFM topography images of (e) partially dewetted PLGA film (33 nm) on a PS film (77 nm) after 1 min at 120 °C and (f) fully dewetted PLGA films on PS films after 5 hours at 120 °C. (g-h) Line-cross sections from the AFM topography images of the PS hole in part (e) and the PLGA droplets in part (f), respectively.

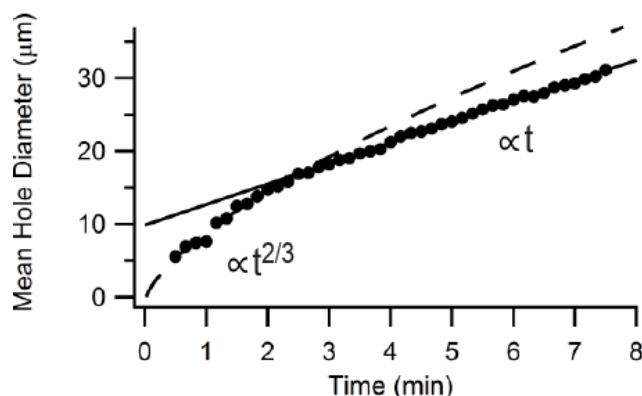


Figure 3.4. Typical dynamic of hole growth in PLGA/PS bilayers upon annealing at 120 °C. Dashed line: fitting of the mean hole diameter with a $t^{2/3}$ scaling law. Solid line: fitting of the mean hole diameter with a t scaling law.

The AFM micrograph of a partially dewetted PLGA/PS bilayer in Figure 3.3e shows PS holes surrounded by flat PLGA background. As expected in dewetting of polymer thin films, the retraction of PLGA during dewetting caused the accumulation of the dewetted polymer into rims (83 ± 10 nm high) surrounding the PS holes (31 ± 5 nm deep) (Figure 3.3g). Upon complete dewetting, the isolated droplets of PLGA on the PS bottom layer were often asymmetric in shape, and polydisperse in diameter (approx. 2 μ m to 8 μ m, Figure 3.3f) and height (approx. 100 nm to 700 nm, Figure 3.3h). The retraction of the PLGA ribbons into droplets left thin and shallow tracks on the surface of the underlying PS film (Figure 3.3f). The appearance of these tracks in the PS film, the polydispersity of the PLGA droplets and their delayed break-up can probably be explained by the partial interpenetration of PLGA and PS films after several hours of annealing at 120 °C, which is above the T_g of both PLGA and PS.

3.3.2. PLGA aminolysis and hydrolysis

PLGA films were treated with ethylenediamine (en) and NaOH to create reactive functional groups (NH_2 and OH , respectively) on the surface. Aminolysis and hydrolysis of PLGA films caused a decrease of the film thickness (-0.7 ± 0.3 nm after aminolysis, and -10.1 ± 0.3 nm after hydrolysis, as per ellipsometry measurement), due to the fragmentation of PLGA chains on the films' surface upon treatment with ethylenediamine and NaOH, respectively (Figure 3.5).

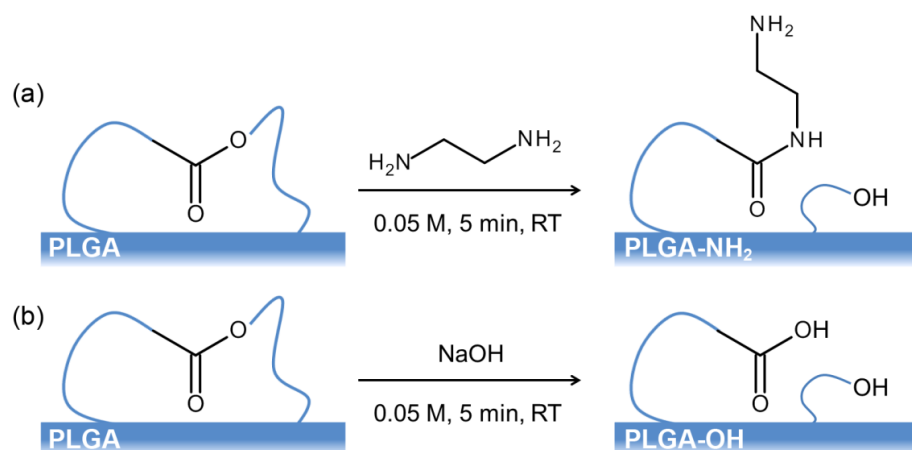


Figure 3.5. Schematic of (a) surface aminolysis of PLGA films with ethylenediamine, and (b) surface hydrolysis of PLGA films with sodium hydroxide.

These reactions led to water-soluble short-chain fragments that were dissolved away when rinsing, as previously observed.^{27, 28} The thickness decrease in PLGA-OH films (-10.1 ± 0.3 nm) was more than 10 times higher than that observed in PLGA-NH₂ films (-0.7 ± 0.3 nm), due to the higher mobility of OH⁻ ions in comparison to ethylenediamine molecules, which allowed OH⁻ to penetrate deeper in the PLGA film, increasing the depth of chain fragmentation. AFM imaging showed that the RMS roughness of the PLGA films was largely unchanged after aminolysis and hydrolysis (PLGA, $RMS = 0.29 \pm 0.02$ nm; PLGA-NH₂, $RMS = 0.25 \pm 0.03$ nm; PLGA-OH, $RMS = 0.34 \pm 0.05$ nm) (Figure 3.6). The static contact angle of water on PLGA was $72 \pm 2^\circ$ and it did not change significantly after *surface* aminolysis (the contact angle on PLGA-NH₂ was $72 \pm 2^\circ$), or hydrolysis, (on PLGA-OH it was $66 \pm 4^\circ$) (Table 3.1).

Table 3.1. Water contact angle and thickness of PLGA films before and after *surface* aminolysis and hydrolysis, respectively.

	Contact Angle (°)			Thickness (nm)
	Static	Advancing	Receding	
PLGA	72 ± 1	80 ± 1	51 ± 3	33.4 ± 0.1
PLGA-NH₂	72 ± 1	76 ± 1	44 ± 3	32.7 ± 0.2
PLGA-OH	66 ± 1	79 ± 1	45 ± 1	23.3 ± 0.2

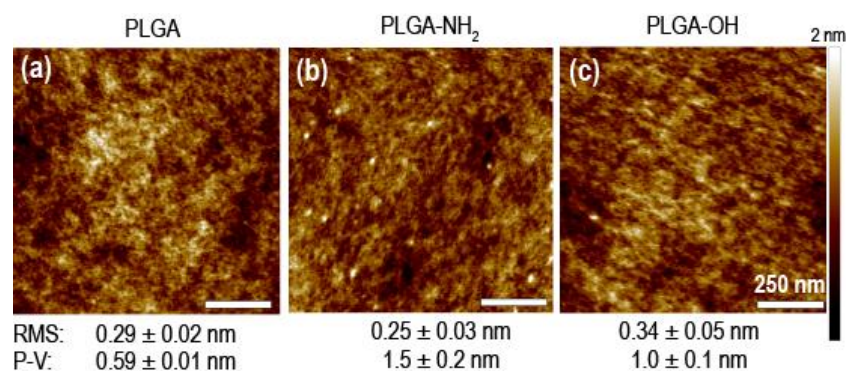


Figure 3.6. AFM topography images of (a) as spin-coated PLGA films, (b) surface-aminolyzed PLGA films (PLGA-NH₂), and (c) surface-hydrolyzed PLGA films (PLGA-OH). The *RMS* roughness values and the peak-to-valley (*P-V*) values are indicated in the images.

XPS analysis of PLGA-NH₂ films showed that, after aminolysis in aqueous ethylenediamine (0.05 M), the nitrogen content on the surface was 0.10 %, whereas no nitrogen was detected on the untreated PLGA films (Figure 3.7a). Except for the nitrogen content measured on the PLGA-NH₂ surfaces, aminolysis and hydrolysis induced very little change in the atomic composition of the surface with respect to untreated PLGA films (Table 3.2). In the case of hydrolysis, it has been reported in literature that for every 1 % of ester bonds hydrolyzed, the amount of oxygen on the surface should increase by only 0.1 %, which made this level of modification undetectable by XPS. Also, no remarkable changes in the C 1s spectrum were observed after either aminolysis or hydrolysis of PLGA films (Figure 3.7b).

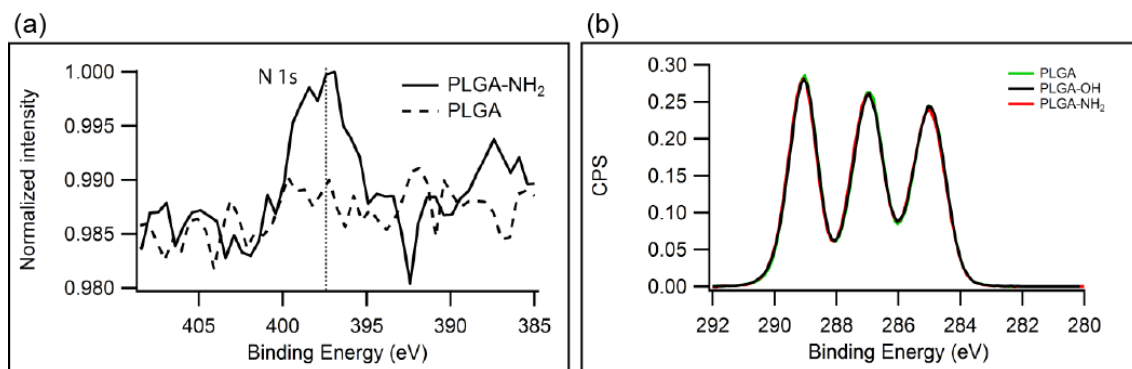


Figure 3.7. (a) N 1s region of the XPS spectra of PLGA-NH₂ (solid line) and PLGA (dashed line). (b) C 1s region of the XPS spectrum of PLGA, PLGA-OH and PLGA-NH₂ films.

Table 3.2. Atomic composition and O/C ratio of the employed surfaces as determined by XPS.

	Element (%)						O/C
	O	C	N	F	Cl	Si	
PLGA/PS	37.1	62.9	<0.01	<0.1	<0.1	<0.1	0.59 ± 0.01
PLGA-NH₂/PS	37.1	62.9	0.1	<0.1	<0.1	<0.1	0.59 ± 0.01
PLGA-OH/PS	37.0	63.0	-	<0.1	<0.1	<0.1	0.59 ± 0.01
PEG_{CP}-g-PLGA-NH₂/PS	35.4	63.9	-	0.1	0.1	0.4	0.55 ± 0.01
PEG_{RT}-g-PLGA-NH₂/PS	36.3	63.4	-	<0.1	<0.1	0.3	0.57 ± 0.01
PEG_{CP}-g-PLGA-OH/PS	35.5	63.9	-	<0.1	0.1	0.4	0.55 ± 0.01
PEG_{RT}-g-PLGA-OH/PS	36.7	62.9	-	<0.1	<0.1	0.4	0.58 ± 0.01

PS films exhibited good stability against aminolysis and hydrolysis with ethylenediamine and NaOH, respectively: thickness and contact angle of the PS films were identical before and after either aminolysis or hydrolysis (Table 3.3) and only minor changes in the film topography of the PS films were observed after the treatment (Figure 3.8).

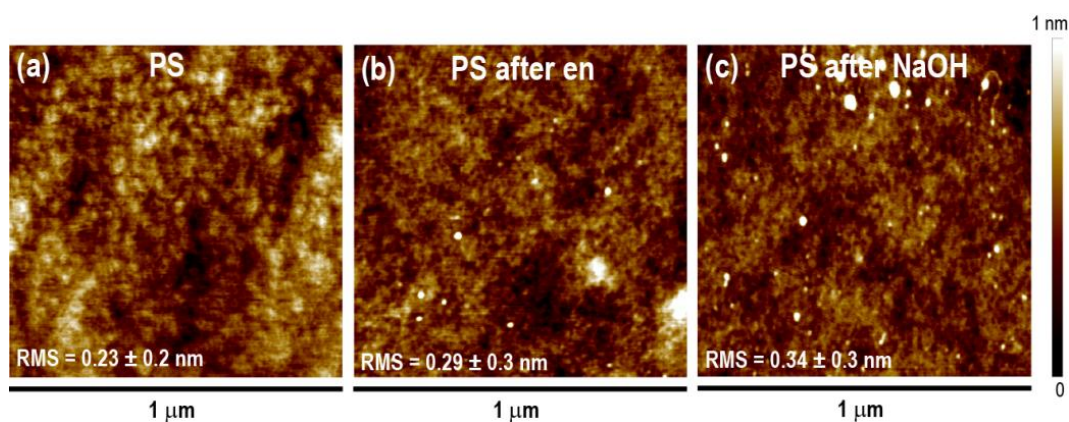
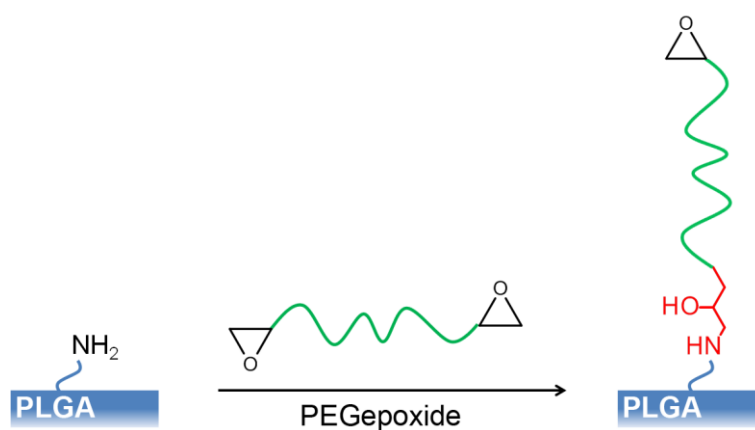
**Figure 3.8.** AFM topography images of (a) PS films, (b) PS films after aminolysis with ethylenediamine – en – and (c) PS films after hydrolysis with NaOH. *RMS* values are indicated.

Table 3.3. Water contact angle and thickness of PS films before and after *surface* aminolysis and hydrolysis, respectively.

	Contact Angle (°)			Thickness (nm)
	Static	Advancing	Receding	
PS	94 ± 1	96 ± 1	95 ± 1	76.3 ± 0.3
PS after aminolysis	93 ± 1	101 ± 1	75 ± 6	76.4 ± 0.3
PS after hydrolysis	95 ± 1	101 ± 5	76 ± 2	76.4 ± 0.3

3.3.3. PEG grafting

The covalent immobilization of PEGepoxide onto PLGA-NH₂ and PLGA-OH surfaces was performed by exploiting the epoxide-amine and the epoxide-hydroxide reactivity, respectively (Figure 3.9).²⁹ PEG grafting was performed under conditions of varying PEGepoxide solubility, achieved by carrying out the grafting reaction at different temperatures and in presence of varying amount of salt, as described by Kingshott *et al.*¹⁹

**Figure 3.9.** Schematic of the mechanism of the grafting of PEGepoxide to PLGA-NH₂ films. A similar reaction mechanism can be drawn for PLGA-OH films by replacing NH₂ groups with OH groups.

Low solubility grafting (cloud point conditions, *CP*) was performed in phosphate buffer at 33 °C in presence of salt (Na₂SO₄ 0.8 M) and high solubility grafting (room temperature conditions, *RT*) was performed in water at room temperature

($T = 25\text{ }^{\circ}\text{C}$). Thickness and packing parameter of the PEG coatings are presented in Table 3.4. CP grafting led to a thicker and denser PEG coating than RT grafting on both PLGA-NH₂ and PLGA-OH: the thickness of the PEG coating was $2.4 \pm 0.8\text{ nm}$ and $4.8 \pm 1.3\text{ nm}$ after CP grafting on PLGA-NH₂ and on PLGA-OH, respectively, and $0.4 \pm 0.3\text{ nm}$ and $0.5 \pm 0.2\text{ nm}$ after RT grafting on PLGA-NH₂ and PLGA-OH, respectively. The loss of the hydration shell surrounding the PEG chains and the consequent association of PEG molecules occurring under CP conditions caused the reduction of the mean interchain distance ($2R$) between the PEG molecules grafted on the surface. The mean interchain distance after CP grafting on PLGA-NH₂ ($2R = 1.21\text{ nm}$) and PLGA-OH ($2R = 0.85\text{ nm}$) were smaller than the Flory diameter ($2R_F$) of PEG ($2R_F = 2.58\text{ nm}$ for PEG with $M_w = 2000\text{ g mol}^{-1}$ in H₂O, from Upadhyayula *et al.*³⁰), suggesting the formation of densely packed PEG coatings.³¹ Conversely, after RT grafting, the $2R$ value was larger than $2R_F$ for both PEG-grafted PLGA-NH₂ ($2R = 3.0\text{ nm}$) and PEG-grafted PLGA-OH ($2R = 2.6\text{ nm}$), indicating the formation of a low-density PEG coating, most likely consisting of isolated polymer coils tethered to the surface (‘mushroom’ conformation).

Table 3.4. Thickness (h), grafting density (g) and interchain distance ($2R$) in the PEG coating after CP and RT grafting on PLGA NH₂ and PLGA-OH. The Flory radius (R_F) refers to PEG with $M_n = 2000\text{ g mol}^{-1}$ in H₂O (from Upadhyayula *et al.*³⁰). Grafting density and interchain distance of PEG molecules were calculated from the film thickness, as described in Section 3.2.3.

	Grafting on PLGA-NH ₂		Grafting on PLGA-OH	
	CP	RT	CP	RT
PEG thickness, h (nm)	2.4 ± 0.8	0.4 ± 0.3	4.8 ± 1.3	0.5 ± 0.2
Grafting density, g (nm ⁻¹)	0.9	0.1	1.7	0.2
Interchain distance, $2R$ (nm)	1.2	3.0	0.9	2.6
$2R$ vs $2R_F$ ($2R_F = 2.58\text{ nm}$)	$2R < 2R_F$	$2R > 2R_F$	$2R < 2R_F$	$2R > 2R_F$
PEG conformation	High-density	Low-density	High-density	Low-density

CP grafting of PEGepoxide on PLGA-OH films led to a thicker PEG coating (4.8 ± 1.3 nm) than on PLGA-NH₂ (2.4 ± 0.8 nm). As illustrated in Figure 3.10, we believe that the PEGepoxide molecules used in our study, which have one epoxide group at each end of the molecule, reacted with surface amine groups to create loops on the surface of PLGA-NH₂, which resulted in a decrease in the average thickness of the PEG coating in PEG-g-PLGA-NH₂ films. This reactivity also has consequences for the protein repellence of the two surfaces, as discussed in Section 3.4.4.

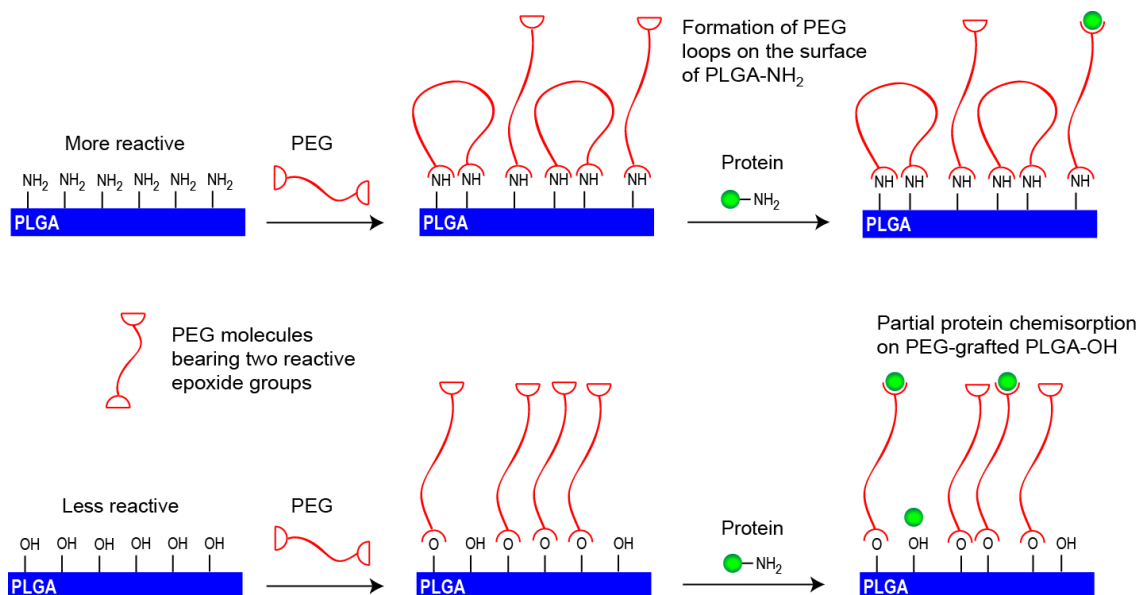


Figure 3.10. Schematic representation of the proposed mechanism for PEG grafting on PLGA-NH₂ and PLGA-OH films and consequences on protein adsorption.

XPS analysis of PEG-g-PLGA films showed a decrease in the oxygen content of the surface, and hence in the O/C ratio, after CP grafting on both PLGA-NH₂ and PLGA-OH films ($O/C_{CP} = 0.55 \pm 0.01$) in comparison to the O/C ratio of aminolyzed, hydrolyzed and untreated PLGA films ($O/C = 0.59 \pm 0.01$) (Table 3.2), which indicated the successful reaction of PEG molecules ($O/C_{THEORETICAL} = 0.50$) on the PLGA surface ($O/C_{THEORETICAL} = 0.70$). Although a decrease in the O/C ratio was observed also after RT grafting on PLGA-NH₂ and PLGA-OH films ($O/C_{RT} = 0.57 \pm 0.01$), the magnitude of the decrease was smaller than that observed after CP grafting, which is consistent

with the formation a high-density PEG coating under CP grafting and a low-density PEG coating under RT grafting.

The C 1s region of the XPS spectrum of PLGA, aminolyzed/hydrolyzed PLGA and PEG-grafted PLGA was composed of three components (Figure 3.11): C-C carbons (285.0 eV), C-O carbons (286.9 eV) and O-C=O carbons (289 eV). The C 1s spectrum of PEGepoxide was composed of a main signal at 286.5 eV (C-O carbons) and a small shoulder at 285 eV (C-C carbons). After PEG grafting on PLGA-NH₂ and PLGA-OH films, we observed a decrease in the ratio of peak intensity for the component at 289 eV (PLGA) and the component at 286.9 eV (PLGA + PEG), which indicated the presence of PEG on the film surface after the grafting reaction (Figure 3.11). The change in shape of the C 1s spectra was more marked for PEG_{CP}-g-PLGA films than for PEG_{RT}-g-PLGA, due to the more effective surface modification under CP conditions.

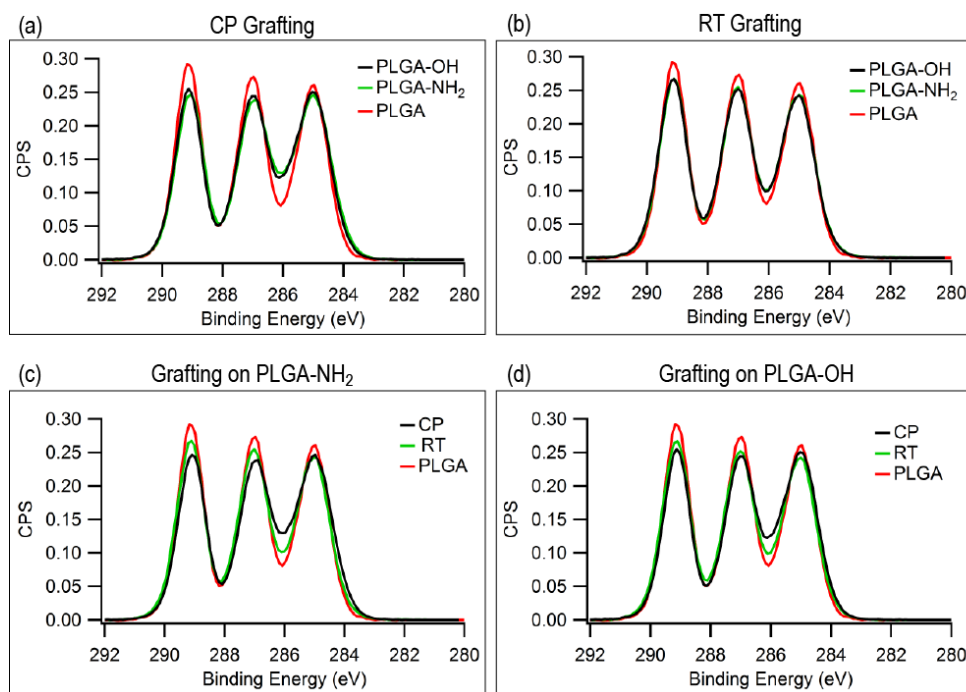


Figure 3.11. (a-b) C 1s region of the XPS spectrum of PLGA-NH₂ and PLGA-OH after (a) CP grafting and (b) RT grafting. (c-d) C 1s region of the XPS spectrum of (c) PLGA-NH₂ and (d) PLGA-OH after CP and RT grafting. The C 1s region of untreated PLGA is also showed in as a reference in each plot.

The topography of PLGA films after PEG grafting was investigated by AFM. Although no significant changes in the film topography were observed, both *RMS* and peak-to-valley (*P-V*) roughness average values slightly increased after PEG grafting (Figure 3.12).

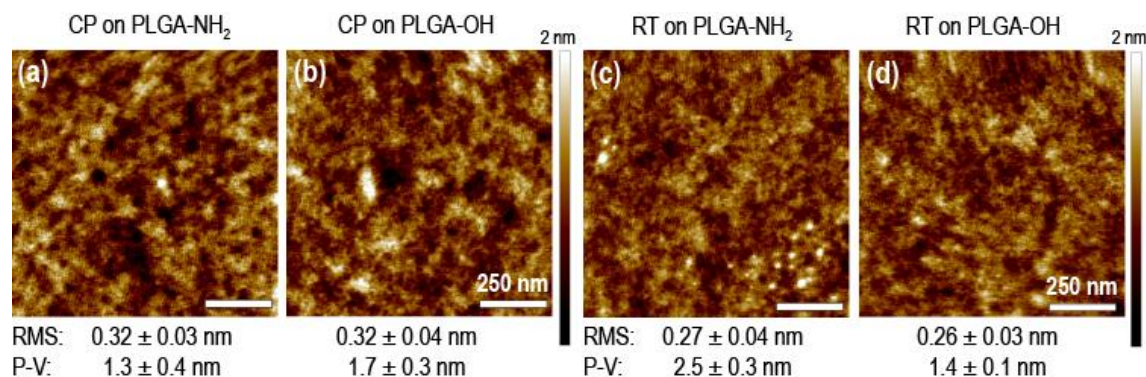


Figure 3.12. AFM topography images of (a) PLGA-NH₂ films after CP grafting, (b) PLGA-OH films after CP grafting, (c) PLGA-NH₂ films after RT grafting, (d) PLGA-OH films after RT grafting. The *RMS* roughness values and the peak-to-valley (*P-V*) values are indicated in the images.

3.3.4. Protein adsorption and preferential protein immobilization

The ability of PEG-*g*-PLGA films to reduce the absorption of bovine serum albumin (BSA) adsorption was assessed by QCM (Figure 3.13). The adsorbed amount on PEG coatings obtained by CP grafting on PLGA-NH₂ was almost one order of magnitude lower ($26 \pm 2 \text{ ng cm}^{-2}$) than that on PEG coatings obtained using RT grafting ($249 \pm 20 \text{ ng cm}^{-2}$). This difference was due to the higher grafting density of PEG molecules achieved under CP grafting conditions, which resulted in significantly lower protein adsorption onto the PEG coating. Similarly, the protein adsorption onto PEG coatings on PLGA-OH films was much lower when the PEG grafting was carried out under CP conditions compared to RT conditions (adsorbed mass: $289 \pm 20 \text{ ng cm}^{-2}$ after CP grafting, and $451 \pm 32 \text{ ng cm}^{-2}$ after RT grafting). Less protein was adsorbed onto PEG-*g*-PLGA films than on both untreated PLGA films ($509 \pm 36 \text{ ng cm}^{-2}$) and PS films ($487 \pm 34 \text{ ng cm}^{-2}$), which showed a similar level of protein adsorption. The excellent performance in terms of low protein adsorption achieved by PLGA-NH₂ films grafted with PEG under CP conditions was similar to that reported in literature for PEG brushes or other antifouling coatings ($10 - 30 \text{ ng cm}^{-2}$).^{32, 33}

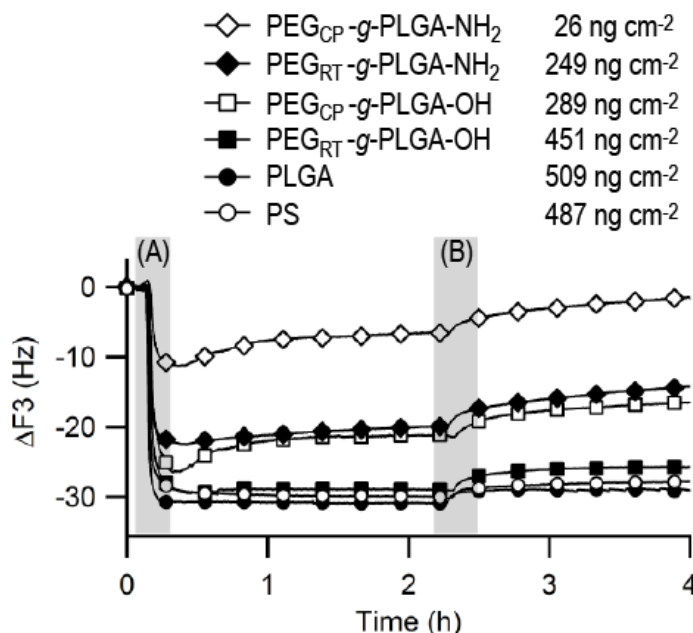


Figure 3.13. Typical frequency shift of a representative resonance frequency (3rd harmonic, F3) during the QCM monitoring of the adsorption of BSA on the employed surface. (A) Injection of the BSA solution in PBS (2 mg mL⁻¹); (B) rinsing with PBS. The mass of the BSA adsorbed on each surface after rinsing is indicated in the legend.

The low protein adsorption properties of PEG-*g*-PLGA films were employed to produce protein micropatterns by preferential immobilization of proteins on partially dewetted PEG-*g*-PLGA/PS bilayers. In Figure 3.14 are presented the fluorescence micrographs obtained for partially dewetted PLGA films (PLGA-NH₂ and PLGA-OH) on PS before and after PEG grafting (under both CP and RT conditions), incubated with FITC-tagged BSA (green fluorescence). The fluorescence micrographs show preferential protein adsorption inside the PS holes rather than on PEG_{CP}-*g*-PLGA-NH₂ and PEG_{CP}-*g*-PLGA-OH (Figure 3.14a-b). RT grafting on both PLGA-NH₂ and PLGA-OH produced a PEG coating with higher protein adsorption and no preferential protein immobilization was achieved (Figure 3.14c-d). The cross-sectional profiles of fluorescence intensity across the samples after PEG grafting and FITC-BSA incubation are shown in Figure 3.15. Both PLGA-NH₂ and PLGA-OH show maximal fluorescence contrast after CP grafting, indicating that these layers are protein repellent. The fluorescence contrast after RT grafting is instead intermediate between that of CP grafting and that of untreated PLGA, where PS holes and PLGA background show nearly the same fluorescence intensity (Figure 3.15a-b). PLGA-NH₂ and PLGA-OH

show the same fluorescence intensity contrast after PEG grafting under CP conditions (Figure 3.15c), indicating similar performances of aminolysis and hydrolysis in terms of surface activation and reactivity with PEG-epoxide.

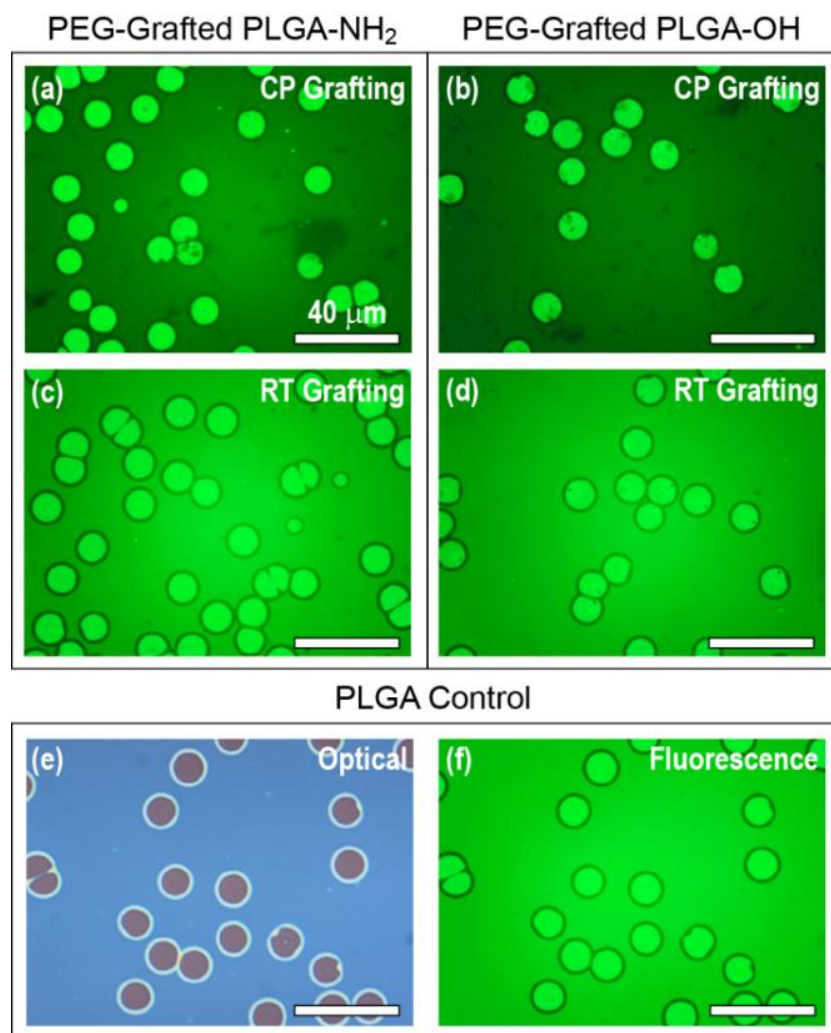


Figure 3.14. Fluorescence micrographs of partially dewetted PLGA/PS bilayers after aminolysis/hydrolysis, PEG grafting and FITC-BSA adsorption. (a) PLGA-NH₂ after CP grafting, (b) PLGA-OH after CP grafting, (c) PLGA- NH₂ after RT grafting, (d) PLGA-OH after RT grafting. (e) Optical and (f) fluorescence micrograph of untreated PLGA after FITC-BSA adsorption. Fluorescence exposure time: 6 s.

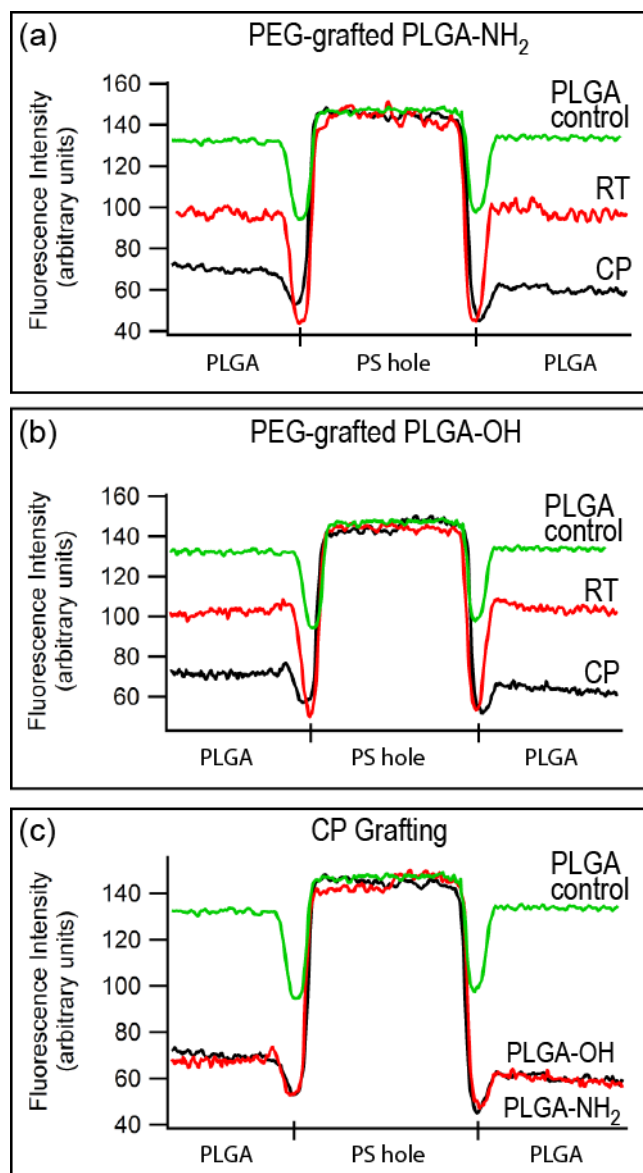


Figure 3.15. Cross-sectional fluorescence intensity profiles across partially dewetted PEG-g-PLGA film on PS after incubation with FITC-BSA. (a) PEG-grafted PLGA-NH₂ under CP and RT conditions, (b) PEG-grafted PLGA-OH under CP and RT conditions, (c) PEG-grafted PLGA-NH₂ and PLGA-OH under CP conditions.

Although analysis of QCM data showed that less protein were adsorbed onto PEG_{CP}-g-PLGA-NH₂ surfaces than on PEG_{CP}-g-PLGA-OH (Figure 3.13), the fluorescence assay with FITC-BSA led to similar fluorescence intensity contrast for partially dewetted PEG_{CP}-g-PLGA-NH₂/PS and PEG_{CP}-g-PLGA-OH/PS bilayers (Figures 3.14 and 3.15). Although the reason of the discrepancy between QCM and

fluorescence is not fully clear at the present, we believe it is related to the dependence of the fluorescence yield of the FITC tag on the local pH at the surface.³⁴

3.3.5. Degradation of PLGA films and PEG-g-PLGA films

The degradation of PEG-g-PLGA/PS bilayers after immersion in PBS was monitored by both optical microscopy and spectroscopic ellipsometry and compared to the degradation of PLGA/PS bilayers in PBS (Figure 3.16). Partially dewetted and flat PEG-g-PLGA films exhibited good resistance to degradation: optical micrographs of partially dewetted PEG-g-PLGA/PS bilayers showed no significant changes in the topography of both the PS holes and the PEG-g-PLGA film after immersion in PBS up to 25 days (Figure 3.16a-b), with no remarkable change in the morphology of the rims of the PS holes and no appreciable signs of PEG-g-PLGA erosion within the timeframe of the experiment. Monitoring of the degradation of flat PEG-g-PLGA/PS bilayers by spectroscopic ellipsometry showed no significant change in the thickness of the PEG-g-PLGA top layer (Figure 3.16c) and indicated no detectable erosion of the PEG-g-PLGA film after 25 days in PBS.

The degradation of untreated PLGA/PS bilayers on the other hand is shown in Figure 3.16d-f. Coalescence of multiple holes in partially dewetted PLGA/PS bilayers was observed after 3 days of immersion in PBS (Figure 3.16d), which became extensive across the polymer surface after 16 days (Figure 3.16e). We believe that the multi-coalesced holes observed throughout the degradation experiments on PLGA/PS bilayers in PBS were the consequence of solvent-induced dewetting of PLGA films, triggered by the fragmentation of PLGA into low-molecular weight chains. Additional investigation showed that PLGA films dewet in water upon annealing above 40 °C, whereas the onset of PLGA dewetting in air was observed at around 100 °C. The low-temperature dewetting of PLGA/PS bilayers in water provides supporting evidence of the in-water dewetting of PLGA occurring at room temperature during the degradation experiments, due to the lowering of the T_g of the fragmented polymer. The degradation of flat PLGA films in PBS was followed by monitoring the thickness change in the PLGA films (Figure 3.16f). PLGA films in PBS were stable with respect to the film thickness for up to 7 days, with a rapid decrease of the film thickness for longer immersion time, as similarly observed in literature.¹⁴ The comparison of the degradation performances of

PEG-*g*-PLGA and PLGA films in PBS showed significant enhancement of the resistance against degradation of PLGA films after PEG grafting.

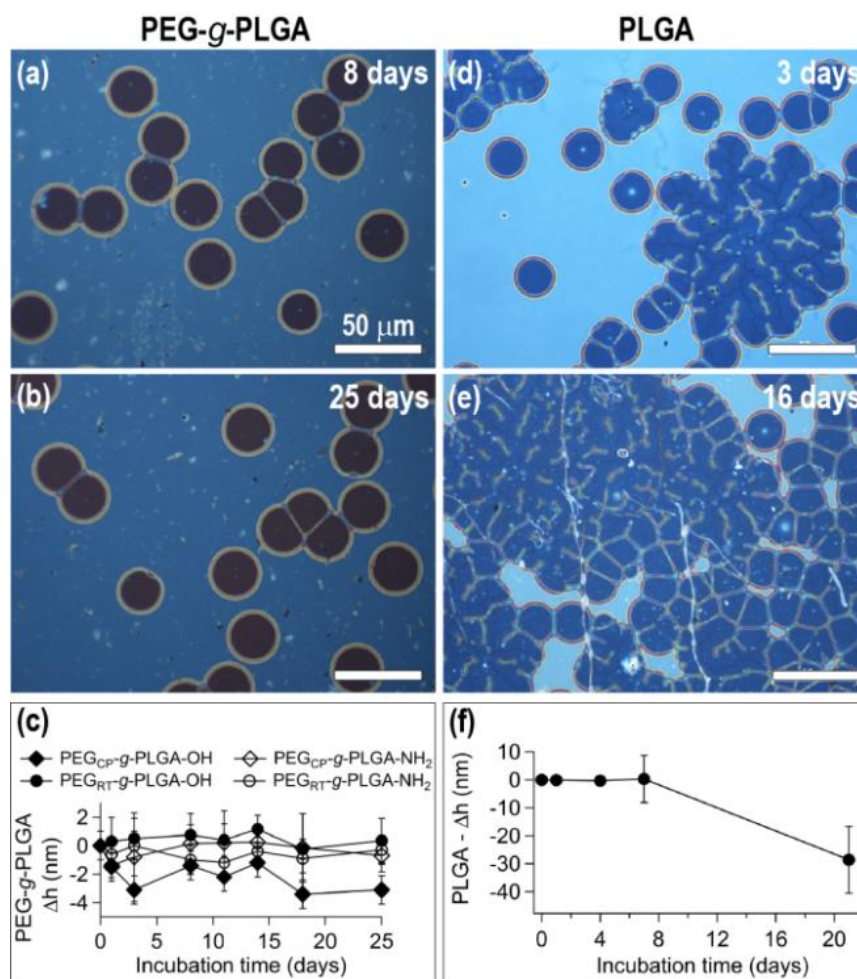


Figure 3.16. (a-b) Optical micrographs of partially dewetted PEG-*g*-PLGA/PS bilayers after incubation in PBS at room temperature for (a) 8 days and (b) 25 days. (d-e) Optical micrographs of partially dewetted PLGA/PS bilayers after immersion in PBS at room temperature for (d) 3 days and (e) 16 days. Thickness change in (c) PEG-*g*-PLGA films and (f) PLGA films after immersion in PBS for various intervals.

3.4. Discussion

In this Chapter we investigated the grafting of PEG chains onto partially dewetted PLGA thin films, and demonstrated the use of these new functional micropatterned films as platforms to selectively adsorb and produce protein micropatterns. PLGA was chosen as a dewettable polymer as it is biocompatible, FDA-approved, and can be spin-

coated and dewetted on hydrophobic substrates, such as PS. In addition, the biodegradability of plain PLGA in water solutions offers the opportunity to test the ability of grafted thin layer to create a barrier to water penetration in the underlying film.

Different substrates could replace the PS bottom film in the bilayer, such as culture tissue treated polystyrene, as long as PLGA formed unstable films upon solvent or thermal annealing. Surface patterning by dewetting of thin polymer films is intrinsically an up-scalable method, which could be applied to objects of any shape and size, since the only requirement for patterning is a uniform coating on the object. This can be achieved, for example, by dip-coating and either thermal or solvent annealing of the polymer film. The size of the dewetting patterns, consisting of randomly nucleated holes with narrow size distribution, can be controlled simply by tuning the annealing conditions (temperature and time). By cooling the polymer films down to room temperature, dewetting can be stopped at any stage of hole growth: the longer the annealing time, the larger the holes.^{10, 11, 20, 24} In terms of the dynamics of hole growth, the higher the annealing temperature, the lower the polymer viscosity and the faster the hole growth.

Our group has shown that dewetting patterns with lateral order can be produced by pre-stamping the substrate via microcontact printing techniques; ordered patterns might be useful for automated read-out and quantification in biological applications, e.g. single-cell studies.³⁵ In our investigation we highlighted a number of important physico-chemical mechanisms, as detailed below.

3.4.1. Layer inversion

As the PLGA/PS bilayer system contains a high surface tension polymer (PLGA) on top of a lower surface tension polymer (PS), we anticipated that there would be a degree of layer interpenetration and inversion during dewetting. Layer interpenetration occurs when the surface tension of the bottom layer is lower than the surface tension of the top layer:^{25, 26} the polymer with lower surface tension, here PS, tends to migrate to the polymer-air interface, partially displacing the top polymer with higher surface tension, in this case PLGA. Layer inversion is related to the mobility of the polymer layers in their melt states: the lower the viscosity of the polymer, the greater the likelihood of layer inversion. In our experiments, PS flows relatively slowly at the annealing

temperature of 120 °C, and so layer interpenetration became noticeable only after long annealing times. The extent of layer inversion observed overall was limited, as the top film appeared to be very well coated with the grafted PEG brush, which excludes the presence of large PS patches anywhere but inside the dewetted holes.

3.4.2. Surface functionalization of PLGA

Surface aminolysis and hydrolysis enabled the formation of reactive groups (-NH_2 and -OH , respectively) on the surface of PLGA films, which were then employed to graft PEG molecules by the epoxide ring-opening reaction. Both aminolysis and hydrolysis consist in the cleavage of the ester bonds of PLGA by reaction of the carbonyl groups on the polymer backbone with a nucleophile (en and NaOH, respectively). The surface of aminolyzed and hydrolyzed PLGA films contains amides bearing primary amines and carboxylic acids, respectively, plus primary alcohols on both surfaces.²¹ The amine groups on the surface were found to be more efficient than the hydroxyl groups for the creation of dense PEG grafted brushes. The possible explanation lies in the higher reactivity of amine groups towards epoxide ring-opening reactions, due principally to the higher nucleophilicity of amines with respect to alcohols.³⁶ Aminolysis and hydrolysis reactions are versatile approaches for surface functionalization of polymer films, as they are not specific to PLGA and could be used to modify the surface of other polymers containing ester bonds in the backbone, such as polycaprolactone, polylactic acid and polyethylene terephthalate.²⁸ In addition, the reactive groups created on the surface of the film (NH_2 and OH) could be used to functionalize the film with different grafted polymer layers, by using a range of other chemical reactions, such as reductive amination of aldehyde-terminated chains, or amination of chains with terminal *N*-hydroxysuccinimide (NHS) esters.

3.4.3. Grafting of PEG to PLGA

In this Chapter, PEG grafting was performed via covalent immobilization of prefabricated PEG molecules (*grafting to* strategy) on the surface of aminolyzed and hydrolyzed PLGA films. The main benefits of employing a *grafting to* strategy are the limited synthetic effort, the ease of the grafting protocol and the use of commercially-available chemicals. In addition, in the development of biocompatible coatings for biological applications, *grafting to* strategies may be preferable to *grafting from*

strategies employing atom-transfer radical polymerization (ATRP),³⁷ due to the cytotoxicity of the copper catalyst used in these cases.³⁸

Thick and densely packed PEG coatings could be achieved only under the low solubility conditions used in the cloud point grafting approach. This observation confirmed the finding of Kingshott *et al.*¹⁹ that the reduction of the intermolecular repulsion between PEG chains, induced by the loss of the hydration shell of PEG molecules under cloud point conditions (high temperature and high ionic strength), leads to dense packing of chains on the surface.³⁹

The higher nucleophilicity of amine groups with respect to hydroxyl groups and the use of bifunctional PEG molecules likely favored the formation of PEG loops on PLGA-NH₂ films by reaction of the amine groups on the surface with the unreacted epoxide group of tethered PEG molecules, which is believed to have consequences for the protein adsorption, as discussed below.

3.4.4. Protein adsorption on grafted PEG layers

The key properties that determine the protein repellence of PEG coatings are the grafting density and the conformation of PEG molecules at the interface.^{40, 41} The grafting density should be high enough to provide an interfacial barrier preventing protein molecules from interacting with the underlying substrate,⁴² but not so high as to lead to the loss of the helical conformation of PEG chains.⁴³ The protein-adsorptive properties of PLGA films were markedly reduced after PEG grafting, with the strongest antifouling properties being achieved on PEG-g-PLGA coatings obtained using CP grafting (high grafting density coatings), as tested by QCM and fluorescence microscopy. Protein adsorption experiments by QCM showed that the low protein adsorption observed on PEG coatings grafted on PLGA films under CP conditions was comparable to that reported in literature for high density PEG brushes and other antifouling coatings.^{31, 40, 44} The strong contrast in protein affinity of the polymer layers was used to produce protein micropatterns on partially dewetted bilayers, as demonstrated by fluorescence micrographs revealing the preferential adsorption of fluorescent proteins inside the PS domains. The best performance in terms of selectivity of protein adsorption was achieved employing CP-grafted PLGA films: the low protein adsorption onto PEG-g-PLGA films resulted in preferential protein adsorption only inside the PS holes. Interestingly, the 2.4 nm thick PEG coating on PLGA-NH₂ films

obtained under CP conditions were more protein-repellent than the 4.8 nm thick PEG coating on PLGA-OH films. We believe that this is related to the occasional chemisorption of BSA via reaction of the amine groups of the protein with the unreacted epoxide groups exposed on the surface of the PEG coatings (Figure 3.10),⁴⁵ which are likely to be more abundant on the surface of PLGA-OH due to the less favourable PEG looping.

3.4.5. Degradation resistance

The degradation properties of PLGA films were significantly modified by PEG grafting. PEG coatings enhanced the resistance of PLGA films against degradation by creating a thin passivation layer, which protected the underlying PLGA films from hydrolysis. Similarly, it is known that alkanethiol self-assembled monolayers on gold or copper are an effective anti-corrosion shell for the metallic substrate.^{46, 47} PEG-induced passivation of PLGA films was observed after both CP and RT grafting, indicating that the thickness and the grafting density of the PEG coating achieved in both instances was sufficiently high to provide degradation resistance.

3.5. Summary

We reported for the first time the dewetting of PLGA thin films for surface micropatterning. PLGA thin films on PS were annealed above the T_g to produce a surface pattern consisting in randomly nucleated PS holes surrounded by a PLGA matrix. The micropatterned PLGA films were functionalized by covalent immobilization of PEG molecules via a two-step grafting route, consisting in PLGA activation by aminolysis/hydrolysis followed by PEG grafting. The advantages of this functionalization protocol proposed in the present work are the flexibility (different types of reaction can be used to graft PEG molecules on aminolyzed/hydrolyzed surfaces), the environment-friendliness (all reactions were performed in water) and the limited synthetic effort (all reaction employed commercially-available chemicals). The protein adsorption onto the novel PEG-grafted PLGA films was very low, a feature which was employed to form protein micropatterns by preferential adsorption of proteins inside the PS holes exposed in the partially dewetted PEG-g-PLGA films. The resistance to hydrolytic degradation of the PEG-g-PLGA films in PBS, with respect to

the untreated PLGA films, was due to passivation by the PEG coating. Low protein adsorptive properties and degradation resistance, along with the general low cytotoxic nature of both PEG and PLGA, makes PEG-g-PLGA films an interesting platform for biological applications such as single cell study and cell cultures for tissue engineering.

References

1. Alves, N. M.; Pashkuleva, I.; Reis, R. L.; Mano, J. F., Controlling Cell Behavior through the Design of Polymer Surfaces. *Small* **2010**, *6*, 2208-2220.
2. Fukuda, J.; Khademhosseini, A.; Yeh, J.; Eng, G.; Cheng, J. J.; Farokhzad, O. C.; Langer, R., Micropatterned Cell Co-Cultures Using Layer-by-Layer Deposition of Extracellular Matrix Components. *Biomaterials* **2006**, *27*, 1479-1486.
3. Thissen, H.; Johnson, G.; Hartley, P. G.; Kingshott, P.; Griesser, H. J., Two-Dimensional Patterning of Thin Coatings for the Control of Tissue Outgrowth. *Biomaterials* **2006**, *27*, 35-43.
4. Mrksich, M.; Chen, C. S.; Xia, Y. N.; Dike, L. E.; Ingber, D. E.; Whitesides, G. M., Controlling Cell Attachment on Contoured Surfaces with Self-Assembled Monolayers of Alkanethiolates on Gold. *Proceedings of the National Academy of Sciences of the United States of America* **1996**, *93*, 10775-10778.
5. Lee, K. B.; Park, S. J.; Mirkin, C. A.; Smith, J. C.; Mrksich, M., Protein Nanoarrays Generated by Dip-Pen Nanolithography. *Science* **2002**, *295*, 1702-1705.
6. Chiu, D. T.; Jeon, N. L.; Huang, S.; Kane, R. S.; Wargo, C. J.; Choi, I. S.; Ingber, D. E.; Whitesides, G. M., Patterned Deposition of Cells and Proteins onto Surfaces by Using Three-Dimensional Microfluidic Systems. *Proceedings of the National Academy of Sciences of the United States of America* **2000**, *97*, 2408-2413.
7. Neto, C., A Novel Approach to the Micropatterning of Proteins Using Dewetting of Polymer Bilayers. *Physical Chemistry Chemical Physics* **2007**, *9*, 149-155.
8. Thickett, S. C.; Moses, J.; Gamble, J. R.; Neto, C., Micropatterned Substrates Made by Polymer Bilayer Dewetting and Collagen Nanoscale Assembly Support Endothelial Cell Adhesion. *Soft Matter* **2012**, *8*, 9996-10007.
9. Telford, A. M.; Meagher, L.; Glattauer, V.; Gengenbach, T. R.; Easton, C. D.; Neto, C., Micropatterning of Polymer Brushes: Grafting from Dewetting Polymer Films for Biological Applications. *Biomacromolecules* **2012**, *13*, 2989-2996.
10. Reiter, G., Dewetting of Thin Polymer Films. *Physical Review Letters* **1992**, *68*, 75-80.

11. Seemann, R.; Herminghaus, S.; Neto, C.; Schlagowski, S.; Podzimek, D.; Konrad, R.; Mantz, H.; Jacobs, K., Dynamics and Structure of Formation in Thin Polymer Melt Films. *Journal of Physics: Condensed Matter* **2005**, *17*, S267-S290.
12. Damman, P.; Baudalet, N.; Reiter, G., Dewetting near the Glass Transition: Transition from a Capillary Force Dominated to a Dissipation Dominated Regime. *Physical Review Letters* **2003**, *91*.
13. Choksakulnimitr, S.; Masuda, S.; Tokuda, H.; Takakura, Y.; Hashida, M., In-Vitro Cytotoxicity of Macromolecules in Different Cell-Culture Systems. *Journal of Controlled Release* **1995**, *34*, 233-241.
14. Lu, L.; Garcia, C. A.; Mikos, A. G., In Vitro Degradation of Thin Poly(D,L-Lactic-Co-Glycolic Acid) Films. *Journal of Biomedical Materials Research* **1999**, *46*, 236-244.
15. Grafahrend, D.; Heffels, K. H.; Beer, M. V.; Gasteier, P.; Moller, M.; Boehm, G.; Dalton, P. D.; Groll, J., Degradable Polyester Scaffolds with Controlled Surface Chemistry Combining Minimal Protein Adsorption with Specific Bioactivation. *Nature Materials* **2011**, *10*, 67-73.
16. Khang, G.; Jeon, J. H.; Lee, J. W.; Cho, S. C.; Lee, H. B., Cell and Platelet Adhesions on Plasma Glow Discharge-Treated Poly(Lactide-Co-Glycolide). *Bio-Medical Materials and Engineering* **1997**, *7*, 357-368.
17. Kundu, A. K.; Khatiwala, C. B.; Putnam, A. J., Extracellular Matrix Remodeling, Integrin Expression, and Downstream Signaling Pathways Influence the Osteogenic Differentiation of Mesenchymal Stem Cells on Poly(Lactide-Co-Glycolide) Substrates. *Tissue Engineering Part A* **2009**, *15*, 273-283.
18. Anderson, J. M.; Shive, M. S., Biodegradation and Biocompatibility of PLA and PLGA Microspheres. *Advanced Drug Delivery Reviews* **1997**, *28*, 5-24.
19. Kingshott, P.; Thissen, H.; Griesser, H. J., Effects of Cloud-Point Grafting, Chain Length, and Density of PEG Layers on Competitive Adsorption of Ocular Proteins. *Biomaterials* **2002**, *23*, 2043-2056.
20. Neto, C.; Jacobs, K.; Seemann, R.; Blossey, R.; Becker, J.; Grun, G., Correlated Dewetting Patterns in Thin Polystyrene Films. *Journal of Physics: Condensed Matter* **2003**, *15*, S421-S426.
21. Croll, T. I.; O'Connor, A. J.; Stevens, G. W.; Cooper-White, J. J., Controllable Surface Modification of Poly(Lactic-Co-Glycolic Acid) (PLGA) by Hydrolysis or Aminolysis I: Physical, Chemical, and Theoretical Aspects. *Biomacromolecules* **2004**, *5*, 463-473.
22. Gengenbach, T. R.; Chatelier, R. C.; Griesser, H. J., Characterization of the Ageing of Plasma-Deposited Polymer Films: Global Analysis of X-Ray Photoelectron Spectroscopy Data. *Surface and Interface Analysis* **1996**, *24*, 271-281.
23. Sauerbrey, G., Verwendung Von Schwingquarzen Zur Wagung Dunner Schichten Und Zur Mikrowagung. *Zeitschrift Fur Physik* **1959**, *155*, 206-222.

24. Jacobs, K.; Seemann, R.; Schatz, G.; Herminghaus, S., Growth of Holes in Liquid Films with Partial Slippage. *Langmuir* **1998**, *14*, 4961-4963.
25. Thickett, S.; Harris, A.; Neto, C., Interplay between Dewetting and Layer Inversion in P4VP/PS Bilayers. *Langmuir* **2010**, *26*, 15989-15999.
26. Steiner, U.; Klein, J.; Fetters, L. J., Surface Phase Inversion in Finite-Sized Binary-Mixtures. *Physical Review Letters* **1994**, *72*, 1498-1501.
27. Nam, Y. S.; Yoon, J. J.; Lee, J. G.; Park, T. G., Adhesion Behaviours of Hepatocytes Cultured onto Biodegradable Polymer Surface Modified by Alkali Hydrolysis Process. *Journal of Biomaterials Science, Polymer Edition* **1999**, *10*, 1145-1158.
28. Awodi, Y. W.; Johnson, A.; Peters, R. H.; Popoola, A. V., The Aminolysis of Poly(Ethylene-Terephthalate). *Journal of Applied Polymer Science* **1987**, *33*, 2503-2512.
29. Zhou, C.; Xu, J. X., Regioselective Nucleophilic Ring Opening Reactions of Unsymmetric Oxiranes. *Progress in Chemistry* **2011**, *23*, 165-180.
30. Upadhyayula, S.; Quinata, T.; Bishop, S.; Gupta, S.; Johnson, N. R.; Bahmani, B.; Bozhilov, K.; Stubbs, J.; Jreij, P.; Nallagatla, P.; Vullev, V. I., Coatings of Polyethylene Glycol for Suppressing Adhesion between Solid Microspheres and Flat Surfaces. *Langmuir* **2012**, *28*, 5059-5069.
31. Unsworth, L. D.; Tun, Z.; Sheardown, H.; Brash, J. L., Chemisorption of Thiolated Poly(Ethylene Oxide) to Gold: Surface Chain Densities Measured by Ellipsometry and Neutron Reflectometry. *Journal of Colloid and Interface Science* **2005**, *281*, 112-121.
32. Jo, S.; Park, K., Surface Modification Using Silanated Poly(Ethylene Glycol) *Biomaterials* **2000**, *21*, 605-616.
33. Telford, A. M.; James, M.; Meagher, L.; Neto, C., Thermally Cross-Linked PNVP Films as Antifouling Coatings for Biomedical Applications. *Applied Materials and Interfaces* **2010**, *2*, 2399-2408.
34. Xu, J. Q.; Sun, L.; Li, J.; Liang, J. L.; Zhang, H. M.; Yang, W. S., FITC and Ru(phen)(3)(2+) Co-Doped Silica Particles as Visualized Ratiometric pH Indicator. *Nanoscale Research Letters* **2011**, *6*, 561-567.
35. Ghezzi, M.; Thickett, S. C.; Neto, C., Early and Intermediate Stages of Guided Dewetting in Polystyrene Thin Films. *Langmuir* **2012**, *28*, 10147-10151.
36. Mayr, H.; Patz, M., Scales of Nucleophilicity and Electrophilicity - a System for Ordering Polar Organic and Organometallic Reactions. *Angewandte Chemie International Edition* **1994**, *33*, 938-957.
37. Pyun, J.; Kowalewski, T.; Matyjaszewski, K., Synthesis of Polymer Brushes Using Atom Transfer Radical Polymerization. *Macromolecular Rapid Communications* **2003**, *24*, 1043-1059.

38. Seth, R.; Yang, S.; Cho, S.; Sabeen, M.; Roberts, E. A., In Vitro Assessment of Copper-Induced Toxicity in the Human Hepatoma Line, Hep G. *Toxicology. in Vitro* **2004**, *18*, 501-509.
39. Hamilton-Brown, P.; Gengebach, T.; Griesser, H. J.; Meagher, L., End Terminal, Poly(Ethylene Oxide) Graft Layers: Surface Forces and Protein Adsorption. *Langmuir* **2009**, *25*, 9149-9156.
40. Kingshott, P.; Griesser, H. J., Surfaces That Resist Bioadhesion. *Current Opinion in Solid State and Materials Science* **1999**, *4*, 403-412.
41. Michel, R.; Pasche, S.; Textor, M.; Castner, D. G., Influence of PEG Architecture on Protein Adsorption and Conformation. *Langmuir* **2005**, *21*, 12327-12332.
42. Malmsten, M.; Emoto, K.; Van Alstine, J. M., Effect of Chain Density on Inhibition of Protein Adsorption by Poly(Ethylene Glycol) Based Coatings. *Journal of Colloids and Interface Science* **1998**, *202*, 507-517.
43. Harder, P.; Grunze, M.; Dahint, R.; Whitesides, G. M.; Laibinis, P. E., Molecular Conformation in Oligo(Ethylene Glycol)-Terminated Self-Assembled Monolayers on Gold and Silver Surfaces Determines Their Ability to Resist Protein Adsorption. *Journal of Physical Chemistry B* **1998**, *102*, 426-436.
44. Ladd, J.; Zhang, Z.; Chen, S.; Hower, J. C.; Jiang, S., Zwitterionic Polymers Exhibiting High Resistance to Nonspecific Protein Adsorption from Human Serum and Plasma. *Biomacromolecules* **2008**, *9*, 1357-1361.
45. Barbey, R.; Kauffmann, E.; Ehrat, M.; Klok, H. A., Protein Microarrays Based on Polymer Brushes Prepared Via Surface-Initiated Atom Transfer Radical Polymerization. *Biomacromolecules* **2010**, *11*, 3467-3479.
46. Yamamoto, Y.; Nishihara, H.; Aramaki, K., Self-Assembled Layers of Alkanethiols on Copper for Protection against Corrosion. *Journal of The Electrochemical Society* **1993**, *140*, 436-443.
47. Zamborini, F. P.; Crooks, R. M., Corrosion Passivation of Gold by N-Alkanethiol Self-Assembled Monolayers: Effect of Chain Length and End Group. *Langmuir* **1998**, *14*, 3279-3286.

Chapter 4.

Guided Dewetting by Microcontact Printing

4.1. Introduction

The stability of thin polymer films on rigid substrates has received significant attention in the past two decades due to their use as coatings, lubricants or protective layers.¹⁻³ The stability of polymer films depends on the film thickness as well as the forces at the interface between the polymer and the solid. For film thicknesses below the capillary length, gravitational forces can be neglected and film stability is governed by intermolecular forces. Short- and long-range forces determine the effective interfacial potential, $\phi(h)$, between the polymer and the surface, which determines whether a polymer thin film is stable, unstable or metastable.⁴⁻⁸ Macroscopically, the film stability depends on the surface wettability.⁹ Polymer films on non-wettable substrates are unstable and dewet from the solid surface upon annealing above the glass transition temperature (T_g). Dewetting leads to the rupture of the initially homogeneous film, typically by nucleation of holes on film defects and/or spots with high residual stress.¹⁰ ¹¹ Continuous annealing of the film causes the holes to grow in size until coalescence with neighbouring holes, producing polymer ribbons which decay further into an assembly of polymer droplets due to Rayleigh instability.^{12, 13}

Polymer dewetting has attracted growing interest as a versatile and robust process to form surface patterns.¹⁴⁻¹⁷ Control over hole size is possible by tuning the annealing time and temperature, but control over hole location is not straightforward on an uniform substrate, as holes nucleate randomly. Lateral order in the dewetting pattern can be imposed by tailoring substrate wettability, typically by microcontact printing

(μ CP) of self-assembling monolayers (SAMs).¹⁸⁻²² Extensive experimental and theoretical work has shown how the features of a surface pattern affect dimension and position of the polymer droplets in the final stage of dewetting.²³⁻²⁸ However, to our knowledge, no prior work exists on the early and intermediate stages of dewetting on chemically heterogeneous substrates. The term 'early' refers to the very beginning of polymer dewetting, i.e. when the polymer film breaks up and holes grow independently without interaction with the neighbouring ones. The term 'intermediate' refers to the stage of polymer dewetting after holes coalescence but before droplet formation. Here we investigated polystyrene (PS) thin films, spin-coated onto silicon wafers with a native oxide layer (Si/SiO₂) previously patterned with a SAM of octadecyltrichlorosilane (OTS) by μ CP. The employed stamp for μ CP has a square grid pattern, which resulted in stripes of hydrophobic OTS and square regions of uncoated Si/SiO₂ (Figure 4.1a).

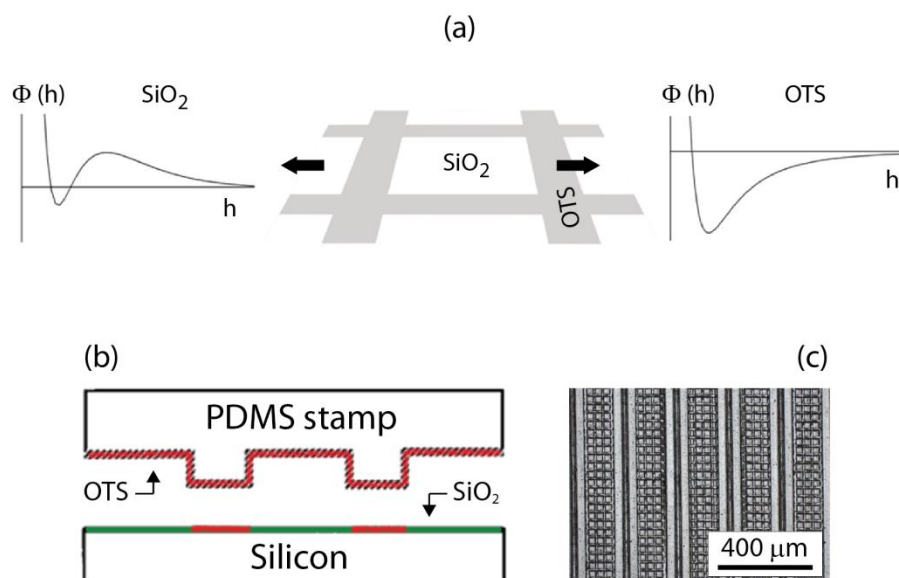


Figure 4.1. (a) Schematic diagram of an OTS-patterned Si/SiO₂ substrate and the corresponding effective interface potentials, $\phi(h)$, as a function of the PS film thickness (h). (b) Schematic depiction of μ CP of an OTS self-assembling monolayer on a Si/SiO₂ substrate. (c) Optical micrograph of the PDMS stamp employed for μ CP. The relief protrusions of the stamp correspond to the dark areas of the optical micrograph.

The effective interface potential for PS thin films on silicon substrates with a native layer of SiO₂ (ϕ_{SiO_2}) and on OTS-coated silicon substrates with a native layer of SiO₂ (ϕ_{OTS}) are, respectively:⁶

$$\phi_{\text{SiO}_2}(h) = \frac{c_{\text{SiO}_2}}{h^8} - \frac{A_{\text{SiO}_2}}{12\pi h^2} + \frac{A_{\text{SiO}_2} - A_{\text{Si}}}{12\pi (h + d_{\text{SiO}_2})^2} \quad (4.1)$$

$$\phi_{\text{OTS}}(h) = \frac{c_{\text{OTS}}}{h^8} - \frac{A_{\text{OTS}}}{12\pi h^2} + \frac{A_{\text{OTS}} - A_{\text{SiO}_2}}{12\pi (h + d_{\text{OTS}})^2} + \frac{A_{\text{SiO}_2} - A_{\text{Si}}}{12\pi (h + d_{\text{OTS}} + d_{\text{SiO}_2})^2} \quad (4.2)$$

where c_{SiO_2} and c_{OTS} denote the strength of the short-range part of the potential; A_{SiO_2} , A_{Si} and A_{OTS} are the Hamaker constants of PS on SiO₂, Si and OTS, respectively; h is the thickness of the PS film; d_{SiO_2} and d_{OTS} are the thickness of the native layer SiO₂ and the thickness of the OTS layer, respectively. The effective interface potential $\phi(h)$ for PS on the OTS-coated Si/SiO₂ substrate is typical of an unstable film, with a deep minimum and no barrier to dewetting.⁵ On plain Si/SiO₂, $\phi(h)$ for PS is that of a metastable film, with a significant barrier to dewetting and a shallower minimum, which experimentally result in no dewetting (Figure 4.2). Here we investigated the effects of the chemical pattern on the evolution of the hole morphology and on dynamics of the hole growth.

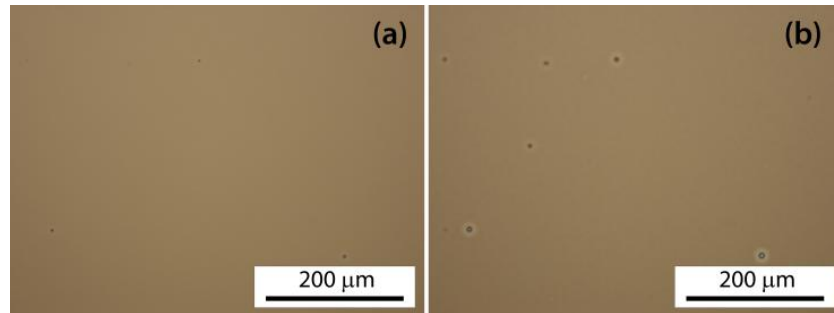


Figure 4.2. Optical micrographs of a PS 2k film (thickness: 54.6 ± 0.5 nm) on piranha cleaned Si/SiO₂ substrate. (a) Before annealing. (b) After thermal annealing at 100°C for 5 hours. No evidence of polymer dewetting emerged from the comparison of both images, not even around dust particles/defects on the film that usually act as nucleation spots. The same annealing conditions led to complete dewetting of the PS 2k film on OTS-patterned Si/SiO₂ substrate.

4.2. Materials and Methods

4.2.1. Sample preparation

Prime grade silicon wafers coated with a 1.9 nm thick native oxide layer (Si/SiO₂; MMRC Pty. Ltd., Australia) were subjected to microcontact printing (μ CP) to form micrometer scale patterns of octadecyltrichlorosilane (OTS; 90%+, Sigma-Aldrich) self-assembled monolayers (SAMs)²⁹ using a polydimethylsiloxane stamp (PDMS; Bandwidth Foundry, Sydney), according to a standard procedure described by Xia *et al.*³⁰ (Figure 4.1b). Briefly, substrates were cleaned by heating at 70 °C for 30 min in piranha solution (a mixture of 7:3 (v/v) of 98% H₂SO₄ and 30% H₂O₂), thoroughly rinsed with Milli-Q water, and used immediately. The ‘ink’ used in μ CP was a 0.2% (w/w) solution of OTS in toluene. The stamp was left in contact with the Si/SiO₂ substrates for 1 min under the pressure of 200 grams weight, and then sonicated in toluene to remove unreacted OTS. Uniform OTS self-assembled monolayers (thickness 2.3 ± 0.1 nm) on Si/SiO₂ substrates were prepared by A/Prof Chiara Neto using an established procedure.^{31, 32}

The polymers employed in the present work were atactic polystyrene (PS) of two different molecular weights: PS 2k (M_n 1920 g mol⁻¹; \bar{D} 1.08) and PS 96k (M_n 96000 g mol⁻¹; \bar{D} 1.04), (Polymer Standard Service, Germany). Polymer films were cast on the OTS-patterned substrates by spin-coating (Laurell Technologies Co., model 400B-6NPP-LITE). PS films on top of uniform OTS monolayers were prepared by dip floating the films in water and used as control samples.¹⁷ PS can not be deposited on OTS by spin coating from toluene solution because toluene does not wet the OTS layer, and upon spinning the solution droplet rolls off the substrate, with no resulting polymer film on the substrate. Dip-floating is common practice in the field to obviate this problem. Dip-floating deposition consists in first spin coating the polymer film on a wettable substrate (mica) and then transferring it on the non-wettable substrate through floating on water.

Since most of the experiments were performed using PS 2k, in the following sections PS will refer to PS 2k, unless otherwise specified.

4.2.2. Surface characterization

Typical thicknesses of spin-coated PS films were 55 nm for PS 2k (20 mg mL⁻¹ in toluene, 4000 RPM; measured by spectroscopic ellipsometry (J.A. Woollam Co. Inc., model M-2000V; see Section 2.2) and 35 nm for PS 96k (10 mg mL⁻¹ in toluene, 3000 RPM). The wetting properties of the employed materials were investigated by measuring the advancing and receding contact angles of 4-8 μ L sessile droplets of Milli-Q water with a KSV CAM200 Contact Angle System (KSV Instruments Ltd., Helsinki, Finland), as described in Section 2.4. The static, advancing, and receding contact angle of water were measured at four different locations on six different samples, and the average and standard deviation of these values were calculated (results are summarized in Table 4.1). Polymer annealing was performed on a hot plate (ATV Technologie GMBH, model TR-124) with control over the set temperature of 0.1 °C. PS 2k was annealed at 70 °C to 100 °C. For PS films of thickness around 50 nm, T_g is significantly lower than bulk and the onset of polymer dewetting was observed at 62 °C.³³ PS 96k films were annealed at 160 °C to 200 °C. After annealing, the substrates were placed on a surface at room temperature, so that the temperature rapidly dropped below the T_g , causing film dewetting to be arrested. Dewetting patterns were observed and characterized by atomic force microscopy (Bruker Multimode VIII; see Section 2.3) and optical microscopy (Nikon LV150).

Table 4.1. Water contact angle on the employed surfaces. Uncertainties results from the statistical analysis of multiple measurements (four measurements per sample, six samples per type).

	Contact Angle (°)		
	Static	Advancing	Receding
Si/SiO₂	< 10	< 10	< 10
OTS pattern	82 ± 1	86 ± 1	48 ± 1
OTS monolayer	111 ± 1	112 ± 1	88 ± 4
PS 2k	94 ± 1	96 ± 1	78 ± 1
PS 96k	94 ± 1	98 ± 1	77 ± 1

4.3. Results and Discussion

4.3.1. Spatially-ordered dewetting patterns

The stamping process produced a number of defects in the polymer film, more numerous than on the homogeneous OTS coatings. The polymer film was uneven on top the OTS grid due to the presence of OTS aggregates of height below 5 nm (Figure 4.3). The resulting RMS roughness of PS films on the OTS stripes was 1.0 ± 0.1 nm, whereas on the unpatterned background it was around 0.3 nm (similar to that of bare Si/SiO₂ and OTS monolayer, both around 0.2 nm).

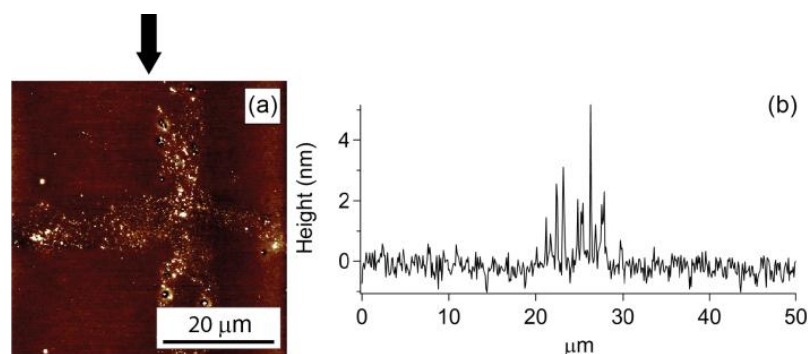


Figure 4.3. Morphology of PS film on a stripe of the OTS square grid pattern before annealing. (a) AFM topography. (b) Cross section obtained from AFM topography, in correspondence of the black arrow.

The dewetting of a PS film on an OTS-patterned Si/SiO₂ substrate at 70 °C and then at 100 °C is shown in Figure 4.4. In the sample before annealing (Figure 4.4a) an array of square grid patterned OTS was visible underneath the PS film, due to the OTS layer thickness, which was of the order of a few nanometres due to local polymerization of the silane.³⁴ As soon as the film was annealed above T_g , PS began to dewet via nucleated holes at random locations on the OTS grid (Figure 4.4b, Figure 4.4c). Dewetting by heterogeneous nucleation starts with the random nucleation of holes at sites of local heterogeneity in the film.³⁵ Therefore, the dewetting of PS on OTS-patterned silicon initiated in correspondence of the morphological defects in the polymer film introduced by the μ CP process (Figure 4.3). In the early stages of annealing, roughly circular holes grew symmetrically on the OTS stripes until their diameter matched the width of the OTS stripes. In later stages of dewetting, the holes

became elongated (see Section 4.3.2), and eventually coalesced with neighboring holes. The polymer ribbons formed at the contact line of two coalescing holes broke down into small droplets by Rayleigh instability. These small droplets can be seen inside the OTS-coated channels (Figure 4.4d). Dewetting of the PS film from the non-wettable OTS pattern at 70 °C led to an ordered grid-shaped pattern of PS channels, mirroring the underlying OTS pattern (Figure 4.4d). While dewetting progressed steadily in the initial and intermediate stages of dewetting (see times in Figure 4.4a-d), after PS dewetted completely from the OTS-strips (Figure 4.4d) no further movement of the contact line occurred in the following 60 minutes of annealing at 70 °C. Increasing the annealing temperature up to 100 °C caused the PS film to start dewetting also from the rest of the Si/SiO₂ substrate (Figure 4.4e, f). The rim of the film retracted further to the centre of the uncoated part of the grid, until all PS accumulated into an ordered array of large droplets. The pattern with ordered array of polymer droplets could not be obtained by prolonged annealing at 70 °C, as the dewetting driving force at this temperature was not strong enough to overcome both the pinning of the contact line on the OTS border and the increasing dissipation along the rim of the hole (see Section 4.3.2).

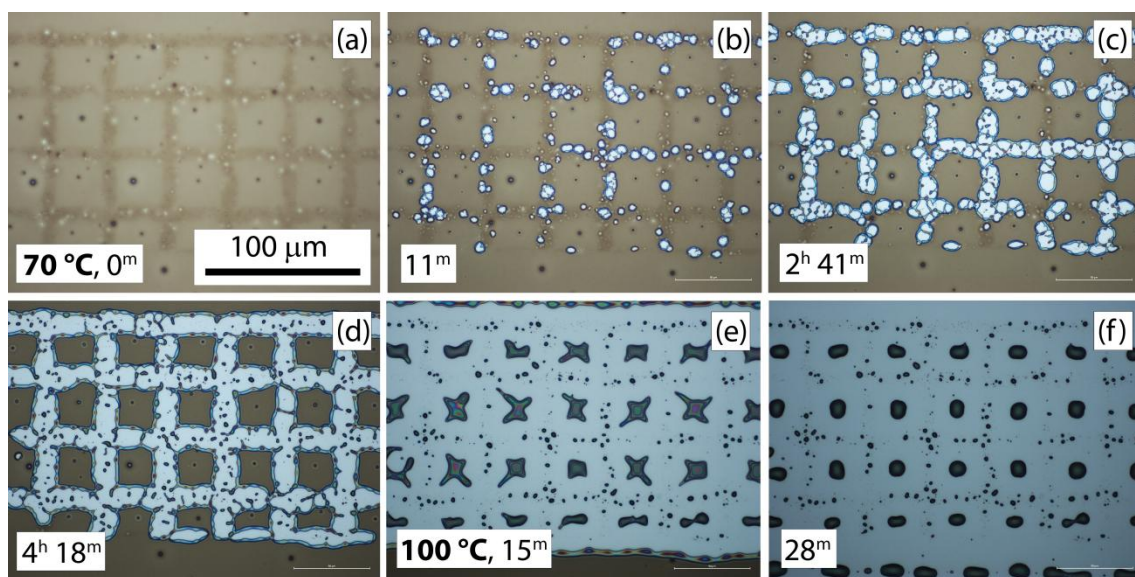


Figure 4.4. Optical micrographs showing a typical real time dewetting of a PS film (54.1 ± 0.2 nm) on a Si/SiO₂ substrate patterned with a square grid SAM of OTS. Light areas are dewetted areas of the polymer film; dark areas are intact areas of the polymer film or droplets. Annealing temperature: (a-d) 70 °C, (e-f) 100 °C. Increase of annealing temperature occurs at 4h 18m 21s, i.e. just after capture of image (d). Annealing time and temperature are indicated in each micrograph.

In this manner, two different surface patterns with topographically ordered features could be obtained by simply tuning the annealing conditions (Figure 4.5). Annealing temperatures slightly higher than the T_g confined the dewetting of the PS film within the OTS square grid pattern. The result was a dewetted film with an array of channels with width of ~ 11 - $14\ \mu\text{m}$ separated by rows of squares or lines of PS $\sim 50\ \mu\text{m}$ wide (Figure 4.5a, c), in good agreement with the features of the PDMS stamp (Figure 4.1c). For films of thickness $52.8 \pm 0.6\ \text{nm}$, the semi-cylindrical PS rims formed at the border of the channels (from the accumulated PS removed from the stripe) had height of about $150\ \text{nm}$; channel depth was about $44 \pm 5\ \text{nm}$. The width and spacing of the polymer pattern was determined by the stamp, whereas channel depth and rim height could be tuned by varying the initial PS film thickness.⁶

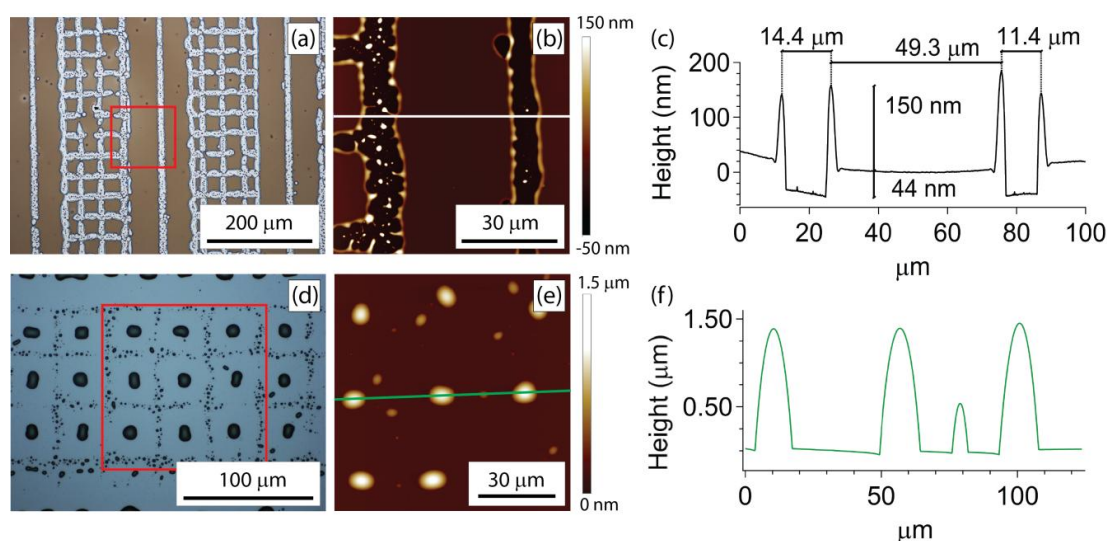


Figure 4.5. Ordered patterns obtained by guided dewetting of PS on OTS-patterned Si/SiO₂. (a-c) Intermediate dewetting pattern resulting from low temperature (70 °C) annealing. (d-f) Final dewetting pattern resulting from high temperature (100 °C) annealing. Optical micrographs (a, d), AFM topography images (b, e), and line cross-sections obtained from AFM topography images (c, f) are shown.

Prolonged high temperature annealing of the sample (100 °C, 2h) resulted in complete dewetting of the PS film and the formation of an array of polymer droplets with positions guided by the underlying OTS pattern: large droplets located in the center of the grid and small droplets on the frame of the OTS pattern (Figure 4.5d, e). Statistical analysis confirmed the presence of a narrow bimodal size distribution of PS

droplets: large droplets with diameter $11.1 \pm 0.4 \mu\text{m}$ and height of $1.4 \pm 0.1 \mu\text{m}$, and small droplets with diameter $3.8 \pm 0.8 \mu\text{m}$ and height $0.7 \pm 0.2 \mu\text{m}$. The quoted values are mean values and the uncertainties are standard deviations of the size distribution. For non-spherical drops we used the equivalent diameter, i.e. the diameter of a circle with same area. Control over both droplet diameter and height is possible by varying stamp periodicity and film thickness, respectively, to obtain the desired size distribution.²¹ The contact angle of PS droplets measured from AFM images was $25^\circ \pm 4^\circ$, i.e. a value intermediate between that expected on SiO_2 (6.9°) and that on OTS (58°).³⁶

Three possible factors contributed to the complete dewetting of PS on the non-silanized background: firstly, it is well established that in μCP the ink can “bleed out” of the pattern during the stamping, which in turn results in blurry edges and/or SAM patches outside the main pattern.³⁷ Contact angle measurement of PS droplets confirmed this hypothesis, as the contact angle of PS was intermediate between that on SiO_2 and on OTS, which is consistent with a composite surface outside the OTS grid.³⁸ Secondly, the abundance of defects on OTS-patterned Si/SiO_2 (Figure 4.4a) could facilitate the otherwise slow dewetting on bare Si/SiO_2 . Thirdly, when the annealing temperature was increased to 100°C , the viscosity of the polymer film decreased significantly³⁹ leading to a much more fluid film, in which the dewetting driving force dominated over the viscous forces, which would have otherwise slowed down the dewetting on Si/SiO_2 .

PS 96k thin films showed a dewetting evolution similar to that described for PS 2k (Figure 4.6), except that in PS 96k a larger numbers of small polymer droplets formed on the OTS grid, consistent with the observed greater density of nucleated holes for high molecular weight polymers. The hole density on a solid substrate by dewetting via heterogeneous nucleation depends on the molecular weight of the polymer used because longer polymer chains are typically more entangled and lead to a higher degree of strain within the film, which in turn may result in a higher hole density.¹¹

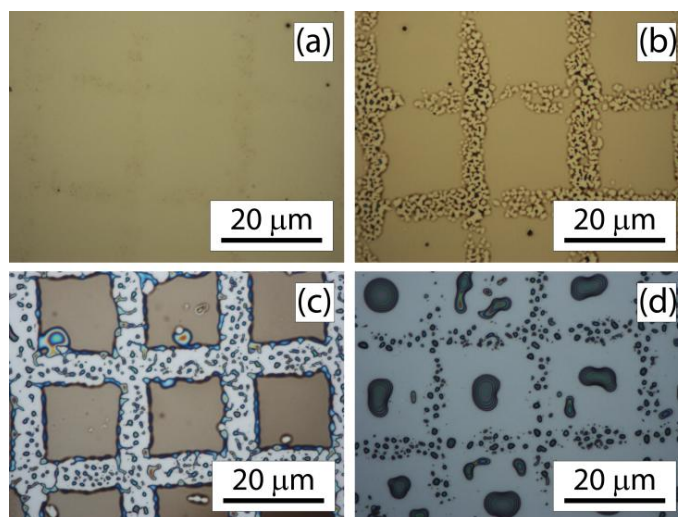


Figure 4.6. Optical micrographs showing a typical real time dewetting of a PS 96k film (30.1 ± 0.2 nm) on a silicon substrate patterned with a SAM of OTS. Annealing temperature and progressive annealing time: (a) before annealing; (b) 160°C, 20 s; (c) 160°C, 1 min ; (d) 200°C, 7 hours. Increase of annealing temperature occurred just after capture of image (c).

4.3.2. Dynamics of hole growth

The growth dynamics of a representative and isolated hole on top of an OTS-patterned Si/SiO₂ substrate is shown in Figure 4.7a. Initially, when the hole diameter was smaller than the width of the underlying OTS stripe (around 8 μm), dewetting propagated symmetrically in all directions, producing circular holes and a linear hole growth with time. Once the hole diameter matched the width of the OTS stripe, the dynamics of hole growth became affected by the underlying OTS pattern.

When the rim of the dewetted hole approached the OTS boundary, polymer dewetting became asymmetrical, leading to ellipsoidal holes with different dewetting rates along the long axis (L , faster) and the short axis (S , slower) of the hole. Due to surface tension, the growth of ellipsoidal holes is less favored than that of circular holes, resulting in a decrease of the overall dewetting rate (Figure 4.7b, Slow (I)). Then, the contact line became physically pinned at the OTS border and the growth along the short axis, S , was consequently constricted, leading to a plateau of the hole growth ($dR/dt = 0$) along both axes of the ellipsoids (Figure 4.7b, Slow (II)). The plateau of the dewetting rate also along L is a consequence of the constricted growth along S : when there is no more displacement of the contact line along S , surface tension forces the

contact line along L to stop moving in order to avoid a further increase of the aspect ratio of the hole (L/S). Conversely, the dewetting rate for a PS film on a uniform OTS is positive at all times ($dR/dt > 0$), as shown for comparison in Figure 4.7a, and can be modelled accounting for viscous forces and interfacial slip.^{40, 41}

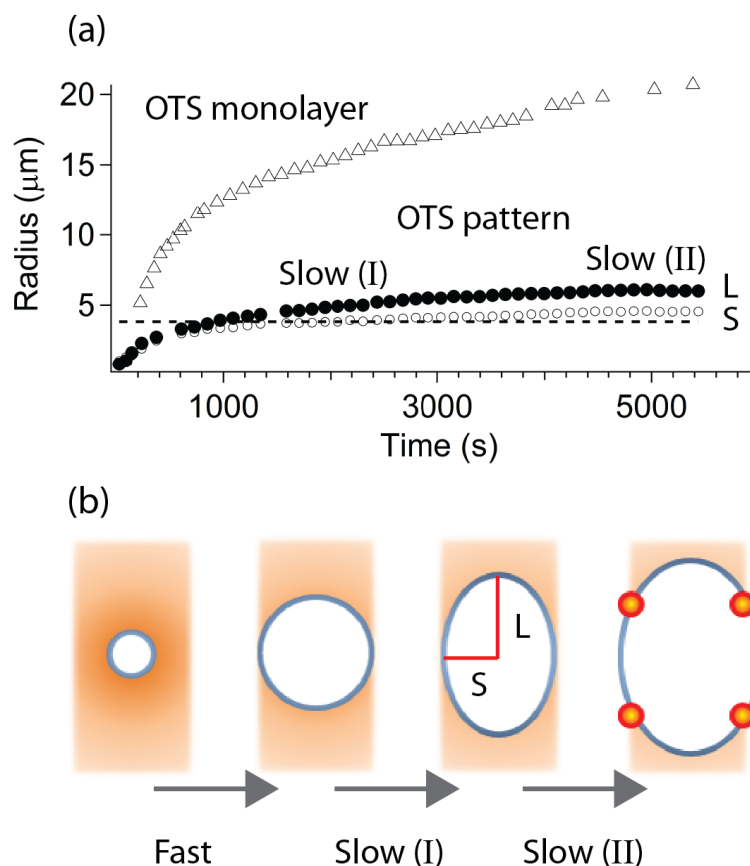


Figure 4.7. (a) Typical dynamics of hole growth in a PS film on an uniform OTS monolayer (Δ) and on an OTS-patterned substrate (\bullet , \circ) upon annealing at constant temperature (70 °C). The OTS pattern induced the growth of ellipsoidal holes: L (\bullet) is the long axis of the hole; S (\circ) is the short axis of the hole. The dashed line represents the average half width of the OTS stripe underneath the PS film determined from Figure 1c. (b) Schematic depiction of hole growth on an OTS stripe (orange rectangle). The initial fast growth of circular holes is followed by a slow step due to the unfavourable transition from circular to ellipsoidal holes (Slow (I)). Further retraction of the PS causes the contact line to pin on the OTS boundary, leading to the plateau of the growth rate (Slow (II)).

Additionally, PS films with similar thickness (about 55 nm) and same annealing temperature (70 °C) produced larger and more regular holes on a uniform OTS monolayer than on the OTS-patterned substrate, due to a more uniform SAM underlying

the polymer film (Figure 4.8). The wettability of the silane layer depends on the quality of the layer: true self-assembled monolayers have higher contact angles because water interacts with only methyl groups, whereas disordered multilayers expose also silanol groups to the solvent. In turn, different wettability of the substrate results in a different dewetting rate of the polymer film.⁴²

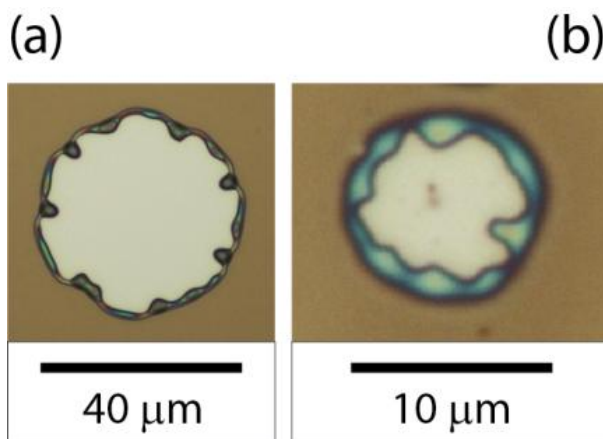


Figure 4.8. Comparative analysis of hole morphology on substrates with different degree of uniformity. (a) On a homogeneous OTS monolayer. (b) Holes formed on top of OTS-patterned substrates..

4.4. Summary

In the present work we investigated the early and intermediate stages of PS dewetting on OTS-patterned Si/SiO₂ substrates. Microcontact printing of SAMs selectively guided the dewetting of polymer thin films, producing surface patterns with topographically ordered features. Polymer dewetting is an effective and reliable way to transfer and amplify the features of a bidimensional SAM pattern into a three dimensional polymer pattern. Two different types of patterns were achieved by tuning the annealing conditions (time and temperature): low temperature annealing led to an ordered pattern of polymer channels mirroring the underlying OTS pattern. High temperature and prolonged annealing led to a bimodal distribution of polymer droplets in an ordered array, with position and dimension guided by the underlying OTS pattern.

The dynamics of hole growth became affected by the pattern as soon as the hole size approached the pattern size, with contact line pinning and reduced dewetting forces outside the pattern as main reasons for the stop in hole growth. This guided approach

could be useful in extending the use of polymer dewetting to applications in protein patterning, cell studies and biosensing requiring topographical order.

References

1. Lee, L. P.; Szema, R., Inspirations from Biological, Optics for Advanced Photonic Systems. *Science* **2005**, *310*, 1148-1150.
2. Squires, T. M.; Quake, S. R., Microfluidics: Fluid Physics at the Nanoliter Scale. *Reviews of Modern Physics* **2005**, *77*, 977-1026.
3. Langer, R.; Tirrell, D. A., Designing Materials for Biology and Medicine. *Nature* **2004**, *428*, 487-492.
4. Konnur, R.; Kargupta, K.; Sharma, A., Instability and Morphology of Thin Liquid Films on Chemically Heterogeneous Substrates. *Physical Review Letters* **2000**, *84*, 931-934.
5. Seemann, R.; Herminghaus, S.; Jacobs, K., Dewetting Patterns and Molecular Forces: A Reconciliation. *Physical Review Letters* **2001**, *86*, 5534-5537.
6. Seemann, R.; Herminghaus, S.; Jacobs, K., Gaining Control of Pattern Formation of Dewetting Liquid Films. *Journal of Physics: Condensed Matter* **2001**, *13*, 4925-4938.
7. Muller-Buschbaum, P., Dewetting and Pattern Formation in Thin Polymer Films as Investigated in Real and Reciprocal Space. *Journal of Physics: Condensed Matter* **2003**, *15*, R1549-R1582.
8. Craster, R. V.; Matar, O. K., Dynamics and Stability of Thin Liquid Films. *Reviews of Modern Physics* **2009**, *81*, 1131-1198.
9. De Gennes, P. G.; Brochard-Wyart, F.; Quere, D., *Capillarity and Wetting Phenomena: Drops, Bubbles, Pearls, Waves*. New York, 2003.
10. Jacobs, K.; Herminghaus, S.; Mecke, K., Thin Liquid Polymer Films Rupture Via Defects. *Langmuir* **1998**, *14*, 965-969.
11. Reiter, G.; Hamieh, M.; Damman, P.; Slavovs, S.; Gabriele, S.; Vilmin, T.; Raphael, E., Residual Stresses in Thin Polymer Films Cause Rupture and Dominate Early Stages of Dewetting. *Nature Materials* **2005**, *4*, 754-758.
12. Reiter, G., Dewetting of Thin Polymer Films. *Physical Review Letters* **1992**, *68*, 75-80.
13. Sharma, A.; Reiter, G., Instability of Thin Polymer Films on Coated Substrates: Rupture, Dewetting, and Drop Formation. *Journal of Colloid and Interface Science* **1996**, *178*, 383-399.

14. Gentili, D.; Foschi, G.; Valle, F.; Cavallini, M.; Biscarini, F., Applications of Dewetting in Micro and Nanotechnology. *Chemical Society Reviews* **2012**, *41*, 4430-4443.
15. Xue, L. J.; Han, Y. C., Pattern Formation by Dewetting of Polymer Thin Film. *Progress in Polymer Science* **2011**, *36*, 269-293.
16. Becker, J.; Grun, G.; Seemann, R.; Mantz, H.; Jacobs, K.; Mecke, K. R.; Blossey, R., Complex Dewetting Scenarios Captured by Thin-Film Models. *Nature Materials* **2003**, *2*, 59-63.
17. Neto, C., A Novel Approach to the Micropatterning of Proteins Using Dewetting of Polymer Bilayers. *Physical Chemistry Chemical Physics* **2007**, *9*, 149-155.
18. Braun, H. G.; Meyer, E., Thin Microstructured Polymer Films by Surface-Directed Film Formation. *Thin Solid Films* **1999**, *345*, 222-228.
19. Ermi, B. D.; Nisato, G.; Douglas, J. F.; Rogers, J. A.; Karim, A., Coupling between Phase Separation and Surface Deformation Modes in Self-Organizing Polymer Blend Films. *Physical Review Letters* **1998**, *81*, 3900-3903.
20. Luo, C. X.; Xing, R. B.; Zhang, Z. X.; Fu, J.; Han, Y. C., Ordered Droplet Formation by Thin Polymer Film Dewetting on a Stripe-Patterned Substrate. *Journal of Colloid and Interface Science* **2004**, *269*, 158-163.
21. Sehgal, A.; Ferreira, V.; Douglas, J. F.; Amis, E. J.; Karim, A., Pattern-Directed Dewetting of Ultrathin Polymer Films. *Langmuir* **2002**, *18*, 7041-7048.
22. Zhang, Z. X.; Wang, Z.; Xing, R. B.; Han, Y. C., Patterning Thin Polymer Films by Surface-Directed Dewetting and Pattern Transfer. *Polymer* **2003**, *44*, 3737-3743.
23. Bandyopadhyay, D.; Sharma, A., Self-Organized Microstructures in Thin Bilayers on Chemically Patterned Substrates. *Journal of Physical Chemistry C* **2010**, *114*, 2237-2247.
24. Julthongpiput, D.; Zhang, W. H.; Douglas, J. F.; Karim, A.; Fasolka, M. J., Pattern-Directed to Isotropic Dewetting Transition in Polymer Films on Micropatterned Surfaces with Differential Surface Energy Contrast. *Soft Matter* **2007**, *3*, 613-618.
25. Kargupta, K.; Sharma, A., Morphological Self-Organization by Dewetting in Thin Films on Chemically Patterned Substrates. *Journal of Chemical Physics* **2002**, *116*, 3042-3051.
26. Mukherjee, R.; Bandyopadhyay, D.; Sharma, A., Control of Morphology in Pattern Directed Dewetting of Thin Polymer Films. *Soft Matter* **2008**, *4*, 2086-2097.
27. Patra, A.; Bandyopadhyay, D.; Tomar, G.; Sharma, A.; Biswas, G., Instability and Dewetting of Ultrathin Solid Viscoelastic Films on Homogeneous and Heterogeneous Substrates. *Journal of Chemical Physics* **2011**, *134*.
28. Xia, Y. N.; Qin, D.; Yin, Y. D., Surface Patterning and Its Application in Wetting/Dewetting Studies. *Current Opinion in Colloid and Interface Science* **2001**, *6*, 54-64.

29. Wang, D. W.; Thomas, S. G.; Wang, K. L.; Xia, Y. N.; Whitesides, G. M., Nanometer Scale Patterning and Pattern Transfer on Amorphous Si, Crystalline Si, and SiO₂ Surfaces Using Self-Assembled Monolayers. *Applied Physics Letters* **1997**, *70*, 1593-1595.
30. Xia, Y. N.; Mrksich, M.; Kim, E.; Whitesides, G. M., Microcontact Printing of Octadecylsiloxane on the Surface of Silicon Dioxide and Its Application in Microfabrication. *Journal of the American Chemical Society* **1995**, *117*, 9576-9577.
31. Sagiv, J., Organized Monolayers by Adsorption .1. Formation and Structure of Oleophobic Mixed Monolayers on Solid-Surfaces. *Journal of the American Chemical Society* **1980**, *102*, 92-98.
32. Brzoska, J. B.; Benazouz, I.; Rondelez, F., Silanization of Solid Substrates - a Step toward Reproducibility. *Langmuir* **1994**, *10*, 4367-4373.
33. Herminghaus, S.; Jacobs, K.; Seemann, R., The Glass Transition of Thin Polymer Films: Some Questions, and a Possible Answer. *European Physical Journal E* **2001**, *5*, 531-538.
34. Fadeev, A. Y.; McCarthy, T. J., Self-Assembly Is Not the Only Reaction Possible between Alkyltrichlorosilanes and Surfaces: Monomolecular and Oligomeric Covalently Attached Layers of Dichloro- and Trichloroalkylsilanes on Silicon. *Langmuir* **2000**, *16*, 7268-7274.
35. Seemann, R.; Jacobs, K.; Blossey, R., Polystyrene Nanodroplets. *Journal of Physics: Condensed Matter* **2001**, *13*, 4915-4923.
36. Pompe, T.; Fery, A.; Herminghaus, S.; Kriele, A.; Lorenz, H.; Kotthaus, J. P., Submicron Contact Printing on Silicon Using Stamp Pads. *Langmuir* **1999**, *15*, 2398-2401.
37. Cassie, A. B. D.; Baxter, S., Wettability of Porous Surfaces. *Transactions of the Faraday Society* **1944**, *40*, 0546-0550.
38. Hao, T., Viscosities of Liquids, Colloidal Suspensions, and Polymeric Systems under Zero or Non-Zero Electric Field. *Advances in Colloid and Interface Science* **2008**, *142*, 1-19.
39. Jacobs, K.; Seemann, R.; Schatz, G.; Herminghaus, S., Growth of Holes in Liquid Films with Partial Slippage. *Langmuir* **1998**, *14*, 4961-4963.
40. Fetzer, R.; Jacobs, K.; Munch, A.; Wagner, B.; Witelski, T. P., New Slip Regimes and the Shape of Dewetting Thin Liquid Films. *Physical Review Letters* **2005**, *95*.
41. Seemann, R.; Herminghaus, S.; Neto, C.; Schlagowski, S.; Podzimek, D.; Konrad, R.; Mantz, H.; Jacobs, K., Dynamics and Structure of Formation in Thin Polymer Melt Films. *Journal of Physics: Condensed Matter* **2005**, *17*, S267-S290.

Chapter 5.

Guided Dewetting by Colloidal Imprinting

5.1. Introduction

Pattern formation in thin polymer thin films by spontaneous dewetting is a robust and versatile method to produce surface coatings with controlled chemistry and topography, and with functional properties.¹⁻⁵ Control over the hole size is possible by finely tuning the annealing time and temperature, as well as the molecular weight of the polymer.⁶ Patterns arising from the dewetting of thin polymer films typically consist of randomly distributed holes. However, lateral order in the dewetting pattern can be imposed by introducing chemical and/or physical heterogeneities on the substrate.^{7, 8} For example, the Neto group employed microcontact printing of self-assembled monolayers to induce ordered dewetting of polystyrene from hydrophobised regions of a silicon wafer.⁹

Colloidal lithography has been developed as a versatile approach for the generation of nanometer-scale chemical and topographical patterns spanning large areas.^{10, 11} This method exploits two-dimensional (2D) arrays of self-assembled spherical particles as templates for surface patterning. The advantage of 2D colloidal crystals in nanofabrication and surface patterning is that large-area self-assembly of colloids with well-ordered structures can be achieved without the need for expensive equipment.¹² Typical routes for the fabrication of hexagonally-arranged monolayers and multilayers of colloidal particles include spin coating,¹³ drop-casting,¹⁴ controlled evaporation,¹⁵ and layer-by-layer deposition.¹⁶ Kingshott *et al.* have succeeded in the growth of large area 2D multi-component colloidal crystals a broad range of size ratios by using the evaporation induced confined area assembly method.¹⁶⁻¹⁸ To date, a large

number of surface patterns consisting of arrays of various nanostructures (rings, dots, rods, cavities)^{19, 20} have been fabricated by CL using 2D colloidal crystal templates as masks or molds for evaporation,²¹ etching,²² deposition,²³ and imprinting.²⁴ In particular, colloidal imprinting consists in the use of 2D colloidal crystals as molds for mechanical deformation of imprint resists, typically a polymer film or a curable monomer.^{25, 26} Jang *et al.*²⁷ reported the imprinting of silica nanosphere arrays into polystyrene films by thermal treatment, producing ordered arrays of nanoholes in the polymer film after removal of the embedded particles.

In this study, colloidal imprinting was used for the first time to guide the dewetting of thin polymer films in an ordered fashion leading to spatially-ordered arrays of holes (Figure 5.1). The thermal imprinting of 2D colloidal crystals, made of either single silica particles and binary silica/poly(methyl methacrylate) (PMMA) particles, was used to pattern ordered arrays of holes on polymer bilayers consisting in poly(4-vinylpyridine) (P4VP) thin films on top of polystyrene (PS) thin films (Figure 5.1, step (i) and (ii)). After removing the particles (Figure 5.1, step (iii)), the spatially-ordered holes produced by colloidal imprinting were grown in size and depth by dewetting of the P4VP top layer on PS upon annealing above the glass transition temperature of P4VP (Figure 5.1, step (iv)). P4VP/PS bilayers were the substrate of choice as the P4VP top layer offers good hydrophilicity required for the assembly of silica-based colloidal crystals, and the Neto group has shown that P4VP films dewet readily on top of PS.^{2, 28} Coupling polymer dewetting to colloidal imprinting led to surface micropatterns that are both topographical and chemical in nature, consisting of arrays of holes with tunable size and depth. The main advantage of the approach proposed in this Chapter with respect to conventional colloidal imprinting is the ability to grow the hole size in lateral size and in height in the post-lithographic stage, without the need to employ colloidal crystals with different particle size to vary the hole size.

5.2. Materials and Methods

5.2.1. Preparation of polymer bilayers and surface characterization

Polymer bilayers were prepared on prime grade silicon wafers (MMRC Pty. Ltd., Australia), previously cleaned as described in Section 2.1.²⁰ Polystyrene (PS; Polymer

Standard Service, Germany) was spin-cast in films on clean silicon wafers from a 20 mg mL⁻¹ toluene solution (anhydrous, 99.8 %; Sigma-Aldrich) (3000 RPM for 1 min). Polystyrene with two different molecular weights were employed in the present work: PS96 (M_n 96000 g mol⁻¹, \bar{D} 1.04) and PS236 (M_n 236000 g mol⁻¹, \bar{D} 1.05). Poly(4-vinylpyridine) (P4VP, M_n 19000 g mol⁻¹; Sigma-Aldrich) was then spin-cast on top of the PS films from a 10 mg mL⁻¹ ethanol solution (> 99.9%, Merck) (3000 RPM for 1 min). P4VP films on top of hydrophobised (octadecyltrichlorosilane, OTS-coated) silicon wafers were prepared by dip floating the films on water.⁹ Dip-floating deposition consists in first spin coating the polymer film on a wettable substrate (mica) and then transferring it on the non-wettable substrate through floating on water. Uniform OTS self-assembled monolayers (thickness 2.3 ± 0.1 nm) on Si/SiO₂ substrates were prepared by A/Prof Chiara Neto using an established procedure.²⁹

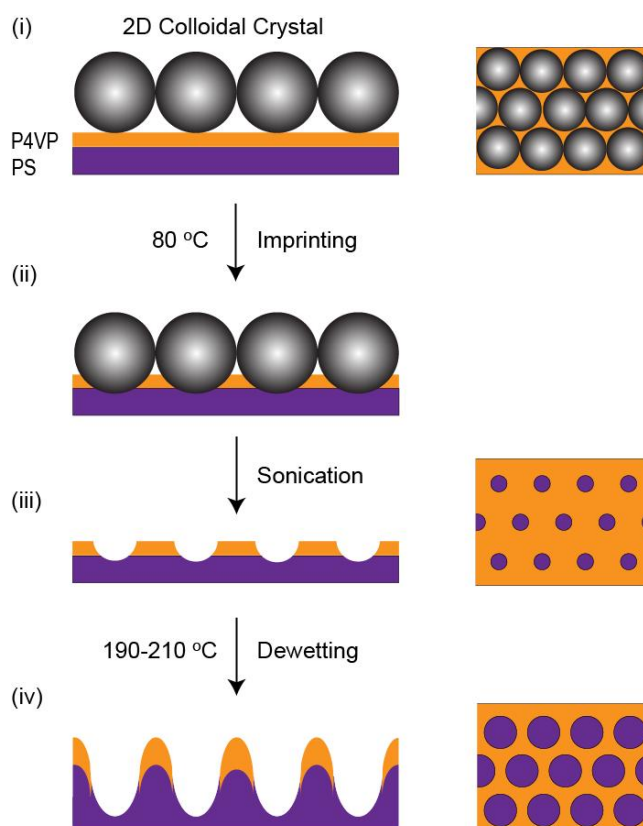


Figure 5.1. Schematic representation of the fabrication of ordered arrays of holes with tunable size and depth by colloidal imprinting on P4VP/PS bilayers followed by dewetting of P4VP films on PS films via thermal annealing.

The average thickness of the films obtained was 75 ± 2 nm for PS and 40 ± 2 nm for P4VP, as determined by spectroscopic ellipsometry (Woollam Co. Inc. M-2000), as described in Section 2.2. Both as-prepared films were smooth, with root-mean-square (RMS) roughness lower than 0.3 nm, as measured by atomic force microscopy (AFM, Bruker Multimode VIII) using Tapping Mode[®] in air on 3×3 μm scan area.

5.2.2. Preparation of colloidal crystals

Colloidal crystals were fabricated based on evaporation induced confined area assembly (EICAA).¹¹ Silica colloidal crystals were prepared using 5 μm silica particles (Bangs Lab, Fisher IN, USA). Binary colloidal crystals were prepared using 5 μm silica particles and 0.4 μm poly(methyl methacrylate) (PMMA) particles (Bangs Lab, Fisher IN, USA), with silica:PMMA number ratio of 1:3289. Prior to use, colloidal solutions were fully suspended using sonication and vortexing. The colloidal suspension was pipetted inside the area confined by a 0.5 cm diameter rubber ring. The amount of colloidal particles needed to form a monolayer was calculated on the basis of the area encircled by the rubber ring. The samples were kept at room temperature until complete evaporation of the solvent. Some of the P4VP/PS bilayers were treated with UV/ozone (UVO) for 10 minutes in order to increase the hydrophilicity of the P4VP top layers. The colloidal crystals were assembled on top of P4VP/PS bilayers by Dr Peng Yuan Wang at the Industrial Research Institute Swinburne (IRIS), Swinburne University of Technology.

The mass ratio between silica particles and PMMA particles was calculated as follows. The volume of silica (V_{silica}) and PMMA (V_{PMMA}) particles are given by:

$$V_{\text{silica}} = \frac{4}{3}\pi R_{\text{silica}}^3 = 6.5 \cdot 10^{-11} \text{cm}^3 \quad (5.1)$$

$$V_{\text{PMMA}} = \frac{4}{3}\pi R_{\text{PMMA}}^3 = 3.4 \cdot 10^{-14} \text{cm}^3 \quad (5.2)$$

where R_{silica} and R_{PMMA} are the radius of silica (2.5 μm) and PMMA (0.2 μm) particles, respectively. From particle volume, we calculated the mass of silica (m_{silica}) and PMMA (m_{PMMA}) particles:

$$m_{\text{silica}} = V_{\text{silica}} \rho_{\text{silica}} = 1.7 \cdot 10^{-10} \text{g} \quad (5.3)$$

$$m_{\text{PMMA}} = V_{\text{PMMA}} \rho_{\text{PMMA}} = 4.0 \cdot 10^{-14} \text{g} \quad (5.4)$$

where ρ_{silica} and ρ_{PMMA} are the density of silica (2.65 g cm^{-3}) and PMMA (1.18 g cm^{-3}). The mass ratio between silica and PMMA particles is then given by:

$$\frac{m_{\text{silica}}}{m_{\text{PMMA}}} \approx 4320 \quad (5.5)$$

5.2.3. Collidal imprinting

Colloidal imprinting was carried out by thermal annealing of the 2D colloidal crystals assembled on top of the P4VP/PS bilayers. Thermal annealing was performed at $80 \text{ }^{\circ}\text{C}$ for 1 min in air on a hot plate with fine temperature control (ATV Technologie GmbH, Germany). After thermal annealing, the colloidal crystals were removed from the polymer bilayers by sonication in Milli-Q water ($5 \times 1 \text{ min}$).

5.2.4. Dewetting of imprinted P4VP/PS bilayers

Dewetting of the imprinted P4VP films on top of PS was performed by annealing the polymer bilayers above the glass transition temperature of P4VP ($141 \text{ }^{\circ}\text{C}$), as determined by differential scanning calorimetry (DSC; see Section 2.5) (Figure 5.2). typically at temperatures between 160 and $210 \text{ }^{\circ}\text{C}$. The real-time evolution of the dewetting patterns was monitored by *in-situ* imaging with a Bruker Multimode VIII AFM equipped with a heating scanner (Bruker, model 9242JVHC), as described in Section 2.3.

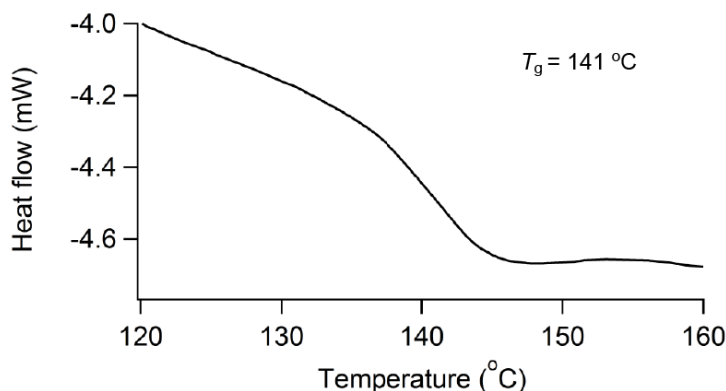


Figure 5.2. Differential scanning calorimetry (DSC) of P4VP powder. The glass transition temperature (T_g) is indicated.

5.3. Results

5.3.1. Binary colloidal crystals

Figure 5.3 shows a typical binary colloidal crystals produced by the self-assembly of a monolayer of 5 μm silica particles and several layers of 0.4 μm PMMA particles on top of P4VP/PS96 bilayers. The colloidal crystal employed consisted of uniform distribution of closely-packed small PMMA particles around large silica particles arranged in hexagonal arrays. Both silica and PMMA particles penetrated into the P4VP/PS96 bilayer upon colloidal imprinting (80 $^{\circ}\text{C}$, 1 min), leading to micropatterned polymer surfaces with bimodal distribution of holes mirroring the position and size of the particles in the colloidal crystal (Figure 5.3b).

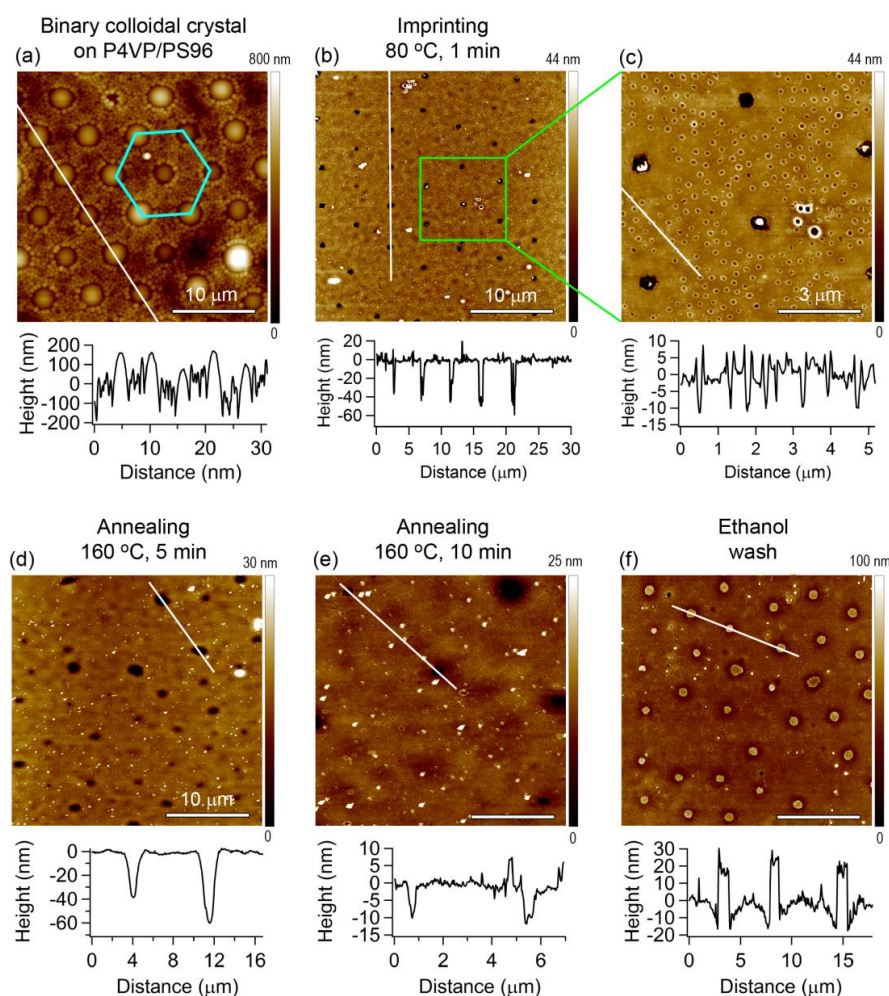


Figure 5.3. AFM topography images of (a) a binary colloidal crystal assembled on a P4VP/PS96 bilayer, and micropatterned P4VP/PS bilayers after (b, c) colloidal imprinting at 80 $^{\circ}\text{C}$ for 1 min, (d, e) annealing at 160 $^{\circ}\text{C}$, (f) selective dissolution of P4VP with ethanol. Line-cross sections from the AFM topography images are shown below each image.

Hexagonal arrays of holes with 590 ± 50 nm diameter produced by the imprinting of the large silica particles were surrounded by a uniform distribution of holes with 140 ± 20 nm diameter produced by the imprinting of the small PMMA particles (Figure 5.3c). The size distribution of the imprinted holes was strikingly narrow, and this level of control applies also to the hole depth. The average depth of the holes resulting from the imprinting of silica particles (50 ± 10 nm) was around five times higher than that of PMMA particles (10 ± 4 nm), due to the weight difference between the two types of particles: the mass of a $5\text{ }\mu\text{m}$ silica particle was approx. 4000 times larger than that of a $0.4\text{ }\mu\text{m}$ PMMA particle (Section 5.2), leading to deeper penetration of silica particles into the P4VP/PS bilayers. The average distance between the large holes was $5.7 \pm 0.2\text{ }\mu\text{m}$, and $0.52 \pm 0.05\text{ }\mu\text{m}$ for the small holes, which are close to the average distance between silica particles ($5.9 \pm 0.2\text{ }\mu\text{m}$) and PMMA particles ($0.48 \pm 0.09\text{ }\mu\text{m}$), respectively, in the colloidal crystal.

As the Neto group has shown before, uniform P4VP films dewet on top of PS films by random nucleation of holes, leading to the formation of micropatterned polymer surfaces featuring randomly distributed arrays of holes.^{2, 28} In the imprinted P4VP/PS96 bilayers, annealing at $160\text{ }^{\circ}\text{C}$ for 5 min caused an initial very slow dewetting, with growth of the large holes from 590 ± 50 to 810 ± 60 nm (Figure 5.3d). Subsequently, dewetting stopped, with most of the holes closing-up when the annealing time was prolonged beyond 10 min (Figure 5.3e). The average depth of the large holes progressively decreased from 50 ± 10 nm before annealing, to 24 ± 12 nm and 14 ± 7 nm after 5 and 10 min at $160\text{ }^{\circ}\text{C}$, respectively. Similar observations and measurements were obtained on all the investigated samples (5 samples).

The closure of the large imprinted holes is believed to be caused by layer inversion in the P4VP/PS96 bilayers. Layer inversion occurs in polymer melt bilayers, when the polymer bottom layer has a lower surface tension than the polymer top layer and tends to migrate to the air interface.³⁰ Layer inversion in P4VP/PS bilayers annealed above $160\text{ }^{\circ}\text{C}$ has been already documented by Thickett *et al.*²⁸ In the present work, layer inversion was confirmed by AFM imaging of annealed P4VP/PS96 films after ethanol washing. Ethanol is a solvent for P4VP, but a nonsolvent for PS. Selective dissolution of the P4VP top layer revealed PS arrays of vertical cylinders (Figure 5.3f), produced by the migration of PS96 to the air interface through the imprinted holes. Migration of PS96 to the air interface was facilitated since the imprinted holes in the

P4VP films were deeper (50 ± 10 nm) than the thickness of the P4VP top layer (40 ± 2 nm), exposing therefore the underlying PS film to the air. The small holes in P4VP/PS96 bilayers produced by imprinting with $0.4\ \mu\text{m}$ PMMA particles readily closed-up upon annealing at $160\ ^\circ\text{C}$ for 5 minutes, as the holes were more shallow and surface tension effects smoothed-out the film.³¹

As the role of the smaller PMMA particles is mainly to increase the order in the silica particle arrays,³² they were selectively removed prior to indentation by acetonitrile washing (Figure 5.4). Acetonitrile is a good solvent for PMMA and a non-solvent for both P4VP and PS. Figure 3b shows that acetonitrile selectively removed only the PMMA particles from the binary colloidal crystal, leaving on the P4VP top layer ordered arrays of $5\ \mu\text{m}$ silica particles assembled with hexagonal arrangement and average particle distance of $5.9 \pm 0.2\ \mu\text{m}$. Despite not being a solvent for P4VP, the acetonitrile wash disrupted the P4VP film surface. After colloidal imprinting ($80\ ^\circ\text{C}$, 1 min), the surface of the P4VP/PS96 bilayers showed a bimodal distribution of holes, consisting of ordered arrays of imprinted due to the silica colloidal particles (diameter: $1.16 \pm 0.07\ \mu\text{m}$; depth: 56 ± 14 nm), plus a number of disordered, shallow and large holes (diameter: $5 \pm 3\ \mu\text{m}$; depth: 22 ± 8 nm) positioned at random locations on the surface (Figure 5.4c).

The surface of P4VP films between the indentation holes lost its initial smoothness, with the appearance of undulations resampling spinodal dewetting.³³ These undulations are believed to be the consequence of the spontaneous solvent-induced dewetting of P4VP occurred during washing with acetonitrile.³⁴ Annealing of the imprinted P4VP/PS96 bilayers at $160\ ^\circ\text{C}$ for 30 min caused the imprinted holes to close-up (Figure 5.4d, part (i)), while some of the randomly distributed holes showed significant growth in depth (86 ± 10 nm) without significant change in the lateral size ($5 \pm 2\ \mu\text{m}$) (Figure 5.4d, part (ii)). The pattern degradation shown in Figure 5.4d is believed to be the results of the combined effects of layer inversion in the P4VP/PS96 bilayer, and nucleation induced by acetonitrile washing.

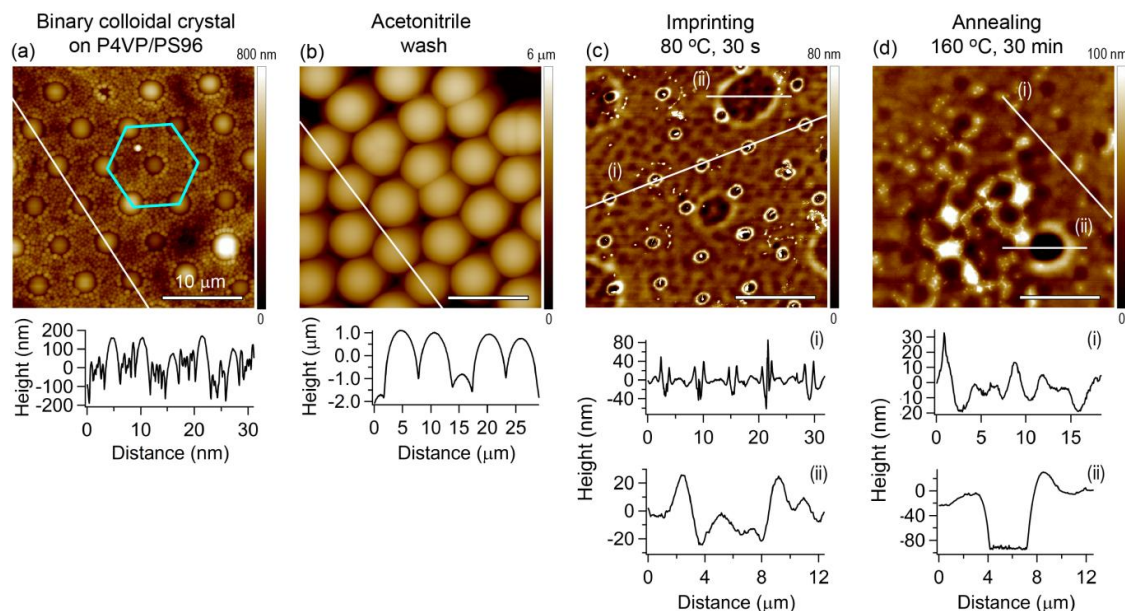


Figure 5.4. (a-b) AFM topography images of binary colloidal crystal assembled on a P4VP/PS96 bilayer (a) before and (b) after removal of the PMMA particle by selective dissolution with acetonitrile. (c-d) AFM topography images of micropatterned P4VP/PS bilayers after (c) colloidal imprinting at 80 °C for 1 min and (d) annealing at 160 °C for 30 min. Line-cross sections from the AFM topography images are shown below each image.

5.3.2. Single-particle colloidal crystals

The results on the binary colloidal crystals presented in the previous section indicated that the dewetting of the P4VP top layer was affected by the interplay of two competing processes: layer inversion in the P4VP/PS bilayers and the smoothing-over in the imprinted P4VP films driven by surface tension. Layer inversion is governed by the melt viscosity of the PS bottom layer and can be slowed-down by using PS with higher MW (PS236). The interplay between polymer dewetting and layer inversion in P4VP/PS bilayers is largely governed by the melt state viscosity (η_0) of the polymer bottom bottom layer, which scales as $\eta_0 \propto MW^{3.5}$.³⁵ The surface tension in the P4VP films is related to density of imprinted holes and can be reduced by using single-particle silica colloidal crystals to produce arrays of imprinted holes with lower density.

Single-particle colloidal crystals obtained with 5 μm silica particles on P4VP/PS236 bilayers (Figure 5.5a) showed lower degree of long-range order than binary silica/PMMA colloidal crystals (Figure 5.4). In the binary colloidal crystals, strong attractive capillary forces between the small PMMA particles guided the ordered

self-assembly of silica particles over large areas.³⁶ Colloidal imprinting on the P4VP/PS236 bilayers with single-particle colloidal crystals (80 °C, 1 min) produced arrays of holes with 770 ± 20 nm diameter and 49 ± 5 nm depth, mirroring the position of the silica particles in the colloidal crystal (Figure 5.5b). The average distance between the imprinted holes was 5.5 ± 0.7 μm , which was comparable to the distance between the silica particles (5.2 ± 0.3 μm).

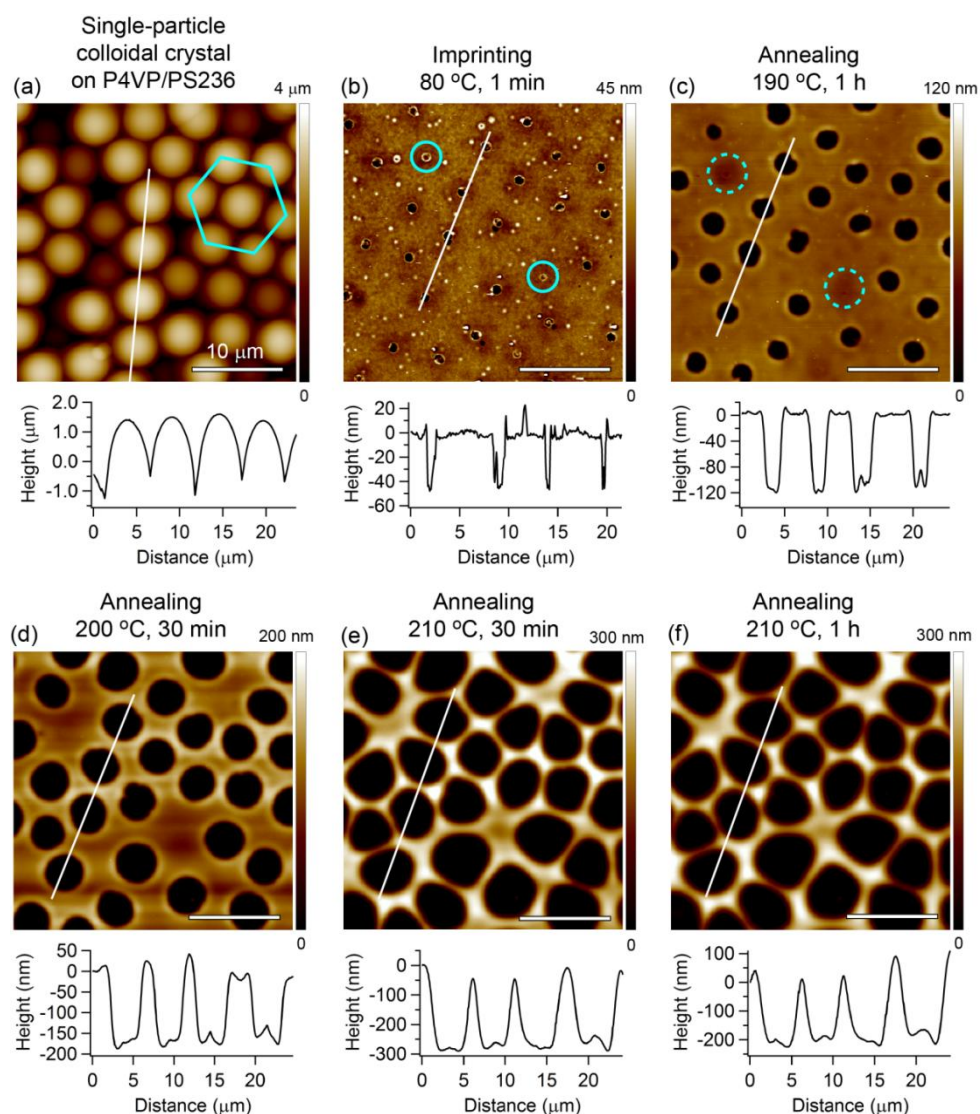


Figure 5.5. AFM topography images of (a) a single-particle colloidal crystal assembled on a P4VP/PS236 bilayer. (b-f) AFM topography images of the same area of a micropatterned P4VP/PS236 bilayer after (b) colloidal imprinting at 80 °C for 1 min, (c-f) and annealing at 190-210 °C for increasing times. The same area was imaged *in situ* in parts (b)-(f). Line-cross sections from the AFM topography images are shown below each image.

Annealing of the P4VP/PS236 bilayers at temperatures between 190 and 210 °C caused the imprinted holes to dewet and grow in size (Figure 5.5c-d), till coalescence with neighbouring holes (Figure 5.5e-f), producing surface micropatterns consisting in arrays of holes with tuneable size. Imprinted P4VP films dewetted on top of the underlying PS236 films by site-specific nucleation initiated by the imprinted holes. The depth of the imprinted holes was a key parameter for the successful hole growth. Only holes with initial depth larger than the thickness of the P4VP film (40 ± 2 nm) acted as nucleii for the dewetting of the polymer film, while shallower holes (e.g. Figure 5.5b, encircled areas; depth 11 ± 3 nm) closed up upon thermal annealing (Figure 5.5c, encircled areas). As mentioned in the previous section, the reason is believed to be related to the interfacial stress in the polymer film.³¹

The dynamics of hole growth showed the simultaneous increase in both diameter and depth of the holes in the P4VP/PS236 bilayers during annealing at temperatures between 190 and 210 °C (Figure 5.6). The annealing temperature was initially set at 190 °C in order to monitor the early stages of dewetting, and then raised up to 210 °C to counteract the decrease in the dewetting rate caused by viscous dissipation within the polymer film.³⁷ During annealing, holes steadily grew in diameter from an initial value of 770 ± 20 nm after imprinting up to a maximum value of 5.2 ± 0.5 μ m, when coalescence occurred (Figure 5.6a). Hole depth gradually increased from 49 ± 5 nm after imprinting up to a maximum of 300 ± 50 nm. Polymer rims formed around the holes due to the displacement and accumulation of P4VP during dewetting, and reached a height of around 50-100 nm (Figure 5.6b). However, the height of the rims could be roughly estimated only in the early stages of dewetting (Figure 5.5d), before the coalescence of the rims into polymer ribbons. For this reason, the depth values reported for dewetted holes refer to the total peak-to-valley distance.

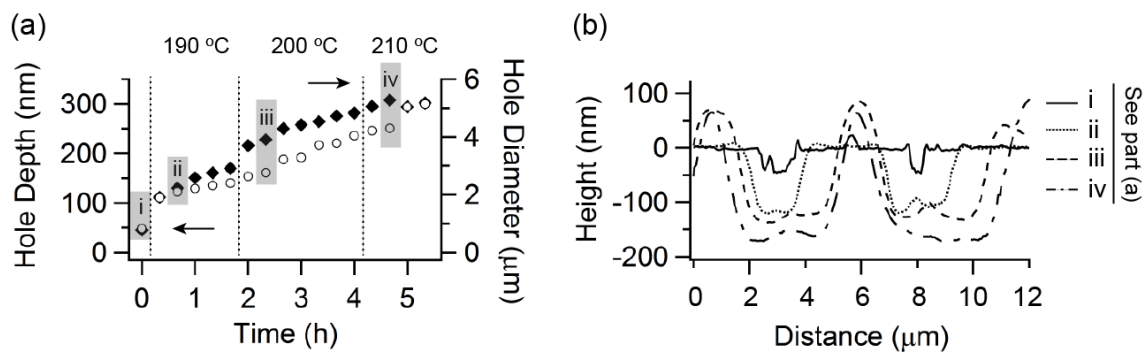


Figure 5.6. (a) Dynamics of growth of holes produced by colloidal imprinting of single-particle colloidal crystal on P4VP/PS236 bilayers as a function of annealing time and temperature. Error bars are of the same size of the symbols used in the plot. (b) Evolution of the cross-section of two representative neighboring holes (from AFM images) during annealing at 190 – 210 °C. The indices (i) to (iv) refer to the times in part (a).

Selective dissolution of the dewetted P4VP films by ethanol washing was used to gain a deeper insight into the mechanism governing the dewetting of imprinted P4VP/PS236 bilayers. The selective removal of P4VP revealed that dewetting affected also the underlying PS surfaces, creating arrays of holes with double rim mirroring the patterns observed before solvent washing (Figure 5.7). The average hole diameter in the PS films was identical to that of P4VP/PS236 bilayers before ethanol washing ($5.2 \pm 0.5 \mu\text{m}$), whereas the average depth of the holes decreased from $300 \pm 50 \text{ nm}$ (before) to $200 \pm 50 \text{ nm}$ (after). The comparison between the line-cross section before and after ethanol washing showed that the rims observed in P4VP/PS bilayers consisted of P4VP accumulated on top of PS domains raised above the surface during annealing above the T_g (Figure 5.7c). The presence of relief domains of PS underneath the holes' rim represented a major contribution to formation of holes in P4VP/PS with depth approx three times higher than the initial thickness of the bilayers ($115 \pm 5 \text{ nm}$).

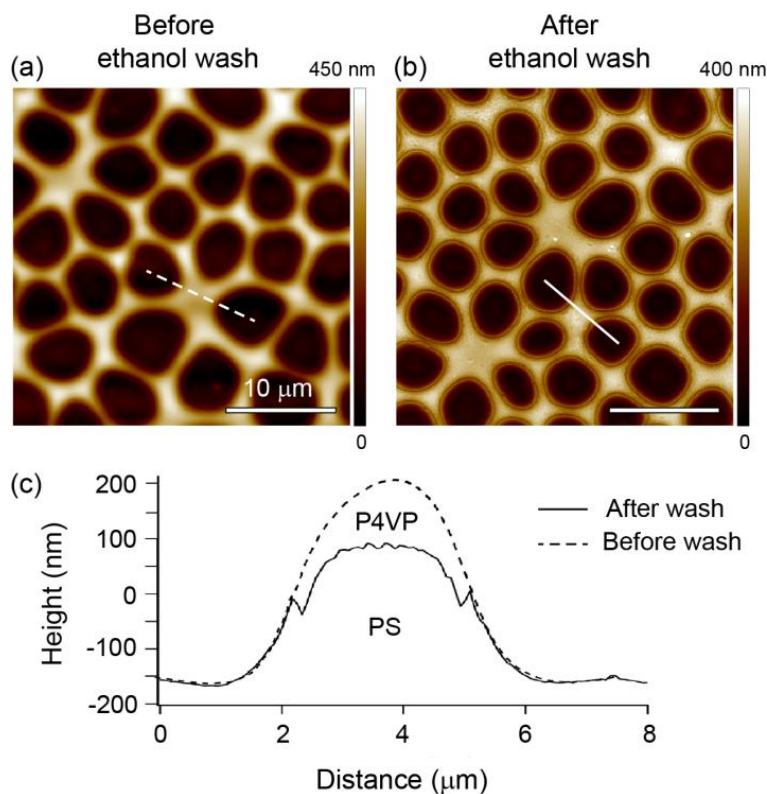


Figure 5.7. (a-b) AFM topography images of P4VP/PS236 bilayers micropatterned by colloidal imprinting with single-particle silica colloidal crystals followed by polymer dewetting (a) before and (b) after selective P4VP dissolution with ethanol. (c) Line-cross sections from the AFM topography images before (dashed line) and after ethanol wash (solid line).

These observations are evidence of partial layer inversion occurred in P4VP/PS236 bilayers after prolonged annealing at 190-210 °C, i.e. above the T_g of both P4VP and PS. However, differently from what observed during the dewetting of imprinted P4VP/PS96 bilayers (Figure 5.3), layer inversion was not the dominant effect and did not inhibit polymer dewetting. The decrease in the viscosity of polystyrene bottom layer achieved by using high-MW (PS236), instead of PS96 used in Figures 5.3 and 5.4, significantly reduced the rate of layer inversion, and allowed the P4VP top layer to dewet upon annealing.³⁸

The formation of extended single-particle colloidal crystals with long-range order is known to depend on the wettability of substrate, since the self-assembly of the colloidal particles is driven by the intermolecular forces existing between the particles and between the particles and the substrate.^{11, 32} To increase the order of the 5 μm silica particle arrays, the hydrophilicity of P4VP was increased by treatment with UV/ozone

(UVO) for 10 min. UVO treatment is well known to generate hydrophilic groups (e.g. OH, C=O and COOH) on polymer surfaces, and it has been widely used to increase the wettability of polymer films without changing the bulk properties of the polymer.³⁹ The UVO treatment led to the formation of extended colloidal crystals of silica particles with ordered hexagonal arrangement (Figure 5.8a). Colloidal imprinting (80 °C, 1 min) produced P4VP/PS236 bilayers showing long-range arrays of holes (diameter: 780 ± 30 nm; depth: 55 ± 5 nm) with hexagonal arrangement mirroring the colloidal crystal used as template (Figure 5.8b).

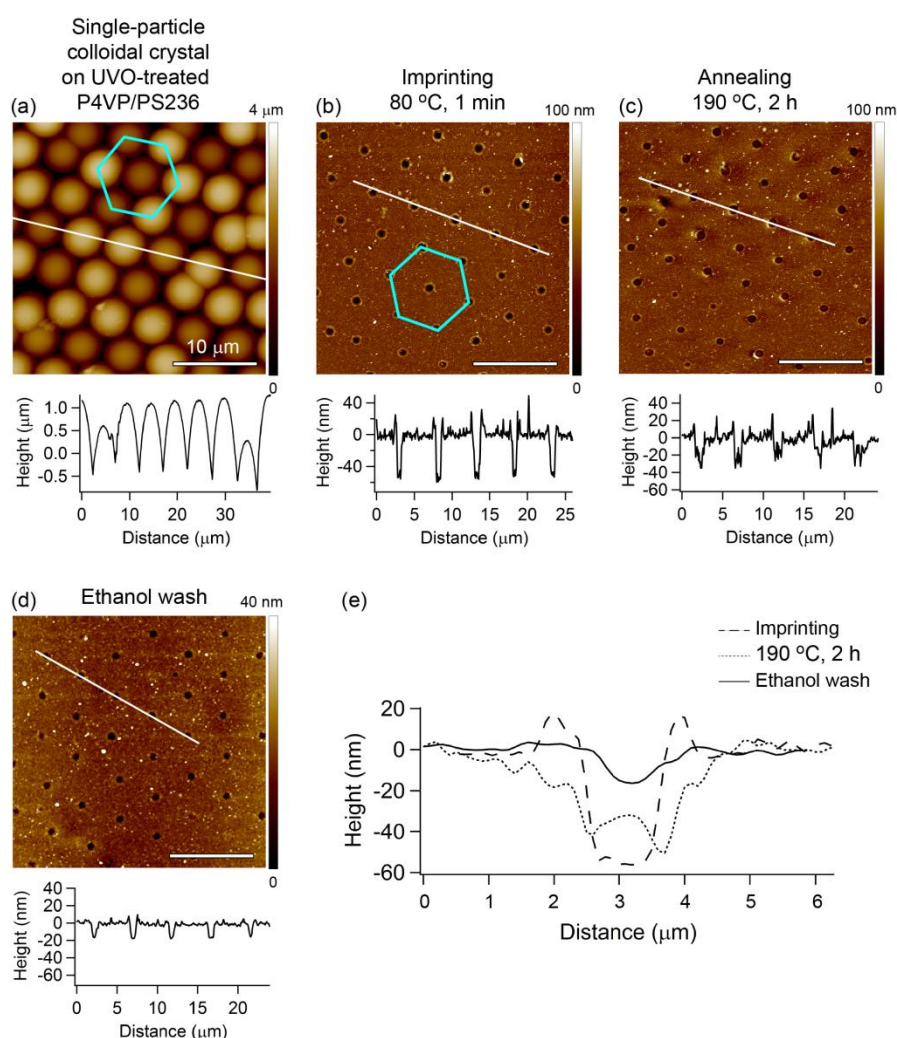


Figure 5.8. AFM topography images and line-cross sections of (a) a single-particle colloidal crystal assembled on a UV/ozone (UVO)-treated P4VP/PS236 bilayer, and micropatterned P4VP/PS bilayers after (b) colloidal imprinting at 80 °C for 1 min, (c) annealing at 190 °C for 2 h, (d) selective dissolution of P4VP with ethanol. (e) Line-cross sections from the AFM topography images showing the real-time evolution of (i) a representative imprinted hole after (ii) annealing at 190 °C for 2 h, and (iii) ethanol wash.

Upon annealing, the holes in the P4VP did not further dewet: annealing of the micropatterned polymer bilayers at 190 °C for 2 h resulted in no significant increase in the lateral size of the imprinted holes (760 ± 30 nm), while a slight decrease in the depth was observed (45 ± 5 nm) (Figure 5.8c). The depth decrease is likely to be caused by partial layer inversion in the P4VP/PS bilayers, and was confirmed by the selective removal of the P4VP top layer by ethanol washing, which revealed PS films micropatterned with spatially-ordered holes with diameter of 620 ± 20 nm and depth of 20 ± 5 nm (Figure 5.8d). In this case, we believe the lateral size of the imprinted holes did not increase after prolonged annealing at 190 °C due to the surface crosslinking of the P4VP films upon UVO treatment.^{40, 41}

In order to remove the contribution of layer inversion, the PS bottom film was replaced by a hydrophobised silicon wafer (coated with a self-assembled monolayer of octadecyltrichlorosilane, OTS). UVO treatment allowed the fabrication of highly-ordered colloidal crystals on P4VP (Figure 5.9a), which produced ordered arrays of holes in the polymer film upon colloidal imprinting (Figure 5.9b). Imprinting holes (diameter: 780 ± 30 nm) in the P4VP monolayers were flat-bottomed and with depth (38 ± 2 nm) comparable to the thickness of the polymer films, indicating that the underlying OTS-silicon substrate was exposed to the air after particle removal. Although uniform P4VP films were proved to dewet on OTS-coated silicon wafers (Figure 5.10), annealing of the imprinted P4VP monolayers on OTS-silicon at 180-200 °C caused the progressive decrease of both hole diameter and depth (Figure 5.9c-e). Even in this case, partial cross-linking of the surface of P4VP by UVO treatment inhibited the dewetting, preventing the holes to grow in size. Hole shrinking is believed to be related to layer inversion occurring within the P4VP monolayer. The surface tension of the top few nanometers of P4VP films exposed to UVO treatment was likely to be increased with respect to the rest of the polymer film as a consequence of the increased hydrophilicity of the films' surface.³⁹ Therefore, the film rearranged to close-up the holes with lower surface tension P4VP.

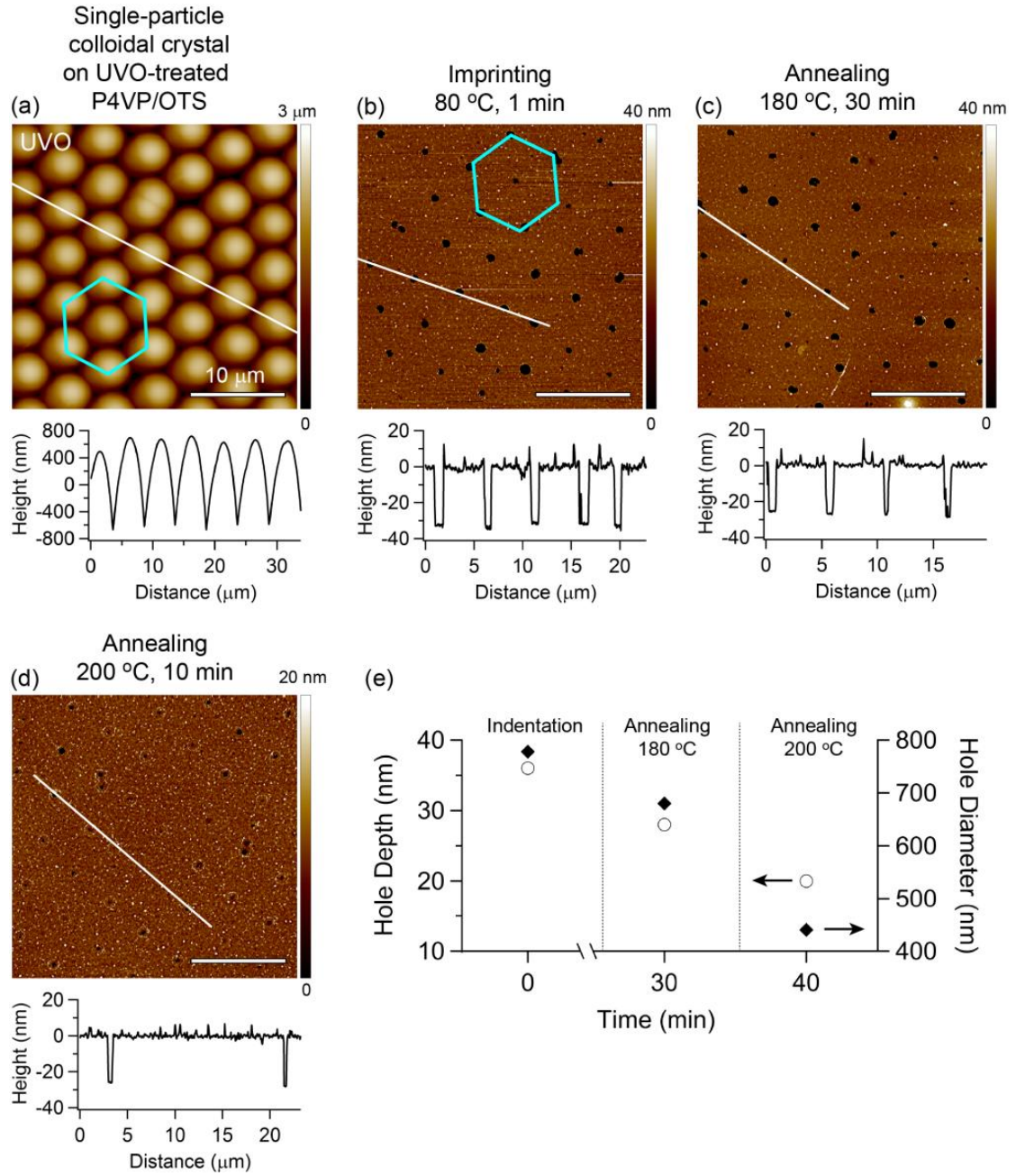


Figure 5.9. AFM topography images and line-cross sections of (a) single-particle colloidal crystals assembled on UVO-treated P4VP films on OTS-coated silicon, and micropatterned P4VP monolayers after (b) colloidal imprinting at 80 $^{\circ}\text{C}$ for 1 min, (c) annealing at 180 $^{\circ}\text{C}$ for 30 min, (d) annealing at 200 $^{\circ}\text{C}$ for 10 min. (e) Depth and diameter of the imprinted holes in function of annealing temperature and time.

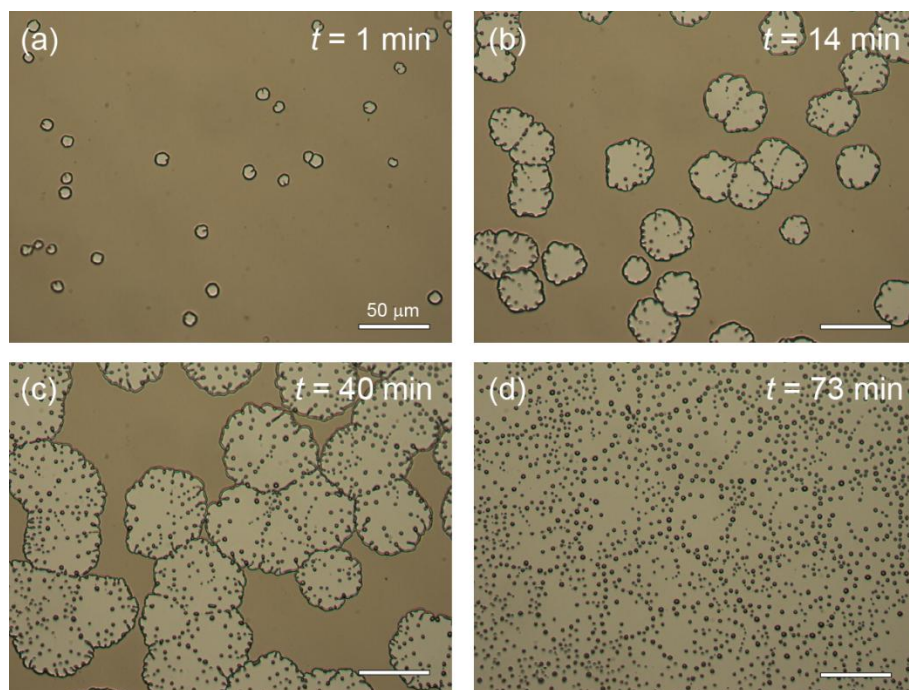


Figure 5.10. Optical micrographs showing the typical real-time dewetting of P4VP films on top of silicon wafers coated with uniform self-assembly monolayers of OTS. Annealing temperature: 180 °C.

5.4. Discussion

The dewetting of thin polymer films represents a flexible and robust route for the creation of surface micropatterns with controlled chemistry and topography. The size of the surface patterns produced by polymer dewetting can be easily controlled by tuning the annealing temperature and time, and the dewetting can be stopped at any stage of hole growth by cooling the polymer films down to room temperature. Typical dewetting patterns in uniform polymer films on plain substrates consist of arrays of holes nucleated at random locations of the polymer surface. Polymer dewetting can be guided to occur in an ordered fashion by introducing chemical and/or physical heterogeneities on the substrate.

In this Chapter, we presented for the first time the use of colloidal imprinting to guide the dewetting of polymer bilayers. Different polymer films could replace the P4VP/PS bilayers, provided that the wettability of the polymer surface is compatible with the self-assembly of the colloidal particles into colloidal crystals (i.e. hydrophilic polymers for hydrophilic colloidal particles, and hydrophobic polymers for hydrophobic colloidal particles), and that the polymer film dewets on the underlying substrate. In

our investigation, we highlighted a number of important physico-chemical mechanisms, as detailed below.

5.4.1. Colloidal imprinting

Colloidal imprinting with both binary and single-particle colloidal crystals was used to pattern the P4VP/PS bilayers with ordered arrays of holes mirroring the position of the colloidal particles. The size and depth of the imprinted holes is strikingly well controlled, and, as shown previously, can be controlled by tuning the imprinting time and temperature.^{23, 42} In this study, we found that the depth of the imprinted holes plays a crucial role for the subsequent hole growth by dewetting. Successful dewetting in the imprinted P4VP/PS bilayers was observed only when the depth of the imprinted holes was larger than the thickness of the P4VP top films, whereas holes closed-up upon annealing when their depth was smaller than the film thickness. The reason is believed to be related to the interplay between polymer dewetting and surface tension-driven smoothing-over of the polymer film. For shallow imprinted holes, the dewetting driving force was weaker than the interfacial stress in the polymer film, causing the P4VP top layer to smooth-over by a vertical decay mechanism already described in the literature.³¹

5.4.2. Guided dewetting

The ordered arrays of holes obtained by colloidal imprinting on the P4VP/PS bilayers were used to guide the dewetting of P4VP films. Upon annealing above the glass transition temperature, the imprinted P4VP films dewetted on top of the underlying PS films by site-specific nucleation initiated by the imprinted holes. The guided dewetting in the P4VP top layers produced surface micropatterns consisting in ordered arrays of holes with tuneable size and depth, with a maximum 7-fold increase in lateral size of the holes from imprinting to coalescence with neighbouring holes, and 6-fold increase in depth from beginning to end. The ability to guide dewetting in an ordered fashion and the ability to control and tune both size and depth of the imprinted holes over a range of almost one order of magnitude by simply tuning the annealing temperature and time are key features of this approach coupling polymer dewetting to colloidal imprinting.

5.4.3. Wettability of the polymer films

The wettability of the polymer film used as a substrate for the self-assembly of the colloidal particles, herein the P4VP top layer, governs the quality of the single-particle colloidal crystals, i.e. the degree of long-range order and the density of defects in the crystalline structure.⁴³ The local degree of order of single-particle colloidal crystals was enhanced and extended on the long-scale by performing the self-assembly on UVO-treated P4VP films, as a consequence of the increased hydrophilicity of the polymer surface with respect to plain P4VP. However, highly ordered single particle-colloidal crystals were obtained at the expense of partial cross-linking of the P4VP top layer induced by the UVO treatment, which inhibited polymer dewetting and prevented the imprinted holes in the P4VP/PS bilayers to grow in size upon annealing above the glass transition temperature. The degree of order and the density of defects in binary colloidal crystals were less sensitive to the wettability of the polymer surface, as the strong attractive capillary forces between the small PMMA particles guided the ordered self-assembly of the silica particles over large areas, leading to the formation of long-range colloidal crystals with low defect density on untreated P4VP films. However, the removal of PMMA particles by selective solvent wash is problematic and led to unwanted dewetting.

5.4.4. Layer inversion

Layer inversion was the dominating process in imprinted P4VP/PS bilayers featuring the relatively mobile PS96 as bottom layer, in which we observed the inhibition of polymer dewetting and the closure of the imprinted holes caused by the migration of the PS bottom layer upon annealing above the glass transition temperature. The rate of layer inversion was significantly reduced and polymer dewetting became the dominant process when the more viscous PS236 was used as a bottom layer. The reduction of the melt viscosity of the PS bottom layer allowed the imprinted P4VP top layer to dewet upon annealing above the glass transition temperature, leading to the growth in size of the holes in the P4VP/PS bilayers produced by colloidal imprinting.

5.5. Summary

We achieved for the first time the guided dewetting of thin polymer films by colloidal imprinting to produce micropatterned polymer surfaces with spatially controlled features. Binary and single-particle colloidal crystals were used as patterning templates to micropattern P4VP/PS bilayers with ordered arrays of holes. Colloidal imprinting with binary colloidal crystals produced bimodal distributions of spatially-ordered holes, whereas monomodal distributions of holes were obtained using single-particle colloidal crystals. Dewetting allowed the control over both the lateral size and the depth of the holes in the polymer bilayers by tuning annealing temperature and time.

The effect of the MW of the PS bottom layer and the wettability of the P4VP top layer on the dewetting of the imprinted bilayers was investigated. Successful growth of the imprinted holes by dewetting of the P4VP top layer was observed only in systems featuring high-MW PS (PS236) as bottom layer, in which the high melt viscosity of the bottom layer reduced the rate of layer inversion in the P4VP/PS bilayers and allowed P4VP to dewet. The increase in the wettability of the P4VP top layer by UVO treatment allowed the fabrication of extended single-particle colloidal crystals with long-range order at the expense of the partial cross-linking of the polymer, which inhibited the dewetting of P4VP.

The micropatterning approach proposed in the present work combines the advantages of colloidal imprinting (highly-ordered surface patterns) to that of polymer dewetting (fine and easy tuning of hole size), and represents a universal patterning route that can be extended to the patterning of a wide range of polymer films. The main advantage with respect to colloidal imprinting alone is the ability to tune the hole size after the imprinting stage, without the need of using different colloidal crystals for different hole size. Potential applications of the topographical and chemical micropatterns produced in this work include the development of microarrays for cell studies.

References

1. Gentili, D.; Foschi, G.; Valle, F.; Cavallini, M.; Biscarini, F., Applications of Dewetting in Micro and Nanotechnology. *Chemical Society Reviews* **2012**, *41*, 4430-4443.
2. Thickett, S. C.; Neto, C.; Harris, A. T., Biomimetic Surface Coatings for Atmospheric Water Capture Prepared by Dewetting of Polymer Films. *Advanced Materials* **2011**, *23*, 3718.
3. Telford, A. M.; Meagher, L.; Glattauer, V.; Gengenbach, T. R.; Easton, C. D.; Neto, C., Micropatterning of Polymer Brushes: Grafting from Dewetting Polymer Films for Biological Applications. *Biomacromolecules* **2012**, *13*, 2989-2996.
4. Thickett, S. C.; Moses, J.; Gamble, J. R.; Neto, C., Micropatterned Substrates Made by Polymer Bilayer Dewetting and Collagen Nanoscale Assembly Support Endothelial Cell Adhesion. *Soft Matter* **2012**, *8*, 9996-10007.
5. Lim, S. K.; Perrier, S.; Neto, C., Patterned Chemisorption of Proteins by Thin Polymer Film Dewetting. *Soft Matter* **2013**, *9*, 2598-2602.
6. Redon, F.; Brochard-Wyart, F.; Rondelez, F., Dynamics of Dewetting. *Physical Review Letters* **1991**, *66*, 715-719.
7. Higgins, A. M.; Jones, R. A. L., Anisotropic Spinoidal Dewetting as a Route to Self-Assembly of Patterned Surfaces. *Nature* **2000**, *404*, 476-478.
8. Kim, Y. S.; Lee, H. H., Selective Dewetting for General Purpose Patterning. *Advanced Materials* **2003**, *15*, 332-334.
9. Ghezzi, M.; Thickett, S. C.; Neto, C., Early and Intermediate Stages of Guided Dewetting in Polystyrene Thin Films. *Langmuir* **2012**, *28*, 10147-10151.
10. Jiang, P.; Bertone, J. F.; Hwang, K. S.; Colvin, V. L., Single-Crystal Colloidal Multilayers of Controlled Thickness. *Chemistry of Materials* **1999**, *11*, 2132-2140.
11. Singh, G.; Pillai, S.; Arpanaei, A.; Kingshott, P., Multicomponent Colloidal Crystals That Are Tunable over Large Areas. *Soft Matter* **2011**, *7*, 3290-3294.
12. Yang, S. M.; Jang, S. G.; Choi, D. G.; Kim, S.; Yu, H. K., Nanomachining by Colloidal Lithography. *Small* **2006**, *2*, 458-475.
13. Li, L.; Zhai, T. Y.; Zeng, H. B.; Fang, X. S.; Bando, Y.; Golberg, D., Polystyrene Sphere-Assisted One-Dimensional Nanostructure Arrays: Synthesis and Applications. *Journal of Material Chemistry* **2011**, *21*, 40-56.
14. Jia, L. C.; Cai, W. P., Micro/Nanostructured Ordered Porous Films and Their Structurally Induced Control of the Gas Sensing Performances. *Advanced Functional Materials* **2010**, *20*, 3765-3773.
15. Zhang, J. H.; Li, Y. F.; Zhang, X. M.; Yang, B., Colloidal Self-Assembly Meets Nanofabrication: From Two-Dimensional Colloidal Crystals to Nanostructure Arrays. *Advanced Materials*. **2010**, *22*, 4249-4269.

16. Singh, G.; Pillai, S.; Arpanaei, A.; Kingshott, P., Layer-by-Layer Growth of Multicomponent Colloidal Crystals over Large Areas. *Advanced Functional Materials* **2011**, *21*, 2556-2563.
17. Singh, G.; Gohri, V.; Pillai, S.; Arpanaei, A.; Foss, M.; Kingshott, P., Large-Area Protein Patterns Generated by Ordered Binary Colloidal Assemblies as Templates. *ACS Nano* **2011**, *5*, 3542-3551.
18. Singh, G.; Pillai, S.; Arpanaei, A.; Kingshott, P., Electrostatic and Capillary Force Directed Tunable 3d Binary Micro- and Nanoparticle Assemblies on Surfaces. *Nanotechnology* **2011**, *22*.
19. Kosiorek, A.; Kandulski, W.; Glaczynska, H.; Giersig, M., Fabrication of Nanoscale Rings, Dots, and Rods by Combining Shadow Nanosphere Lithography and Annealed Polystyrene Nanosphere Masks. *Small* **2005**, *1*, 439-444.
20. Lei, Y.; Yang, S. K.; Wu, M. H.; Wilde, G., Surface Patterning Using Templates: Concept, Properties and Device Applications. *Chemistry Society Reviews* **2011**, *40*, 1247-1258.
21. Chen, J. X.; Liao, W. S.; Chen, X.; Yang, T. L.; Wark, S. E.; Son, D. H.; Batteas, J. D.; Cremer, P. S., Evaporation-Induced Assembly of Quantum Dots into Nanorings. *ACS Nano* **2009**, *3*, 173-180.
22. Park, J. Y., Lithographically Patterned Micro/Nanostructures Via Colloidal Lithography. *Korean Journal of Chemical Engineering* **2014**, *31*, 541-547.
23. Oh, J. R.; Moon, J. H.; Park, H. K.; Park, J. H.; Chung, H.; Jeong, J.; Kim, W.; Do, Y. R., Wafer-Scale Colloidal Lithography Based on Self-Assembly of Polystyrene Nanospheres and Atomic Layer Deposition. *Journal of Material Chemistry* **2010**, *20*, 5025-5029.
24. Acikgoz, C.; Ling, X. Y.; Phang, I. Y.; Hempenius, M. A.; Reinhoudt, D. N.; Huskens, J.; Vancso, C. J., Fabrication of Freestanding Nanoporous Polythiersulfone Membranes Using Organometallic Polymer Resists Patterned by Nanosphere Lithography. *Advanced Materials* **2009**, *21*, 2064-2067.
25. Choi, D. G.; Jang, S. G.; Yu, H. K.; Yang, S. M., Two-Dimensional Polymer Nanopattern by Using Particle-Assisted Soft Lithography. *Chemistry of Materials* **2004**, *16*, 3410-3413.
26. Chen, Z. M.; Gang, T.; Yan, X.; Li, X.; Zhang, J. H.; Wang, Y. F.; Chen, X.; Sun, Z. Q.; Zhang, K.; Zhao, B.; Yang, B., Ordered Silica Microspheres Unsymmetrically Coated with Ag Nanoparticles, and Ag-Nanoparticle-Doped Polymer Voids Fabricated by Microcontact Printing and Chemical Reduction. *Advanced Materials* **2006**, *18*, 924.
27. Jang, S. G.; Choi, D. G.; Heo, C. J.; Lee, S. Y.; Yang, S. M., Nanoscopic Ordered Voids and Metal Caps by Controlled Trapping of Colloidal Particles at Polymeric Film Surfaces. *Advanced Materials* **2008**, *20*, 4862.
28. Thickett, S.; Harris, A.; Neto, C., Interplay between Dewetting and Layer Inversion in P4VP/PS Bilayers. *Langmuir* **2010**, *26*, 15989-15999.

29. Lessel, M.; Bäumchen, O.; Klos, M.; Hähl, H.; Fetzer, R.; Seemann, R.; Jacobs, K., Self-Assembled Silane Monolayers: A Step-by-Step High Speed Recipe for High-Quality, Low Energy Surfaces. *arXiv:1212.0998* **2012**.
30. Steiner, U.; Klein, J.; Fetters, L. J., Surface Phase Inversion in Finite-Sized Binary-Mixtures. *Physical Review Letters* **1994**, 72, 1498-1501.
31. Ahn, D. U.; Ding, Y. F., Vertical Pattern Decay and Lateral in-Phase Capillary Breakup of Nanoimprinted Bilayer Polymer Films. *Soft Matter* **2011**, 7, 3794-3800.
32. Singh, G.; Pillai, S.; Arpanaei, A.; Kingshott, P., Highly Ordered Mixed Protein Patterns over Large Areas from Self-Assembly of Binary Colloids. *Advanced Materials* **2011**, 23, 1519-1523.
33. Vrij, A., Possible Mechanism for Spontaneous Rupture of Thin Free Liquid Films. *Discussions of the Faraday Society* **1966**, 42, 23-33.
34. Xu, L.; Shi, T. F.; An, L., Nonsolvent-Induced Dewetting of Thin Polymer Films. *Langmuir* **2007**, 23, 9282-9286.
35. Watanabe, H., Viscoelasticity and Dynamics of Entangled Polymers. *Progress in Polymer Science* **1999**, 24, 1253-1403.
36. Denkov, N. D.; Velev, O. D.; Kralchevsky, P. A.; Ivanov, I. B.; Yoshimura, H.; Nagayama, K., 2-Dimensional Crystallization. *Nature* **1993**, 361, 26-26.
37. Damman, P.; Baudalet, N.; Reiter, G., Dewetting near the Glass Transition: Transition from a Capillary Force Dominated to a Dissipation Dominated Regime. *Physical Review Letters* **2003**, 91.
38. Kang, H.; Lee, S.-H.; Kim, S.; Char, K., Dewetting and Layer Inversion of Inverted PVP/PS Bilayer Films. *Macromolecules* **2003**, 36, 8579-8583.
39. Efimenko, K.; Wallace, W. E.; Genzer, J., Surface Modification of Sylgard-184 Poly(Dimethyl Siloxane) Networks by Ultraviolet and Ultraviolet/Ozone Treatment. *Journal of Colloid and Interface Science* **2002**, 254, 306-315.
40. Xue, L. J.; Han, Y. C., Inhibition of Dewetting of Thin Polymer Films. *Progress in Materials Science* **2012**, 57, 947-979.
41. Akhrass, S. A.; Ostaci, R.-V.; Grohens, Y.; Drockenmuller, E.; Reiter, G., Influence of Progressive Cross-Linking on Dewetting of Polystyrene Thin Films. *Langmuir* **2008**, 24.
42. Ren, Z. Y.; Zhang, X. M.; Zhang, J. J.; Li, X.; Yang, B., Building Cavities in Microspheres and Nanospheres. *Nanotechnology* **2009**, 20.
43. Ye, X. Z.; Qi, L. M., Two-Dimensionally Patterned Nanostructures Based on Monolayer Colloidal Crystals: Controllable Fabrication, Assembly, and Applications. *Nano Today* **2011**, 6, 608-631.

Chapter 6.

Conclusions and Outlook

This Thesis describes a study of the spontaneous dewetting of thin polymer films leading to micropatterned polymer surfaces with controlled chemistry and topography. The chief advantage of micropatterned surfaces produced by polymer dewetting is the ease with which they can be produced on both flat and 3D objects, and the ability to control the size of the pattern by simply tuning the annealing conditions, without the need for expensive materials, instrumentation and time-consuming procedures.

Chapter 3 describes a study of micropatterned polymer coatings for site-specific protein adsorption. In this study, surface micropatterns were produced for the first time by the dewetting of PLGA thin films on top of PS films. In order to increase the protein repellence of PLGA and enhance the difference in protein affinity with respect to the PS bottom layer, the micropatterned PLGA/PS bilayers were functionalized by covalent immobilization of PEG molecules. The functionalization of PLGA films was performed by a simple two-step grafting route, consisting in the activation of PLGA by either aminolysis or hydrolysis, followed by grafting of PEG. The functionalization protocol proposed in this study required limited synthetic effort, as all the chemicals employed were commercially available, and offers good flexibility, as a wide range of reactions and functional groups could be used to graft PEG molecules to aminolyzed/hydrolyzed PLGA.

The low protein absorptivity of the novel PEG-grafted PLGA films was employed to micropattern proteins by preferential protein adsorption inside the PS domain exposed in the partially dewetted PLGA/PS bilayers. The grafting of PEG

molecules increased the degradation resistance of PLGA films with respect to untreated PLGA, due to the passivating effect of the PEG coatings, which protected the polymer films from hydrolysis upon immersion in PBS buffer. Low protein absorptivity and good degradation resistance, combined with the low cytotoxicity of both PEG and PLGA, make PEG-grafted PLGA films a promising platform for biological applications, such as single cell studies and tissue engineering.

The use of PEG molecules bearing one epoxide group at each end most likely caused the partial chemisorption of proteins on the unreacted epoxide groups exposed by the grafted PEG chains, which decreased the protein repellence of the PEG-grafted PLGA films. Future studies would require the optimization of the grafting reaction with PEG molecules bearing a single reactive group, in order to avoid both protein chemisorption and formation of PEG loops on the surface of functionalized PLGA films. During our studies, we discovered that 40 nm-thick PEG-grafted PLGA films on silicon dewet at temperatures between 40 and 60 °C when immersed in water (Figure 6.1), which is significantly lower than the temperature required to dewet PLGA films of similar thickness on PS (dewetting observed at $T > 100$ °C).

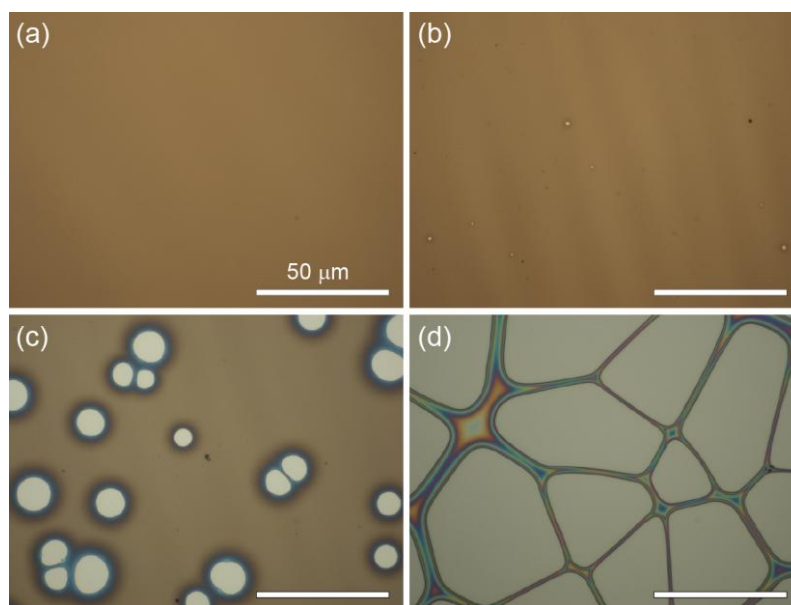


Figure 6.1. Optical micrographs showing the typical dewetting of PEG-grafted PLGA films on silicon substrates upon annealing at (a) 35 °C, (b) 40 °C, (c) 50 °C, and (d) 60 °C for 1 hour in water.

This finding is significant because in the future it may allow the adsorption of biological molecules on the substrate prior to dewetting, and dewetting could occur at temperatures compatible with, for example, protein stability. These findings, combined with the good protein repellence of PEG-grafted PLGA films, represent the fundamental framework for future investigations focused on the development of PLGA-based micropatterned surfaces for protein multiplexing, i.e. the co-patterning of more than one type of protein or other biomolecule on the same substrate.^{1, 2}

Patterns arising from the dewetting of thin polymer films typically consist of randomly distributed holes. To date, this is one of the main arguments against the use of polymer dewetting in several technological applications where it is perceived that ordered patterns are desirable or necessary, such as biosensing. However, it is possible to force the dewetting to occur in an ordered fashion by introducing chemical or physical heterogeneities to favor the nucleation of holes at specific locations. In this Thesis, we demonstrated that dewetting patterns with spatially ordered features could be obtained in a relatively simple manner, by the combination of polymer dewetting and microcontact printing or by using colloidal imprinting,

In Chapter 4, ordered surface patterns were obtained by the dewetting of thin PS films on silica substrates which had been micropatterned with OTS self-assembled monolayers using microcontact printing. PS films selectively dewetted on top of the OTS patterns, producing two different types of ordered patterns depending on the annealing temperature and time. At low temperature, the dewetting of PS produced polymer micropatterns which mirrored and amplified the features of the underlying OTS pattern in the vertical dimension. The prolonged dewetting of PS at high temperature caused the complete retraction of the polymer film into ordered arrays of isolated droplets with bimodal size distribution. Investigation of the dynamics of hole growth showed that the dewetting rate in PS films was affected by the underlying OTS pattern. Pinning of the contact line and symmetry constraints in the growth of ellipsoidal holes were identified as the main reasons for the decrease of the dewetting rate observed as the hole size approached the size of the OTS pattern.

Microcontact printing is a versatile technique to create chemical patterns with several different geometries of choice in order to guide the dewetting of thin polymer film in an ordered fashion. However, in spite of the relative ease of execution, one of

the main issues related to microcontact printing of alkylsilanes on silicon is the formation of oligomers and multilayers during the self-assembly process, due to the high reactivity of the alkylsilanes. Inhomogeneities in the self-assembled monolayer can affect the nucleation and hole growth in the polymer films and limit the control over the dewetting patterns in the early stages of dewetting. Future investigations should address this by improving the quality of the self-assembled monolayers by using molecules with lower reactivity than alkylsilane as ‘ink’ for microcontact printing. A promising category of candidates is that of alkyl derivatives which are capable of making non-covalent halogen bonds with the substrate.^{3, 4} Research along these lines is currently under way in the Neto group.

Finally, in Chapter 5 we investigated the combination of polymer dewetting and colloidal imprinting to produce spatially-ordered dewetting patterns. Colloidal imprinting with both binary and single-particle colloidal crystals was used to micropattern P4VP/PS bilayers with ordered arrays of holes mirroring the position of the particles within the colloidal crystal. Imprinted holes in the P4VP/PS bilayers acted as nuclei for the site-selective dewetting of the P4VP top layer upon annealing above the glass transition temperature. Dewetting of P4VP allowed for control of the size and the depth of the imprinted holes by simply tuning the annealing time and temperature, combining the advantages of colloidal imprinting (high order) to those of polymer dewetting (ease of tuning).

The results of our investigations showed that the wettability of the P4VP top layer and the molecular weight (MW) of the PS bottom layer were the two main parameters governing the order and the growth of the imprinted holes in the P4VP/PS bilayers, respectively. The MW of the PS bottom layer affected the rate of layer inversion in the P4VP/PS bilayers: in systems featuring low-MW PS (PS96) layer inversion overtook the rate of the dewetting process and prevented the growth of the imprinted holes upon annealing above the glass transition temperature. The wettability of the P4VP top layer significantly affected the long-range order in the colloidal crystals. The long-range order in single-particle silica colloidal crystals was extended by UVO treatment at the expense of partial cross-linking of the P4VP top layer, which caused the inhibition of polymer dewetting and prevented the growth of the imprinted holes. In light of these observations, future investigations should involve the design and development of systems consisting of polymer films and colloidal particles with

matched wettability. This approach should result in the ability to fabricate extended colloidal crystals with high a degree of long-range order, and hence highly-ordered arrays of imprinted holes after colloidal imprinting. Possible applications of micropatterned surfaces featuring highly-ordered arrays of holes include biosensing and chips for automated read-out.

The work presented in this Thesis has demonstrated that the dewetting of thin polymer films is a flexible and robust method to produce functional surface micropatterns with chemical and topographical features. The ability to control and tune both the chemistry and the topography of the surfaces in a simple manner creates many opportunities for the application of polymer dewetting in advanced nanoscale technologies. One possible point of weakness of polymer dewetting is the intrinsic limitation related to the use of thin polymer films (< 100 nm). Thick polymer films (> 1 μm) have several advantages from an industrial perspective, as they can be easily prepared by dip-coating or roll printing, and have better mechanical resistance than thin polymer films. Recent unpublished work in the Neto group has shown that μm -thick polymer films can be dewetted by solvent or vapor annealing, representing an important milestone for the future application of polymer dewetting in several industrial and technological applications. An alternative solution might be reached by using composite thin films, containing polymer and inorganic nanoparticles, which could be made to fuse at high temperatures, forming inorganic self-assembled patterns.

References

1. Agheli, H.; Malmstrom, J.; Larsson, E. M.; Textor, M.; Sutherland, D. S., Large Area Protein Nanopatterning for Biological Applications. *Nano Letters* **2006**, *6*, 1165-1171.
2. Singh, G.; Pillai, S.; Arpanaei, A.; Kingshott, P., Highly Ordered Mixed Protein Patterns over Large Areas from Self-Assembly of Binary Colloids. *Advanced Materials* **2011**, *23*, 1519-1523.
3. Metrangolo, P.; Meyer, F.; Pilati, T.; Resnati, G.; Terraneo, G., Halogen Bonding in Supramolecular Chemistry. *Angewandte Chemie-International Edition* **2008**, *47*, 6114-6127.

4. Politzer, P.; Lane, P.; Concha, M. C.; Ma, Y. G.; Murray, J. S., An Overview of Halogen Bonding. *Journal of Molecular Modeling* **2007**, *13*, 305-311.